Escola de Camins
Escola Tècnica Superior d'Enginyeria de Camins, Canals i Ports
UPC BARCELONATECH

Contributions to the simulation of salt concrete - Short- and long-term mechanical behavior description involving an advanced plasticity model approach

MASTER FINAL THESIS

Final Thesis developed by:
Middelhoff, Marvin

Directed by:
Rodriguez-Dono, Alfonso
Olivella, Sebastìa

Master in:
Civil Engineering

Barcelona, 23. January 2017

Department of Civil and Environmental Engineering

MASTER THESIS

CONTRIBUTIONS TO THE SIMULATION OF SALT CONCRETE - SHORT- AND LONG-TERM MECHANICAL BEHAVIOR DESCRIPTION INVOLVING AN ADVANCED PLASTICITY MODEL APPROACH

Marvin Middelhoff
(404147)

Reviewed by:

Alfonso Rodriguez-Dono
Department of Civil and Environmental Engineering
Universitat Politècnica de Catalunya (UPC BarcelonaTech)
Barcelona, Spain

And

Sebastìa Olivella
Department of Civil and Environmental Engineering
Universitat Politècnica de Catalunya (UPC BarcelonaTech)
Barcelona, Spain

Supported by:

Miguel Ángel Mánica Malcom
Department of Civil and Environmental Engineering
Universitat Politècnica de Catalunya (UPC BarcelonaTech)
Barcelona, Spain

23. January 2017

Key words: Rock salt, Concrete based sealing materials, Salt concrete, Numerical simulation

ABSTRACT

In the former German concept, rock salt was the favorite host rock to dispose heat-generating radioactive waste. To assure the integrity of the complete repository system after closure, shafts and drifts have to be sealed. In the context of the DOPAS project GRS performed a laboratory test program and numerical simulations to investigate the properties of concrete based sealing materials. The test program and the numerical simulations mainly focused on salt concrete. In order to perform the numerical simulations, the finite-element-method program Code_Bright was employed.

Former attempts of simulating the short-and long-term mechanical behavior of salt concrete yielded insufficient results with respect to the reproduction of 1) volumetric strains, 2) a stress reduction as a respond to the damage within the sample and 3) viscoplastic strains upon passing a deviatoric stress level above 20 MPa. Among other modeling approaches, an advanced plasticity constitutive model has been taken into account, which is currently being developed. It enables the simulation of 1) strain-hardening prior peak, 2) peak strength, 3) strain-softening post peak and 4) time-dependent creep deformations. A detailed assessment has already revealed the applicability of the new constitutive model in terms of describing the creep behavior. The present thesis pursues the objective of reproducing the entire mechanical behavior of salt concrete by means of employing the advanced plasticity constitutive model. Moreover it is envisaged to identify limitations of the model and to mention further development needs finally.

ACKNOWLEDGEMENT

First of all I am indebted to GRS as they provided me with technical reports and experiment data, which represent the base of the present thesis. Further I am glad about the support of Mr. Oliver Czaikowski. His arguments and ideas have always inspired me to question elaborately my obtained results regarding to credibility.

In general I give thanks to all involved persons for supporting me while simulating and writing. Among many, I want to thank Mr. Miguel Ángel Manica Malcom first of all. He has often shown great patience when we went through some parts of the employed constitutive model. Moreover we had a lot of constructive conversations, which helped to improve this thesis. Second I am really proud and lucky to be intensively supported by Mr. Sebastìa Olivella and Mr. Jean Vaunat. They are able to explain difficult issues in a wonderful simple way. Apart from Sebastìa and Jean, I give thanks to Mr. Alfonso Rodriguez Dono. He helped me in a lot of situations, especially during the first and last months at UPC when I was drifting. Furthermore he agreed to mark this thesis as the first reviewer.

The last massive "Thank you" is dedicated to all my coworkers in the institute, especially to Carme, Laura, Nuria and Roger (alphabetically listed to not imply any ranking)! The coffee breaks helped me a lot to arrange my weird thoughts!

TABLE OF CONTENT

LIST OF SYMBOLS AND ABBREVIATIONS

Perception

Symbol/ Abbreviation	Description
BMU	Federal Ministry for Environment, Nature Conservation and Nuclear Safety
CRZ	Containment-providing Rock Zone
FEM	Finite-Element Method
HEP	Hardening Elastic Plastic model
HLW	High-Level Radioactive Waste
IAEA	International Atomic Energy Agency
IEA	International Energy Agency
ILW	Intermediate-Level Radioactive Waste
LDVT	Linear Differential Variable Transformer
LE	Linear-Elasticity model
LEPP	Linear-Elastic Perfectly Plastic model
LLW	Low-Level Radioactive Waste
OECD-NEA	OECD Nuclear Energy Agency
RPP	Rigid Perfectly Plastic model
TC	Triaxial Compression Experiment
TCc	Triaxial Compression Creep Experiment
THM	Thermal-Hydraulic-Mechanically coupled processes
UC	Uniaxial Compression Experiment
UCc	Uniaxial Compression Creep Experiment
VP	Viscoplasticity model

Capital letters

Symbol/ Abbreviation	Description	Unit
D	Initial diameter	m
$\mathbf{D}_{ep}$	Elasto-plastic constitutive matrix	
E	Young's modulus	MPa
H	Plastic modulus	MPa
I	Identity matrix	-
J	Deviatoric stress invariant	MPa
L	Initial length	m
R	Initial radius	m
S	Deviatoric stress tensor	MPa
T	Temperature	°C

Small letters

Symbol/ Abbreviation	Description	Unit
a_{hard}	Material parameter	-
a_{soft}	Material parameter	-
$\mathbf{b}$	Column matrix of body forces	MPa
c	Cohesion	MPa
f	Yield function	
g	Plastic potential	
$\mathbf{j_s}$	Total mass flux of the solid	$m*s^{-1}$
m	Material parameter	-
n	Material parameter	-
p	Mean stress	MPa
q	Deviatoric stress	MPa
$\mathbf{u}$	Column matrix of displacements	m
w	Water content	%

Greek letters (1)

Symbol/ Abbreviation	Description	Unit
γ	Viscosity	d^{-1}
$d\varepsilon^c$	Creep strain increment	-
$d\boldsymbol{\varepsilon}^c$	Creep strain increment tensor	-
$d\varepsilon^p$	Plastic strain increment	-
$d\boldsymbol{\varepsilon}^p$	Plastic strain increment tensor	-
$d\varepsilon^{tot}$	Total strain increment	-
$d\boldsymbol{\varepsilon}^{tot}$	Total strain increment tensor	-
$d\varepsilon^{vp}$	Viscoplastic strain increment	-
$d\boldsymbol{\varepsilon}^{vp}$	Viscoplastic strain increment tensor	-
$d\varepsilon^p_{eq}$	Equivalent plastic strain increment	-
$d\boldsymbol{\varepsilon}^p_{eq}$	Equivalent plastic strain increment tensor	-
$\dot{\varepsilon}$	Strain rate	s^{-1}
$\dot{\boldsymbol{\varepsilon}}$	Strain rate tensor	s^{-1}
ε_{vol}	Volumetric strain	-
η	Viscosity	Pa*s
θ	Lode-Angle	°
$d\lambda$	Plastic multiplier	-
ν	Poisson's ratio	-
ξ_1	Material parameter	-
ξ_2	Material parameter	-
ξ_3	Material parameter	-
ρ	Density	$kg*m^{-3}$
$\boldsymbol{\sigma}$	Stress tensor	MPa
σ_{Ax}	Axial stress	MPa
$\sigma_{Dilatancy}$	Stress at the dilatancy point	MPa

Greek letters (2)

Symbol/ Abbreviation	Description	Unit
σ_{Iso}	Isotropic stress	MPa
σ_{Rad}	Radial/ Confining stress	MPa
$\dot{\sigma}$	Stress rate	$MPa*s^{-1}$
$\dot{\boldsymbol{\sigma}}$	Stress rate tensor	$MPa*s^{-1}$
φ	Friction angle	°
ϕ_0	Reference porosity	-
ω	Non-associativity constant	-

Units

Denotation	Unit
Cubicmeter	m^2
Day	d
Degree Celsius	°C
Kilogram	kg
Mass-percent	mass-%
Megapascal	MPa
Meter	m
Pascal	Pa
Second	s
Square meter	m^2
Year	y

1 INTRODUCTION

The climate change represents one of the greatest challenges, which humankind has ever had to face. Compared to pre-industrial times, global temperatures increase must not exceed two degree Celsius (°C) by the end of the century. Otherwise the hazard of climate change would become uncontrollable according to generally accepted scientific studies. In order to counteract the temperature increase efficiently, one request among many included in the adopted "Paris Agreement" is the halving of global energy-related emissions by 2050. Hence a wide range of low-carbon energy technologies will be required to support the transition from fossil fuel to renewables. Although the Fukushima Daiichi nuclear power plant accident in 2011 and other issues made people lose confidence in nuclear energy, it represents a proven baseload electricity source emitting a small amount of CO_2. This circumstance in combination with other reasons have animated many countries to reaffirm the importance of nuclear energy within their national energy strategies (International Energy Agency - IEA und OECD Nuclear Energy Agency - NEA 2015).

One of the greatest issues accompanying the production of nuclear energy is the radioactive waste. Radioactive waste does not only arise from electricity production in nuclear power plants, but also from other different activities, e.g. medical treatments in hospital, research, national defense and mineral processing. The radioactive waste is classified into different groups as they contain different levels of energy concentration. Containing the highest level of energy concentration, "High-Level Waste (HLW)" arises exclusively from electricity production, whereas radioactive waste from other activities can be either attached to "Intermediate-Level Waste (ILW)" or to "Low Level Waste (LLW)". Despite of different energy concentrations, a common characteristic of all types of radioactive waste is its potential to present a hazard to people and to the environment (International Atomic Energy Agency - IAEA 2011).

The International Atomic Energy Agency (IAEA) established safety requirements concerning with the construction, operation and post-closure phase of disposal facilities for radioactive waste. It pursues the general objective to assure the long-term safety of people and the environment against the hazard of ionizing radiation. In this context disposal means an emplacement of the radioactive waste into a facility exclusively designed to contain the waste through a system of multiple engineered and natural barriers. These barriers work together without maintenance for a defined period of time in order to isolate the waste from the accessible biosphere (International Atomic Energy Agency - IAEA 2011).

The *Fig. 1-1* illustrates schematically the life span of the considered natural and engineered barriers. It should be noted that the figure illustrates a disposal concept, in which the natural barrier is the main barrier. Other concepts differ in this point. Nevertheless all concepts envisage completion of barriers after repository closure. The maximum color intensity indicates the time when the maximal sealing capacity will likely be reached. Lighter colors indicate a low sealing capacity. The timescale is only indicative (Mönig 2012).

Since a complete isolation is not practicable and the hazard associated with the waste declines with time, it is provided to inhibit, reduce and delay the migration of radionuclides from the

waste to the accessible biosphere at any time (International Atomic Energy Agency - IAEA 2011).

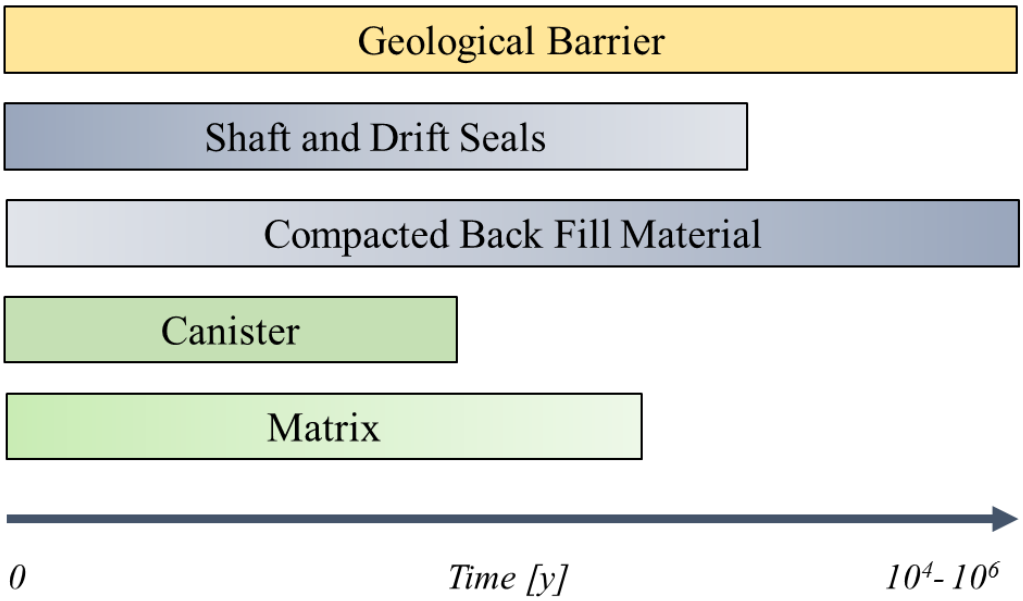

Fig. 1-1: Time-dependent effect of the different barriers in the post-closure phase of the repository

Backed by an international broad agreement, the mentioned safety requirements suggest the disposal of HLW in facilities constructed in geological formations at least few hundred meters below ground level. Main selection criteria for the geological formation are the long-term stability and hydrogeological properties. The safety requirements are formulated irrespectively of the geological formation, thus the radioactive waste can either be disposed in rock salt, in argillaceous rock or crystalline rock formations (International Atomic Energy Agency - IAEA 2011).

1.1 SAFETY REQUIREMENTS FORMULATED BY BMU

Likewise IAEA, the former Federal Ministry for the Environment, Nature Conservation and Nuclear Safety (BMU) formulated safety requirements for the construction, operation and post-closure phase of a repository for the disposal of heat-generating radioactive waste in Germany. The term “heat-generating radioactive waste” corresponds to high-level and a part of intermediate-level radioactive waste (International Atomic Energy Agency - IAEA 2009) . After (Bollingerfehr 2013) “heat-generating radioactive waste” is characterized by a high level of activity concentration and thus high thermal output during decay.

Till the repository site selection act (StandAG) became effective in 2013 (Bundesministerium der Justiz und für Verbraucherschutz 23.07.2013), the former German repository concept focused mainly on the disposal of heat-generating radioactive waste in deep rock salt formations. The concept envisaged defining a particular part within the selected repository site as a natural barrier (Fischer-Appelt 2013). Combined with the engineered barriers, the “Containment-

providing rock zone" (CRZ) serves the purpose of isolating the radioactive waste from the accessible biosphere and preventing a continuous advective transport of fluid phases from the overburden to the radioactive waste (Bollingerfehr 2013).

Five safety cases are requested by the safety requirements of BMU. One of these safety cases is the proof of the robustness of the final repository's technical components. It verifies the serviceability of backfilling and technical sealing structures (Bundesministerium für Umwelt, Naturschutz and Reaktorsicherheit 2010).

Fig. 1-2: Salt concrete sample B4KK1 – T_1.38m

Beside other materials, salt concrete will prospectively be utilized for sealing the emplacement drifts (Middelhoff und Czaikowski) (compare *Fig. 1-2*). Salt concrete is a mass concrete and it is composed of a cement matrix with inclusions of crushed salt (salt grains). Different types of salt concrete exist, depending on the ratio of cement, salt grains and brine. For instance salt concrete types M1 and M2 were employed in the ERAM (Morsleben repository), whereas the type ASSE has exclusively been employed in the ASSE-mine (Czaikowski et al. 2016). The *Tab. 1-1* informs about the composition of the ASSE-type salt concrete in detail:

Tab. 1-1: Composition of salt concrete type ASSE related to 1 m³ (Müller-Hoeppe 2012)

Composition of salt concrete	Proportion [kg/ m³]	Proportion [mass-%]
Blast furnace cement	380	18.3
Crushed salt	1496	72.1
NaCl-brine	198	9.6
Total	2074	100

1.2 SUMMARY OF PREVIOUS INVESTIGATIONS AND ASSESSMENTS

As requested in (Bundesministerium für Umwelt, Naturschutz and Reaktorsicherheit 2010), GRS has been investigating potential sealing and backfilling materials utilizable in salt and clay formations since 2012 (Middelhoff 18.08.2016). Beside other concrete based sealing materials, the investigations have primarily focused on salt concrete. They have involved comprehensive laboratory test sessions as well as numerical simulations. The laboratory test sessions pursued the objective of improving the knowledge about the mechanical and hydraulic properties of salt concrete. Accompanying numerical simulations made use of the results obtained from the experiments. In first instance they aimed at generating a set of material parameter that enables the adequate reproduction of the mechanical and hydraulic behavior of salt concrete. The employed specimen were extracted from a sealing element, which was constructed in the ASSE- salt mine 30 years ago. Detailed information about the sealing element can be found in (Czaikowski et al. 2016) and (Middelhoff 18.08.2016).

The laboratory test sessions dealt with investigations of the sealing capacity of salt concrete. Thus the evolution of strains under deviatoric loading was of same interest as the subsequent changes in porosity and permeability. The strain evolution has been examined in triaxial compression tests (TC-tests) first and in uniaxial compression creep tests (UCc-tests) and triaxial compression creep tests (TCc-tests) second. Gas injection while loading the salt concrete sample served the purpose of determining permeability changes.

Main results of the TC-tests have been the identification of material properties, e.g. young's modulus E and Poison ratio ν. It also became evident that ultimate compressive strength and dilatancy boundary depend strongly on the applied confining stresses. Additionally the TC-tests proved beneficial, because they revealed a transition from elastic deformations to viscoplastic ones. The elastic deformations occur when subjecting the samples to lower deviatoric stresses ($10\ \text{MPa} < \sigma_{Dev} < 20\ \text{MPa}$) and the viscoplastic ones when applying higher deviatoric stresses ($\sigma_{Dev} \geq 20\ \text{MPa}$). Examining the time-dependent deformation behavior, the uniaxial and triaxial compression creep tests revealed results being in accordance with the results from the previously performed TC-tests. First the salt concrete responded elastically to lower deviatoric stresses. Hence it has hardly been possible to detect creep deformations. As soon as subjecting the samples to higher deviatoric stresses, the samples deformed viscoplastically and stationary creep deformations have been exhibited in time.

Before carrying out the numerical simulations, a suitable constitutive law was selected. It was envisaged that the selected constitutive model is able to reproduce the observed strain transition including the evolution of volumetric strains. Moreover transient and stationary creep were supposed to be simulated. The utilized FEM-program Code_Bright incorporates constitutive models which enable the description of the behavior of crushed salt. Hence the applicability of the constitutive models seemed to be reasonable due to the high amount of crushed salt in the salt concrete.

Despite of the high amount of salt grains, the selected constitutive models revealed drawbacks, probably caused by the complex structure of salt concrete. The models were limited regarding to the reproduction of the transition of strains first, the determination of dilatancy second and

the reduction of deviatoric stresses as a respond to the damage of the specimen third. Apparently the greatest challenge is the adequate consideration of the failure of the cement bonds. The failure occur when increasing the deviatoric stresses above 20 MPa. Then the submitted stresses allocate to the residual bond structures and the salt grains (Czaikowski et al. 2016a).

In (Middelhoff 18.08.2016) a modified creep law being part of a recently developed plasticity model was assessed and evaluated. The applicability assessment pursued the objective whether the modified creep law is able to reproduce sufficiently the observed long-term deformations of salt concrete. Although exhibiting limitations with regard to stationary as well as tertiary creep and volumetric strains, the modified form is still able to simulate the observed behavior. The mentioned limitations are mainly caused by the mathematical simplicity of the modified creep law, which does not consider any functional change basing on alterations of the void ratio or the porosity.

1.3 OBJECTIVES AND LAYOUT OF THE THESIS

The entire description of the deformation behavior of salt concrete requires a complex constitutive model. On the one side the short-term behavior should sufficiently be accounted, including both the evolution of elastic and viscoplastic axial strains. Furthermore an adequate description of the volumetric strains is beneficial in order to estimate dilatancy. On the other hand the selected constitutive model should be able to reproduce the time-dependent deformation behavior, especially creep deformations that depends strongly on the applied deviatoric stress level. Currently an advanced plasticity constitutive model has been being developed and it seems to be applicable in terms of the simulation of observed deformations. Therefore the present thesis pursues the objective of reproducing the entire deformation behavior by making use of the mentioned advanced plasticity model. One set of material parameter will be derived from the available experiment data.

The second chapter gives a general introduction into the theory of plasticity and visco-plasticity in order to repeat later required knowledge in the field of solid mechanics. A detailed overview of the performed experiments is presented in the third chapter. It includes descriptions of the experiment layout, the testing procedures and the experiment results. Basing upon experiment results and previously gained experience, reasons for selecting the advanced plasticity constitutive model are elaborately discussed within the fourth chapter. Furthermore the theoretical background of the model is explained. The core of thesis is the detailed documentation of the performed calibration work in the fifth chapter. The numerical simulations concerned with the reproduction of triaxial compression tests (TC-tests) and uniaxial compression creep tests (UCc-tests). Afterwards the obtained results are discussed within the sixth chapter.

2 THEORETICAL BASIS

The chapter 0 discusses the results of the performed laboratory test program and the accompanying numerical simulations. Salt concrete exhibits a complex mechanical behavior depending on the applied deviatoric stress level and the exposure time. On the one side it reacts linear-elastically to low deviatoric stresses and on the other side viscoplastically to deviatoric stresses once a particular stress level has been exceeded. In order to get the process of constitutive model selection and parameter calibration in chapter 4 across, the following subchapters introduce into the theoretical basis of plasticity at the beginning as the description of viscoplasticity bases upon fundamental concepts of plasticity theory. Further the theory for describing the time-dependent mechanical behavior (creep and relaxation) is pictured.

2.1 INTRODUCTION IN THE PLASTICITY THEORY

In the past decades several laboratory tests revealed that different materials, i.e. hard soils, rocks, concrete, and even bones have some characteristics in common with respect to their mechanical behavior. The *Fig. 2-1* depicts a generalized stress-strain-curve resulting from a uniaxial compression test (Zienkiewicz und Taylor 2003).

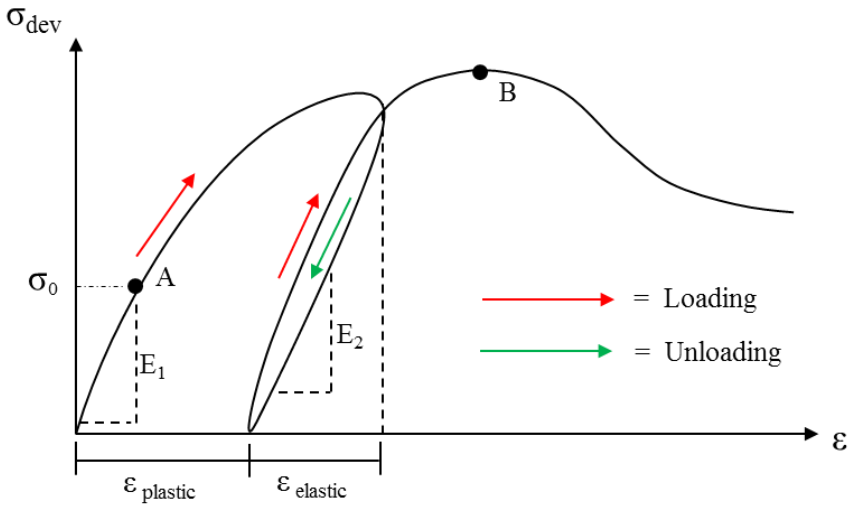

Fig. 2-1: Generalized stress- strain- curve obtained from a UC-test

At the beginning such materials deform roughly linearly when subjected to a constant deformation rate. Thus the materials exhibit an almost linear-elastic behavior under low deviatoric stresses. Then, at some point of the deformation process (indicated by σ_0 in *Fig. 2-1*), the materials start losing their initial stiffness and react to increasing deformations with non-linearly increasing stresses. The materials begin to behave “plastically”, noticeable by the gradually declining slope of the stress-strain-curve. Upon unloading elasto-plastic materials show a new branch in the stress-strain-curve. The new branch often exhibits a similar stiffness in comparison to the initial stiffness ($E_1 \approx E_2$). After complete unloading, elasto-plastic materials remain partially deformed as the plastic deformations are not recoverable (see $\varepsilon_{plastic}$). In *Fig. 2-1*, the stress value of point B represents the maximum deviatoric stress. Failure processes initiate from this point and greater deformations yield a stress reduction (Krabbenhöft 2002).

Resulting from the complexity of the above-mentioned behavior, different models were developed to idealize the observed behavior of elasto-plastic materials. For instance, the "Linear-Elasticity (LE)"- approach acts on the assumption that materials reacts portionally to deformations with stresses. Describing the behavior of some synthetic materials adequately, the LE-approach is only able to approximate the initial behavior of elasto-plastic materials. However the slope of the stress-strain-curve declines gradually from σ_0 (indicated in *Fig. 2-1* and *Fig. 2-2*) and this behavior cannot be captured by a model only basing upon the LE- approach.

The "Rigid-Perfectly Plastic (RPP)"- model ignores totally elastic stresses and assumes the exclusive development of plastic deformations when reaching σ_0 (compare yellow dashed line in *Fig. 2-2*). As the red dashed line in *Fig. 2-2* depicts, the "Linear Elastic-Perfectly Plastic (LEPP)"- model incorporates the LE- approach and the main idea behind RPP- model. Accordingly materials react perfectly-plastic once the deviatoric stress level has reached σ_0. This limit cannot be exceeded and represents the maximum strength. Consequently all stress levels below σ_0 yield a linear-elastic response (Krabbenhöft 2002).

A more sophisticated model is described by "Hardening-Elasto-Plasticity (HEP)". Within the HEP- model stresses are able to exceed σ_0 due to hardening effects (increase of stresses up to $\sigma_0(\alpha)$). The consideration of hardening enables to approximate the gradual decline of the slope after σ_0 (compare black line in *Fig. 2-2*). Elastic unloading takes place in case the deformations are reversed (depicted by the grey arrow in *Fig. 2-2*). The HEP- model is more sophisticated in comparison to the other mentioned models as the hardening requires additional history variables describing the current state of the material (indicated by α in *Fig. 2-2*) (Zienkiewicz und Taylor 2003b; Kelly 2015).

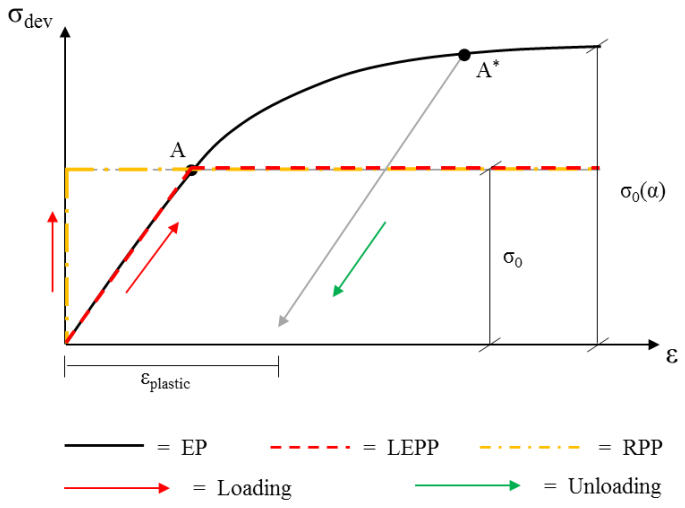

Fig. 2-2: Comparison of different material models /KEL 15/

The plasticity theory has been developed and successfully employed for many decades as most natural and industrially produced materials exhibit plastic deformations under loading. The adequate approximation of the highly complex deformation behavior of rocks, soils, concrete and granular materials has been allowed by means of the developed models. All presented plasticity models incorporate some fundamental concepts, e.g. the "yield function", the "flow rule" and the "consistency condition". Following subchapters explain elaborately these concepts.

2.1.1 YIELD CONDITIONS

As described before, σ_0 represents a transition point, at which plastic deformations start developing. It usually depends on the applied stresses and particular material parameters. Mathematically these assumptions can be merged in a general scalar function f that is known as the "yield function":

$$f(\boldsymbol{\sigma}, \boldsymbol{\alpha}) = f(\sigma_{11}, \sigma_{22}, \sigma_{33}, \sigma_{12}, \sigma_{23}, \sigma_{13}, \alpha_1 \dots \alpha_n) = 0 \quad \text{Eq. 2-1}$$

Where $\boldsymbol{\sigma}$ is the stress tensor containing the six independent stress components σ_{ii} and $\boldsymbol{\alpha}$ is a material tensor containing different material parameters α_i (further derived equations contain these material parameters as well, however they are omitted later). An alternative to describe the stress state of the material is the use of the principal stresses ($\sigma_1, \sigma_2, \sigma_3$). The principal stresses are the components of the stress tensor when the basis is changed in such a way that the shear stress components vanish. The principal directions can be included in the yield function if the loading direction is relevant for the material behavior, if anisotropic material is considered for instance:

$$f(\sigma_1, \sigma_2, \sigma_3, n_1, n_2, n_3) = 0 \quad \text{Eq. 2-2}$$

Where n_i are the principal directions, which inform about the orientation of the principal stresses relative to the reference system. Considering isotropic materials, the material response is independent of the direction of loading, so the principal directions are omitted:

$$f(\sigma_1, \sigma_2, \sigma_3) = 0 \quad \text{Eq. 2-3}$$

The yield function for isotropic material can alternatively be defined by stress invariants in the principal stress space. They are scalar quantities describing the stress state of the material. By definition the stress invariants are independent of the orientation of the reference system, likewise the principle stresses:

$$f(I_1, I_2, I_3) = 0 \quad \text{Eq. 2-4}$$

Where I_i are invariants of the stress tensor $\boldsymbol{\sigma}$. They are defined as follows:

$$I_1 = tr(\boldsymbol{\sigma}) \quad \text{Eq. 2-5a}$$

$$I_2 = \frac{1}{2}(\sigma_{ii}\sigma_{jj} - \sigma_{ij}\sigma_{ji}) \quad \text{Eq. 2-6b}$$

$$I_3 = \det(\sigma_{ij}) \quad \text{Eq. 2-7c}$$

From a geometrical point of view, yield functions describe a surface in the stress space. By this means the stress space is subdivided in an elastic and a plastic region. The *Fig. 2-3* illustrates an arbitrary yield surface in the two-dimensional principal stress space.

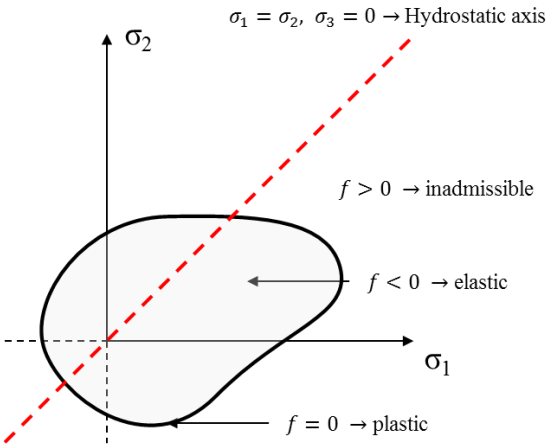

Fig. 2-3: Arbitrary yield surface in the two-dimensional stress space (Krabbenhöft 2002)

Considering the LEPP-model, which describes linear-elastic deformations below the yield point and perfectly-plastic deformations at the yield point, the *Fig. 2-3* depicts clearly three different cases: Due to the definition of the yield surface $f < 0$ is located inside the yield surface. Hence the material shows linear-elastic deformations. The case $f = 0$ represents a stress value on the yield surface, from which only perfectly-plastic deformations occur. The figure shows the case of $f > 0$ as well, however this is inadmissible (Krabbenhöft 2002; Kelly 2015).

2.1.2 LOADING/ UNLOADING CONDITIONS

Plastic loading alters *Eq. 2-5* in the following way:

$$f(\boldsymbol{\sigma} + d\boldsymbol{\sigma}) = f(\boldsymbol{\sigma}) + \nabla f^T d\boldsymbol{\sigma} = 0 \qquad \text{Eq. 2-5}$$

Where $d\boldsymbol{\sigma}$ is the stress increment tensor and the term ∇f is defined as:

$$\nabla f = \left[\frac{\partial f}{\partial \sigma_{11}}, \frac{\partial f}{\partial \sigma_{22}}, \frac{\partial f}{\partial \sigma_{33}}, \frac{\partial f}{\partial \sigma_{12}}, \frac{\partial f}{\partial \sigma_{23}}, \frac{\partial f}{\partial \sigma_{13}}\right]^T \qquad \text{Eq. 2-6}$$

Where the term ∇f represents the normal vector orthonormal to the yield surface. Moreover the incremental stress increase df must not result a displacement of the stress point to the outside of the yield surface. Thus:

$$df = \nabla f^T d\boldsymbol{\sigma} = 0 \qquad \text{Eq. 2-7}$$

Subsequently all changes in stresses d**σ** occur tangentially to the yield surface during plastic deformations (compare *Fig. 2-4*). This is considered by the consistency condition. The consistency condition yields the restriction that plastic strains are not able to occur outside the yield surface. In case of unloading the term df becomes smaller than zero and the stress point moves into the stress surface. Hence a redistribution of applied stresses causes exclusively either the development of elastic strains or a relocation of the stress point on the yield surface, which results plastic strains (Krabbenhöft 2002).

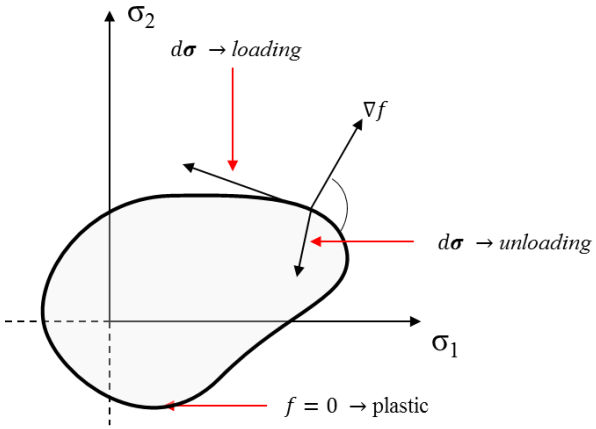

Fig. 2-4: Displacement of a stress point while plastic loading and unloading (Krabbenhöft 2002)

2.1.3 PLASTIC STRAINS

In case of soils, rocks and concrete, the yield criterion serves exclusively the purpose to identify, whether a material deforms elastically or plastically. It does not inform about the direction and the magnitude of plastic deformations (Krabbenhöft 2002; Kelly 2015). Since total strains in the plastic range cannot be determined by utilizing neither a linear nor another unique stress-strain-relationship, it is in common to exclusively consider the infinite small plastic strain increment $d\varepsilon^p$. In general the total strains $d\varepsilon^{tot}$ can be decomposed in the sum of the elastic and plastic strain increments:

$$d\boldsymbol{\varepsilon}^{tot} = d\boldsymbol{\varepsilon}^{e} + d\boldsymbol{\varepsilon}^{p} \qquad \text{Eq. 2-8}$$

Where $d\boldsymbol{\varepsilon}^{tot}$ is the total strain increment tensor, $d\boldsymbol{\varepsilon}^{e}$ is the elastic strain increment tensor, which bases upon a linear-elastic approach (e.g. linear elasticity after Hook), and $d\boldsymbol{\varepsilon}^{p}$ is the plastic strain increment tensor. It is derived from a plastic potential g:

$$d\boldsymbol{\varepsilon}^{p} = d\lambda \frac{\partial g}{\partial \boldsymbol{\sigma}} = d\lambda \, \nabla g \qquad \text{Eq. 2-9}$$

Where $d\lambda$ is the plastic multiplier and ∇g is the flow rule. In case of soils and rocks the plastic potential g can be assumed as a second surface in stress space (grey surface in *Fig. 2-5*), which is similarly defined as the yield function f before:

$$g(\boldsymbol{\sigma}) = g(\sigma_{11}, \sigma_{22}, \sigma_{33}, \sigma_{12}, \sigma_{23}, \sigma_{13}) = 0 \qquad \text{Eq. 2-10}$$

The flow rule defines the normal vector to g. The stress- space including the yield function f as well as the plastic potential g is illustrated in *Fig. 2-5*:

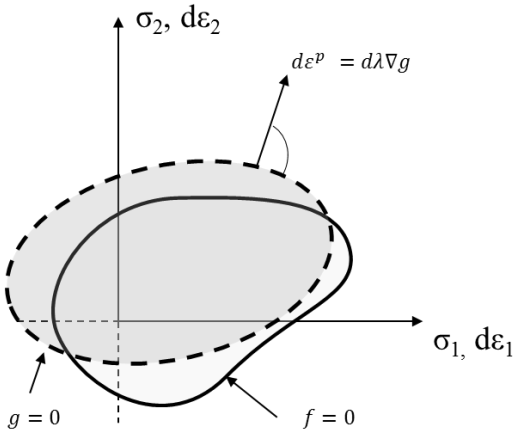

Fig. 2-5: Illustration of the relationship between flow rule and yield function (Krabbenhöft 2002)

The orientation of ∇g gives information about the direction of plastic strains, whereas the plastic multiplier dλ defines their magnitude. The clear distinction of strains is derived from a decomposition of dλ ∇g into a hydrostatic and a deviatoric part. This feature is depicted in *Fig. 2-6* in detail. :

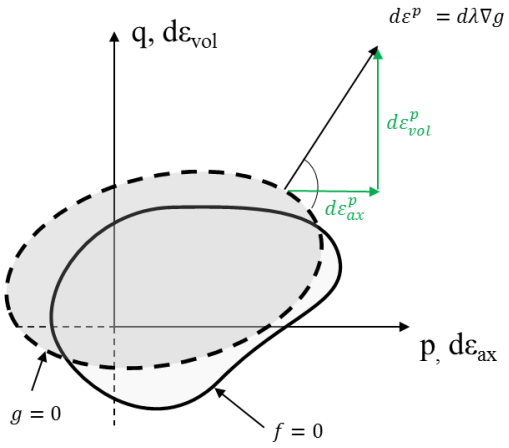

Fig. 2-6: Depiction of decomposition of $d\boldsymbol{\varepsilon}^p$ in a hydrostatic and a deviatoric part (Wieczorek 2010a)

In general the yield function f as well as the plastic potential g are determined by laboratory test evaluations. However the prediction of the plastic potential often represents a challenging task. For instance the volumetric strain development of metals is sufficiently approximated by means of using the same function for f and g. Nevertheless, when applying an associated flow rule to concrete, rocks, soils and granular materials, the associated flow rule causes too high volumetric strains. In order to predict smaller volumetric strains it makes sense to employee a non-associated one. That means the yield function and the plastic potential are two different functions (Krabbenhöft 2002).

2.1.4 HARDENING

In general hardening can be interpreted as an evolution of the yield. Within the previously described HEP-model, materials provide an initial yield surface (elastic limit envelope) that is closely related to the limit of the elastic domain. Further this assumption claims the intactness of the materials, so they must not be subjected to plastic loading before. However, when the applied stress level touches the initial yield surface, the elastic limit shifts into the plastic range due to an alteration in the microstructure. Hence the elastic domain changes either its size or position or orientation or a combination. During plastic loading, the intermediate state of the shifting elastic limit is called loading surface. The description of material failure is given by the maximum possible elastic domain. The failure surface (strength envelope) represents the largest possible resistance of the material. It is the point at which the change in microstructure yields a macroscopic exhaustion of the load carrying capacity of the material. Apart from some exceptions, many materials do not show an entire structural collapse by touching the failure surface. The magnitude of applied stresses decreases while the strains just slightly increases. In other words, the elastic limit contracts or the stress- strain- curve "turns down" (Kelly 2015; Zienkiewicz und Taylor 2003).

The process of strain hardening can be classified into four different kinds, as it was mentioned before. In contrast to isotropic strain hardening, where the elastic limit envelope increases in size, but remains at its origin, the elastic limit envelope shifts from the origin to another point within the stress space during kinematic hardening. However, the envelope remains its original size. In order to reproduce the real experiment data, it is convenient to combine isotropic with kinematic hardening. The process of rotational hardening represents an even more sophisticated approach to describe complex material behavior in plasticity theory. It postulates a rotation of the limit elastic envelope around one axis, however it remains at its origin with the initial size (Jirásek 2002).

2.1.4.1 ISOTROPIC HARDENING

As already described, isotropic hardening increases the yield limit during plastic loading.

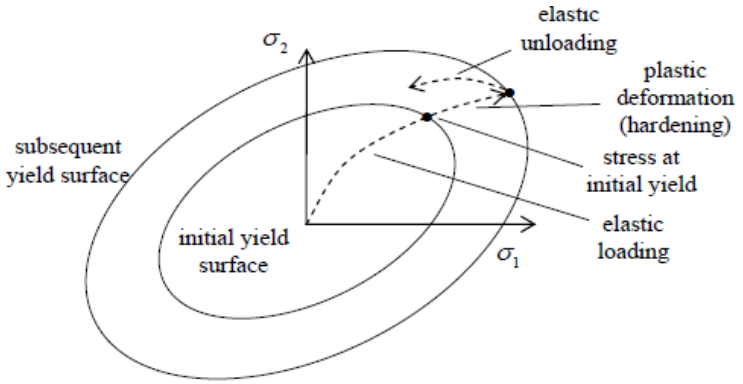

Fig. 2-7: Isotropic hardening (Kelly 2015)

The description of the yield surface evolution is only considerable by including at least one new hardening variable. The already mentioned state variable α is employed in the following passages in order to introduce in the theory of isotropic hardening. A yield criterion including isotropic hardening can mathematically be assumed as:

$$f(\boldsymbol{\sigma}) - \sigma_0(\alpha) = 0 \qquad \text{Eq. 2-11}$$

Where f(**σ**) is the yield function and $\sigma_0(\alpha)$ is the yield stress, whose evolution depends on the state varibale α. The simplest one-dimensional model is depicted in *Fig. 2-8*. Small deformations yield low, linearly increasing stresses (indicated in *Fig. 2-8* by the Young's modulus E). Upon passing the elastic limit the stress increase is related to the smaller tangent modulus E_t.

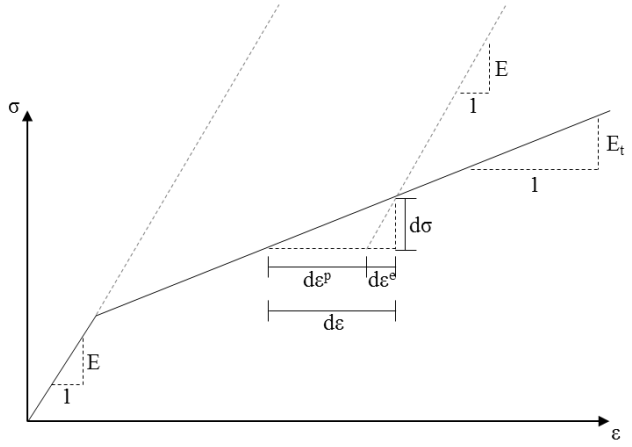

Fig. 2-8: Uniaxial compression test with linearly developing hardening (Krabbenhöft 2002)

In an incremental representation, the two relationships can be written as:

$$d\sigma = E d\varepsilon^e \qquad \text{Eq. 2-12a}$$

$$d\sigma = E_t d\varepsilon^{tot} \;\Leftrightarrow\; d\sigma = E_t(d\varepsilon^e + d\varepsilon^p) \qquad \text{Eq. 2-12b}$$

Where dσ is the stress increment, $d\varepsilon^e$ is the elastic strain increment, $d\varepsilon^p$ is the plastic strain increment, E is the Young's modulus and E_t is the tangent modulus. The total strain increment $d\varepsilon^{tot}$ is decomposed in the elastic $d\varepsilon^e$ and the plastic part $d\varepsilon^p$, as it is shown in *Eq. 2-12c* below:

$$d\varepsilon^{tot} = d\varepsilon^e + d\varepsilon^p \qquad \text{Eq. 2-12c}$$

A rearrangement of *Eq. 2-12a* and subsequent insert in *Eq. 2-12b* yield an elimination of the elastic strain increment $d\varepsilon^e$:

$$d\sigma = E_t\left(\frac{d\sigma}{E} + d\varepsilon^p\right) \qquad \text{Eq. 2-13}$$

A further rearrangement leads to:

$$d\varepsilon^p = \left(\frac{1}{E_t} - \frac{1}{E}\right) d\sigma \qquad \text{Eq. 2-14a}$$

or:

$$d\sigma = \frac{1}{\left(\frac{1}{E_t} - \frac{1}{E}\right)} d\varepsilon^p \qquad \text{Eq. 2-14b}$$

Following the term in front of the plastic strain increment is defined as H, thus:

$$d\sigma = H d\varepsilon^p \qquad \text{Eq. 2-15}$$

Where H is the plastic modulus. Isotropic hardening includes the consideration that an increase in stress above the elastic limit is equivalent to an increase in yield stress, so:

$$\frac{d\sigma}{d\varepsilon^p} = \frac{d\sigma_0}{d\varepsilon^p} = H \qquad \text{Eq. 2-16}$$

Where $d\sigma_0$ is the yield stress increment. Resulting from *Eq. 2-16,* the state variable α in *Eq. 2-11* is replaceable by the plastic strain ε^p due to a recognizable functional relation of $\sigma_0(\varepsilon^p)$ in case of strain hardening plasticity. The equation of isotropic hardening (compare *Eq. 2-17*) applies exclusively to the one-dimensional case including linearly increasing plastic strains during hardening, for instance a uniaxial compression test (Krabbenhöft 2002):

$$\sigma_0 = H\varepsilon_{11}^p \qquad \text{Eq. 2-17}$$

Where σ_0 is the evolving yield stress and $\varepsilon^p{}_{11}$ is the vertical plastic strain. However, the description of the material state during plastic straining in the multi-dimensional case might represent a challenging task. Therefore, it is convenient to characterize strain hardening by the scalar variable of the cumulative plastic strains. A frequently employed state variable is the equivalent plastic strain increment defined as follows (Jirásek 2002):

$$d\varepsilon_{eq}^p = \sqrt{\left(\frac{2}{3} d\varepsilon^p : d\varepsilon^p\right)} \qquad \text{Eq. 2-18}$$

Where $d\varepsilon^p{}_{eq}$ is the equivalent plastic strain increment. The derivation of the equivalent plastic strain increment enables to modify *Eq. 2-15* in a way that the plastic strain increment $d\varepsilon^p$ can be substituted by the equivalent plastic strain increment $d\varepsilon^p{}_{eq}$. An integration of this term yields:

$$\sigma_0 = \int H d\varepsilon_{eq}^p \qquad \text{Eq. 2-19}$$

Where σ_0 is the evolving yield stress. It leads to the conclusion that, in case a material has exceeded the yield point and experienced hardening, the yield surface has expanded permanently and the generated plastic strains are not recoverable. In order to describe the real observed processes, a superposition of isotropic and kinematic hardening may be taken into account.

By considering the consistency condition, isotropic hardening can be included into an elasto-plastic stress-strain constitutive relation in the incremental form:

$$d\boldsymbol{\sigma} = \left(\mathbf{D} - \frac{\mathbf{D}\,\frac{\partial g}{\partial \boldsymbol{\sigma}} \left(\frac{\partial f}{\partial \boldsymbol{\sigma}}\right)^T \mathbf{D}}{H + \left(\frac{\partial f}{\partial \boldsymbol{\sigma}}\right)^T \mathbf{D}\,\frac{\partial g}{\partial \boldsymbol{\sigma}}} \right) d\boldsymbol{\varepsilon} \qquad \text{Eq. 2-20}$$

Where **D** is the elastic constitutive matrix. In case H is equal to zero, an elastic perfectly-plastic behavior is described (Krabbenhöft 2002).

2.1.4.2 KINEMATIC HARDENING

As previously mentioned, the theory of isotropic hardening alone might not describe more complex processes of plastic straining. Kinematic hardening considers a change of the position of the yield function within the stress space. For instance, in case a material has the same yield strength in tension and compression initially, it must not be taken for granted that the material has the same value after loading it into the plastic region and unloading it (Jirásek 2002; Kelly 2015).

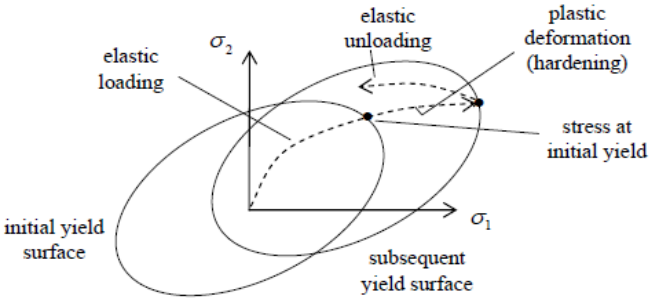

Fig. 2-9: Kinematic hardening (Kelly 2015)

In general the theory of kinematic hardening bases upon the assumption that the initial yield function shifts its origin during plastic loading. Mathematically the shift can be considered as an additional stress modifying *Eq. 2-11*:

$$f(\boldsymbol{\sigma} - \boldsymbol{\alpha}) - \sigma_0 = 0 \qquad \text{Eq. 2-21}$$

Where σ_0 is the initial yield stress. According to (Jirásek 2002) "$\boldsymbol{\alpha}$ is the so-called back stress that represents the center of the shifted elastic domain and plays the role of a tensorial hardening variable".

2.2 INTRODUCTION IN THE VISCOPLASTICITY THEORY

The *Fig. 2-10* shows the observed long-term behavior of salt concrete in a generalized form. In case (a) salt concrete continues deforming although the stress was kept constant and despite constant deformation the stress level has still declined in case (b).

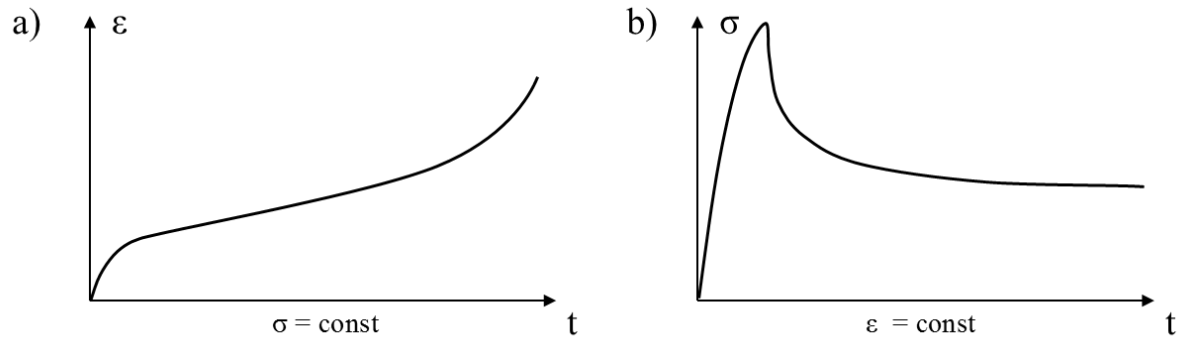

Fig. 2-10: Generalized time-strain-curve (a) and time-stress-curve (b)

To summarize the essential facts of chapter 2.1 briefly, the elastic domain shifts into the plastic domain when the applied stress level touches the initial yield surface. Hardening allows an expansion of the elastic domain by plastic straining, as far as the failure surface is touched. By definition the stress level is not able to go beyond the yield or failure surface. In classic plasticity theory, once the elastic domain expanded by plastic straining, the created strains are irreversible, so the material remains deformed in time. Thus the behavior of salt concrete may not be explicable by employing a constitutive model that bases exclusively upon an elasto-plasticity approach.

2.2.1 RATE-EFFECTS

Previous investigations of concrete and salt, e.g. mentioned in (Mehta und Monteiro 2006b), (Pajak 2011b) or (Düsterloh 2010b), also suggest a strong dependence of the maximal deviatoric strength on the deformation rate and loading rate respectively. The *Fig. 2-11* and *Fig. 2-12* attempt to illustrate these dependencies. The *Fig. 2-11* shows a two-dimensional stress space. The flow rule is assumed to be fully associated to the yield function. Contrary to hardening the initial yield surface is expanded by the applied rates in this case. Infinite high rates ($\dot{\varepsilon} = \infty$; $\dot{\sigma} = \infty$) induce an infinite high ultimate compressive strength and smaller rates ($0 < \dot{\varepsilon} < \infty$; $0 < \dot{\sigma} < \infty$) yield a lower ultimate strength consequently. Further a threshold exists ($\dot{\varepsilon} \approx 0$; $\dot{\sigma} \approx 0$), from which a reduction of the rate does not affect the ultimate compressive strength. The described dependency is not noticeable then and the material behaves rate-independent.

The classic plasticity theory does not provide an approach of dealing with the identified rate dependence. A frequently applied approach is the visco-plasticity theory, which enables the reproduction of rate-dependent effects of geomaterials (Zienkiewicz und Cormeau 1974).

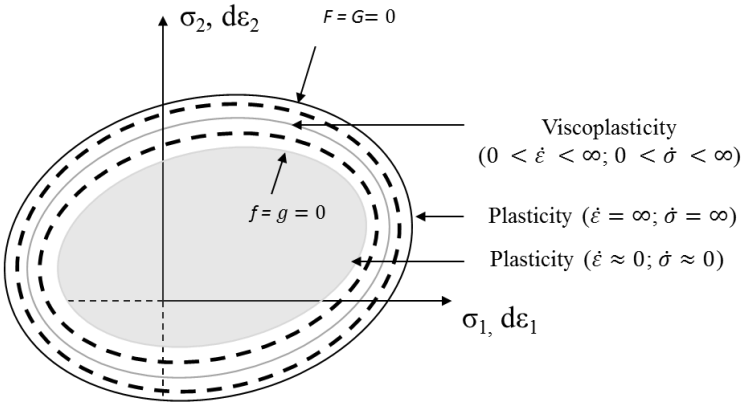

Fig. 2-11: Yield surface expansion by rate dependency (Chaboche 2009)

Within the viscoplasticity theory, the rate-independent yield surface is clearly distinguished from the rate-dependent yield surface. The rate-independent yield surface is depicted in *Fig. 2-11* by f. The yield surface f is the same, which has been defined in chapter 2.1 before.

The significant difference between the classic plasticity theory and the visco-plasticity theory is the assumption that the stress level is able to go beyond the initial yield surface for a particular time. Considering a material has been deformed by a specific deformation rate or stress rate. When keeping the deformation constant then, the distance between the rate-dependent and rate-independent yield surface reduces in time until f * reaches f (Etse et al. 2004). This is described by f and f * in *Fig. 2-12*. Among other influencing factors, the viscosity of the material causes mainly the overstress (Olivella und Gens 2002).

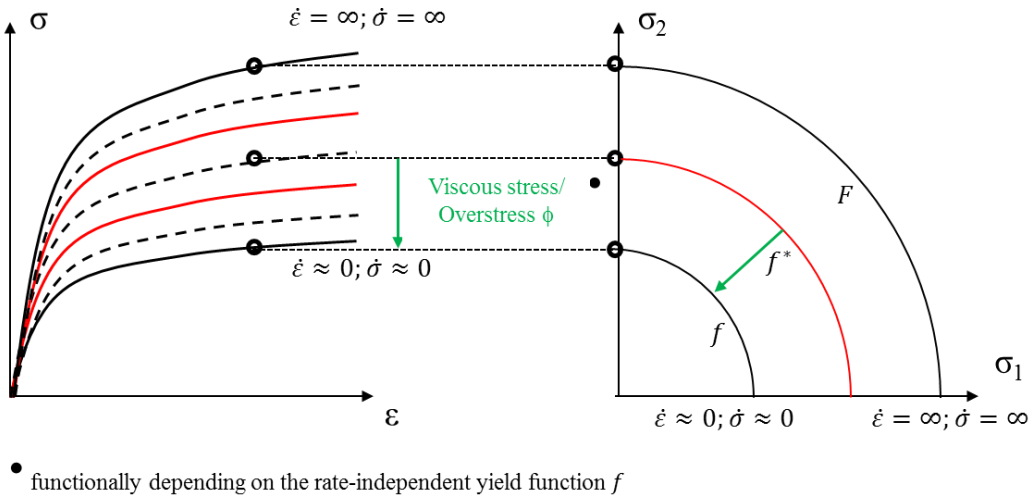

Fig. 2-12: Depiction of the overstress function (Chaboche 2009)

Likewise *Eq. 2-8*, the total strains can also be decomposed in two parts in case of viscoplasticity:

$$d\boldsymbol{\varepsilon}^{tot} = d\boldsymbol{\varepsilon}^{e} + d\boldsymbol{\varepsilon}^{vp} \qquad \text{Eq. 2-22}$$

Where $d\boldsymbol{\varepsilon}^{vp}$ is the viscoplastic strain increment tensor from the visco-plasticity theory.

The term $d\boldsymbol{\varepsilon}^{vp}$ is defined as follows:

$$d\boldsymbol{\varepsilon}^{vp} = \frac{1}{\eta}\langle\phi(f)\rangle\frac{\partial g}{\partial \boldsymbol{\sigma}} \qquad \text{Eq. 2-23}$$

Where η is the viscosity parameter and ϕ(f) is the overstress function, which depends on the rate-independent yield function f. The term $\langle\phi(f)\rangle\,\eta^{-1}$ is comparable to the plastic multiplier dλ within the classic plasticity theory. The McCaulay brackets indicate a distinction of two cases:

$$\langle\phi(f)\rangle = \begin{cases} \phi(f) & if\ \phi(f) \geq 0 \\ 0 & if\ \phi(f) < 0 \end{cases} \qquad \text{Eq. 2-24}$$

By this means the overstress function ϕ(f) is only considered as soon as the stress level goes beyond the rate-independent yield surface. It is convenient to use the following expression for defining the overstress function:

$$\phi(f) = \left(\frac{f - f_0}{f_0}\right)^N \qquad \text{Eq. 2-25}$$

Where f_0 is any convenient reference value of f in order to render the expression non-dimensional. N is a parameter, which should satisfy N ≥ 1 (Olivella und Gens 2002b). A frequently applied expression of a rate-dependent yield function is taken from (Heeres et al. 2002):

$$f^* = f - d\lambda\frac{\eta}{\phi} = 0 \qquad \text{Eq. 2-26}$$

Where f^* is the rate-dependent yield surface. As depicted in *Fig. 2-13*, the term $d\lambda\,\eta\,\phi^{-1}$ defines the difference between f^* and f.

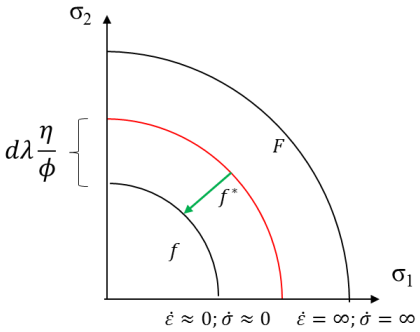

Fig. 2-13: Distance between rate-dependent and rate-independent yield surface according to (Heeres et al. 2002)

The elastoplastic yield condition F = 0 results from setting η equal to 0 (compare *Fig. 2-11*), so rate effects are completely neglected. Contrary an infinite high viscosity exclusively yields an elastic response for every possible stress state. This theoretical aspect accounts for the observed stress reduction of salt concrete in time (stress relaxation in *Fig. 2-10b*)

2.2.2 CREEP

Another observed phenomenon based upon material viscosity is creep. Creep is the inelastic response of materials when subjected to constant deviatoric stresses for a long period of time (Düsterloh 2010; Olivella und Gens 2002). Temperature affects significantly the creep process additionally, because microstructural defect arrangement processes are often accelerated at higher temperatures. Creep is affected by the viscosity of the material as the resulting deformations are directly associated to the exposure time of the stress (Olivella und Gens 2002). The typical strain-time curves obtained from creep tests at constant load and sufficiently long time often exhibit three characteristic stages that are depicted in *Fig. 3-12* (Düsterloh 2010):

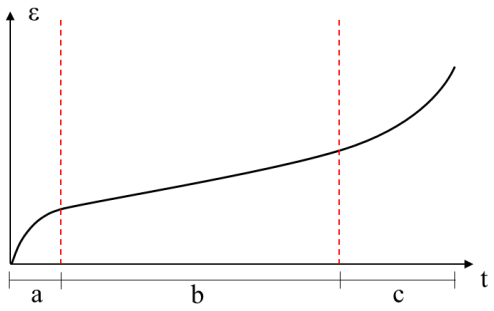

Fig. 2-14: Three characteristic stages of a creep test: a: Transient creep; b: Stationary creep; c: Tertiary creep

During the transient creep phase the material deforms rapidly but at a decreasing rate. Its duration in relation to the entire creep curve is relatively short (a). The strain rate reaches its minimum value within the stationary stage and remains approximately constant over a relatively long period of time (b). Finally the strain rate accelerates rapidly during tertiary creep (c). The rapture of the sample is not illustrated in *Fig. 2-14*.

As already mentioned, creep is closely related to microstructural processes taking place inside the material. Thus a continuum description of creep processes has proven to be useful for the adequate reproduction of these processes. According to (Olivella und Gens 2002) the creep of geomaterials can be approximated by employing a power law in the form of:

$$d\boldsymbol{\varepsilon}^{vp} = A(T)q^n \frac{\partial g}{\partial \boldsymbol{\sigma}} \qquad \text{Eq. 2-27}$$

Where n is the power of the rock creep law and q is derived from the second invariant of the stress tensor:

$$q = \sqrt{3I_2} \qquad \text{Eq. 2-28}$$

A(T) is a temperature-dependent parameter. Other forms of *Eq. 2-27*, like the approach presented in (Olivella und Gens 2002), were modified by replacing the term $A(T)q^n$ with a temperature dependent overstress function $\phi(f)\ \eta(T)^{-1}$. By this means the material viscosity is considered sufficiently.

3 PERFORMED EXPERIMENTS

The introduction chapter informed about the purpose and objectives of the carried out laboratory test program. Briefly repeated, the program was performed to determine the short- as well as the long-term mechanical behavior of salt concrete. Further laboratory tests concentrated on the hydraulic properties, especially the permeability development while loading. The utilized salt concrete samples were obtained from drill cores extracted from a sealing element described in 0. Due to the relative small amount of available salt concreate samples, some samples were used in different laboratory tests. In whole experiment data of nine triaxial compression tests (TC) and one uniaxial compression creep test (UCc) including five samples have been provided.

3.1 MATERIAL STABILITY: TRIAXIAL TESTING METHOD

Apart from a general determination of the material properties, the triaxial compression tests (TC-tests) pursued the objective to improve the knowledge about the onset of gas flux and development of permeability while loading (Czaikowski et al. 2016). Furthermore the need existed to identify the ultimate compressive strength as well as other mechanical material properties of this type of salt concrete. Finally nine specimen were selected and tested (compare *Tab. 3-1*).

Tab. 3-1: Samples used in TC-tests

Sample name:	T_0.68m	T_1.38m	P2	P5	P8
Sample name:	P10	P11	P12	P13	

3.1.1 SAMPLE PREPARATION AND EXPERIMENT LAYOUT

A turning lathe was used to shape cylindrically the samples with coplanar faces before performing the TC-tests. Finally the length and diameter of all samples were L = 0.14 m and D = 0.07 m respectively, thus the samples were prepared following international standards and recommendations (Düsterloh 2010). The *Tab. 3-2* lists average values of sample weight, density, porosity and water content, which have been determined before testing.

Tab. 3-2: Details of salt concrete samples (TC-test)

Average weight $\bar{m}$ [g]	Average density $\bar{\rho}$ [g cm³]	Average porosity $\bar{\phi}$ [-]	Average water c. $\bar{w}$ [%]
1113.68	2.07	0.06	0.02

The *Fig. 3-1* illustrates schematically the principle design of the employed TC-test-cell. In general one cylindrical sample is laterally covered by a tube made up of rubber. Then the sample surrounded by the tube is assembled inside the triaxial cell. The cell is composed of a steel piston and a vessel. During the test, the sample is axially loaded by the steel piston and the vessel is filled with oil. By controlling the oil pressure inside the cell, the confining stresses are adjusted. Furthermore the amount of emitted oil is used to determine the created volumetric strains afterwards (Düsterloh 2010). In case of the employed TC-cell, axial deformations were

measured by using displacement-transducer (LVDT). They were installed outside of the cell. Volumetric strains were directly detected by the determination of emitted oil and indirectly by using strain gauges. They were laterally attached at half sample height. In order to detect changes of permeability induced by mechanical loading, nitrogen gas was injected at the bottom side of the sample and the outflowing gas was measured at the opposite side. The amount of outflowing gas was continuously recorded by a burette (Czaikowski et al. 2016).

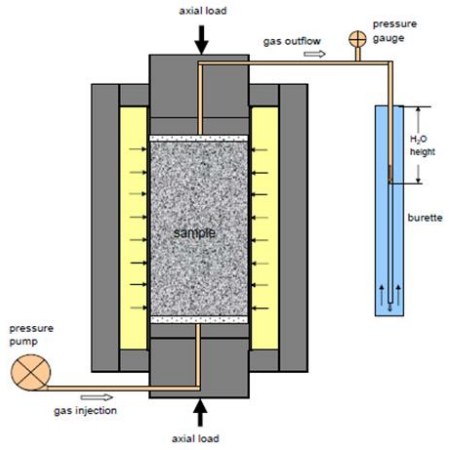

Fig. 3-1: Principle of triaxial compression tests with permeability measurement (Wieczorek 2010b)

Fig. 3-2: Steel vessel for individual oil pressure built-up on a salt concrete sample

3.1.2 TESTING METHOD

The TC-tests were carried out in two steps. In the initial phase an isotropic stress state of σ_{Iso} = 5 MPa was created by applying a stress rate of $\dot{\sigma}$ = 1 MPa/ min. The stress state has been kept constant for 22 hours then. After 22 hours, the isotropic stress state was increased to σ_{Iso} = 20 MPa twice within two hours. The samples were completely unloaded after 24 hours in total. The pre-compaction phase rather served the purpose to reach the state of compaction that the samples had before extraction from the drift seal than inducing a permeability reduction due to healing. The second step of the TC-test was the creation of a deviatoric stress state, which caused the failure of the samples finally. This part of the TC-tests was carried out under strain control. A deviatoric stress state was created by gradually deforming the samples in axial direction while keeping the confining stress constant. Each sample was subjected to a particular confining stress. The *Tab. 3-3* lists each sample with its corresponding confining stress:

Tab. 3-3: Samples with corresponding confining stresses

Sample name		T_0.68m	T_1.38m	P2	P5	P8
σ_3	[MPa]	4.0	1.0	2.0	2.0	5.0

Sample name		P10	P11	P12	P13
σ_3	[MPa]	3.0	5.0	3.0	1.0

According to (Czaikowski et al. 2016) the outflow of the axially injected nitrogen gas has constantly been measured during the experiment to determine a change of permeability.

3.1.3 MEASUREMENT RESULTS

Since the experiments were identically carried out, only varying in confining stresses, one experiment has been chosen in order to present the obtained experiment results exemplarily. The experiments including loading and unloading cycles to determine the young's modulus have not been taken into consideration, i.e. T_0.68m, P11 and P12. The experiment results of P5 have finally been chosen, because the results are well representative. The presentation of experiment results is limited to the evolving deviatoric stresses as well as volumetric strains. The results of the permeability measurement are not considered. Following the sign convention in geotechnics, compressive stresses as well as compressive strains are depicted with a positive prefix. In the upper part the *Fig. 3-3* shows the real applied deformation rate, whereas the resulting deviatoric stresses are illustrated in the lower diagram. The applied deformation rate was $\dot{\varepsilon}_{ax}$ = 3.1e-5 1/s. Confined by a radial stress of σ_{rad} = 2 MPa, the deviatoric stress increased up to a stress level of $\sigma_{max\ dev}$ = 38 MPa. Finally the sample failed at an axial strain of ε_{ax} = 2.75 %. After a phase of volume reduction, which means a compaction of the sample, the volumetric strains started increasing upon passing an axial strain of ε_{ax} = 0.65 %. This indicates the initialization of micro fissure development that coincides with an increase of porosity within the material. The volumetric strains changed when subjecting the sample to a stress of $\sigma_{dilatancy}$ = 33 MPa. The volumetric strains reached a maximum level of about ε_{vol} = 1.3 % (compare *Fig. 3-4*).

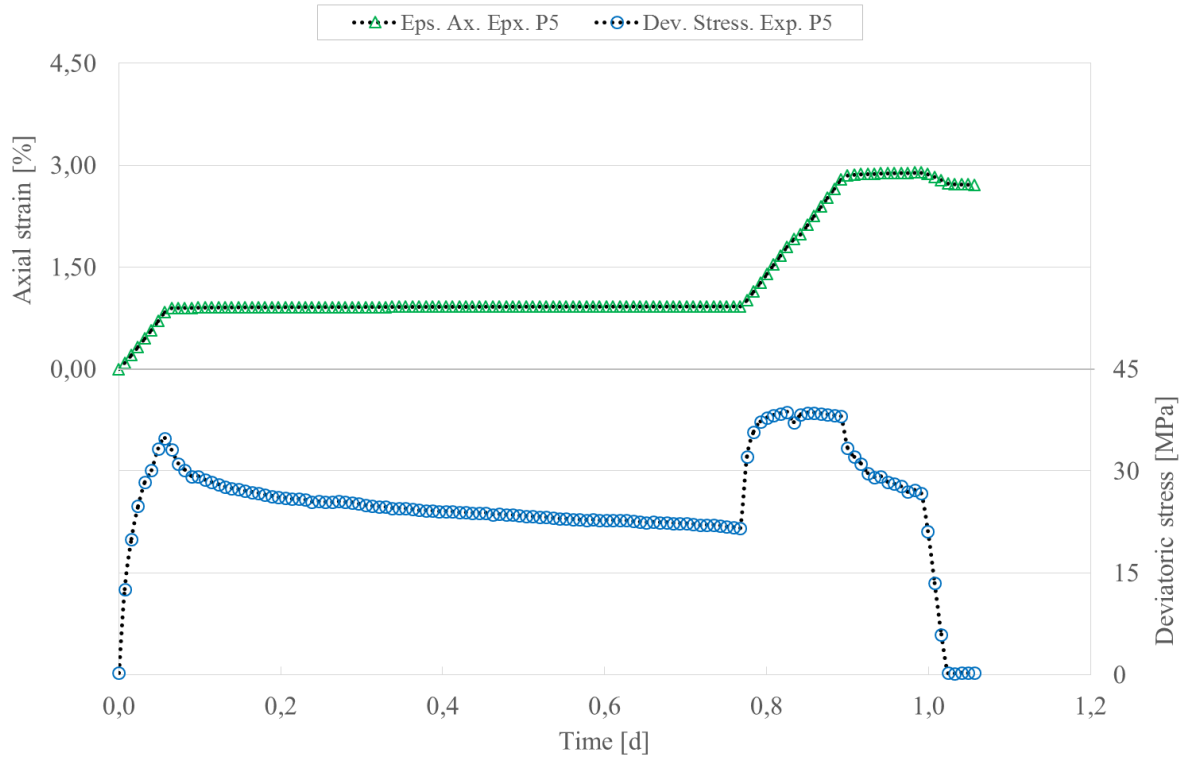

Fig. 3-3: Axial strain application and evolving deviatoric stresses in time

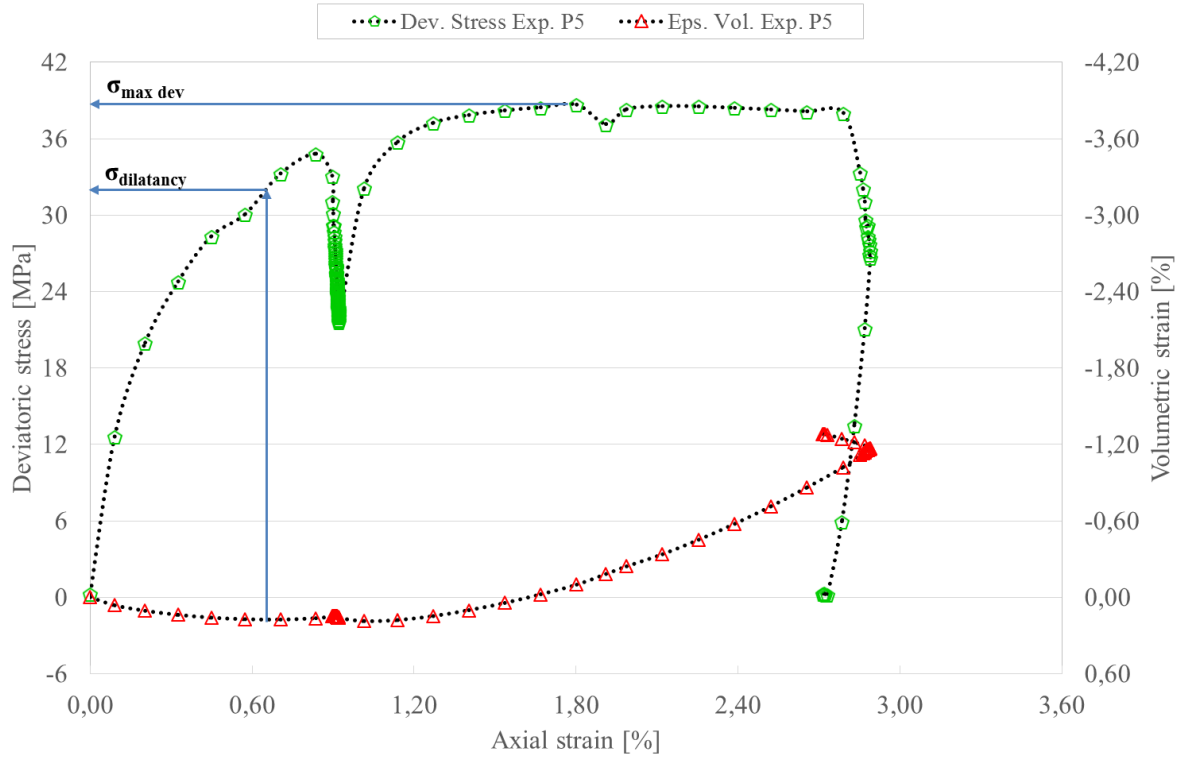

Fig. 3-4: Evolution of deviatoric stresses and volumetric strains
(The maximum deviatoric stress as well as the dilatancy point are depicted)

3.1.4 INTERPRETATION

In general the performed TC-tests revealed similar results compared to the results described within the introduction and (Czaikowski et al. 2016). As already determined in previous works, salt concrete exhibits linear-elastic deformations under low deviatoric loading and plastic deformations under high deviatoric loading. Focusing on the end of the strain-stress curve in *Fig. 3-4*, it was intended to perform an unloading/ loading cycle. Hence the reversible elastic strains can clearly be distinguished from the irreversible plastic ones. Furthermore the maximum deviatoric stress of salt concrete shows a strong dependence on confining stresses. For instance, sample P5 failed when reaching a stress value of about $\sigma_{fail\ dev}$ = 38 MPa, whereas sample P10 failed at a stress of about $\sigma_{fail\ dev}$ = 41 MPa. This outcome seems reasonable, because the sample P10 was confined by a radial stress of σ_{rad} = 3 MPa (compare *Fig. Appendix A-2* and *Fig. Appendix A-4*). Not only the maximum deviatoric stress depends on the confining stresses, but also the dilatancy boundary is shifted to higher axial strains when applying higher confining stresses. Consequently the porosity within the salt concrete sample reduces more.

One significant point, which has been revealed during the performed permeability measurements, is the influence of the material viscosity. Assuming the case, salt concrete is a stiff material, the deviatoric stress would only decrease slightly, when keeping the deformations constant for the time of permeability measurement. However a non-negligible stress-relaxation is noticeable in the lower part of *Fig. 3-3.* This stress relaxation is evidence of the moderate viscosity of salt concrete.

3.2 LONG-TERM DEFORMATION BEHAVIOR: UNIAXIAL TESTING METHOD

The uniaxial compression creep test (UCc-test) aimed at investigating the time-dependent uniaxial deformation behavior of salt concrete. Five samples were finally selected in order to carry out the UCc-test, which are listed in *Tab. 3-4* below:

Tab. 3-4: Selected samples for performing the UCc-test

Sample name:	1048	1049	1050	1051	1052

3.2.1 SAMPLE PREPARATION AND EXPERIMENT LAYOUT

Except from the different dimensions, the specimen utilized in the UCc-test were prepared as described in chapter *3.1.1*. The length and diameter of the five samples were L = 0.16 m and D = 0.08 m respectively. The *Tab. 3-5* lists average values of sample weight, density, porosity and water content, which have been determined before testing:

Tab. 3-5: Details of salt concrete samples (UCc-test)

Average weight $\bar{m}$ [g]	Average density $\bar{\rho}$ [g cm³]	Average porosity $\bar{\phi}$ [-]	Average water c. $\bar{w}$ [%]
1664.68	2.07	0.06	0.02

With respect to the experiment layout, a UC(c)-test represents a special kind of TC(c)-test, because the applied confining stress σ_3 is equal to the surrounding atmospheric pressure. Thus a vessel filled with oil is not required to control the confining stresses. Subsequently the samples are exclusively affected by the stresses created by the steel piston. In comparison to short-term compression tests, creep tests last a greater span of time. Due to a limited span of time and the statistical need to examine the properties of several samples, test rigs were developed, which enable to test up to five samples simultaneously. Before using this kind of apparatus, it has to be ensured that the material properties of the tested samples are similar. According to (Düsterloh 2010) a correct adjustment of the axial load acting on each sample cannot be guaranteed elsewise.

In case of the employed apparatus, the axial deformations of each sample were measured by using displacement transducers (LVDT). Furthermore all samples were equipped with strain gauges, which were directly attached to the sample surface. The gauges pursued the objective to determine axial as well as radial deformations.

3.2.2 TESTING METHOD

In contrast to the TC-test, creep tests are performed stress-controlled. Within the UCc-test the five samples have been subjected to three different deviatoric stress level for 341 days in whole. Initially the samples have been loaded with σ_{Ax} = 5 MPa for 76 days. Afterwards they have been exposed to σ_{Ax} = 10 MPa for 106 days and to σ_{Ax} = 20 MPa within the last phase. Since the temperature affects considerably creep properties in general, it was attempted to keep the temperature inside the laboratory constant. During the tests the temperature was around T = 25 °C (Czaikowski et al. 2016).

3.2.3 MEASUREMENT RESULTS

Following the sign convention in geotechnics, compressive stresses as well as compressive strains are depicted with a positive prefix. The upper part of *Fig. 3-5* illustrates the three different stages of applied deviatoric loading, whereas the lower part shows the response of each salt concrete sample to the stresses. After subjecting the samples to a deviatoric stress of σ_{Dev} = 10 MPa, the maximum axial strain observed was merely about 0.28 %. However, as soon as applying a deviatoric stress of σ_{Dev} = 20 MPa, a constant increase of the axial strains in time is noticeable. In order to compare the axial strains better, the axial strains of all five samples have been fitted to ε_{ax}= 0.16 % at the beginning of the third deviatoric stress phase (compare *Fig. 3-5*). It became evident, that the different samples have similarly deformed within the third phase. This assumption was checked by deriving the rates from the fitted axial strains. The great amount of measured data necessitated the application of smoothing methods to illustrate a trend within the experiment curves. A moving average method was chosen.

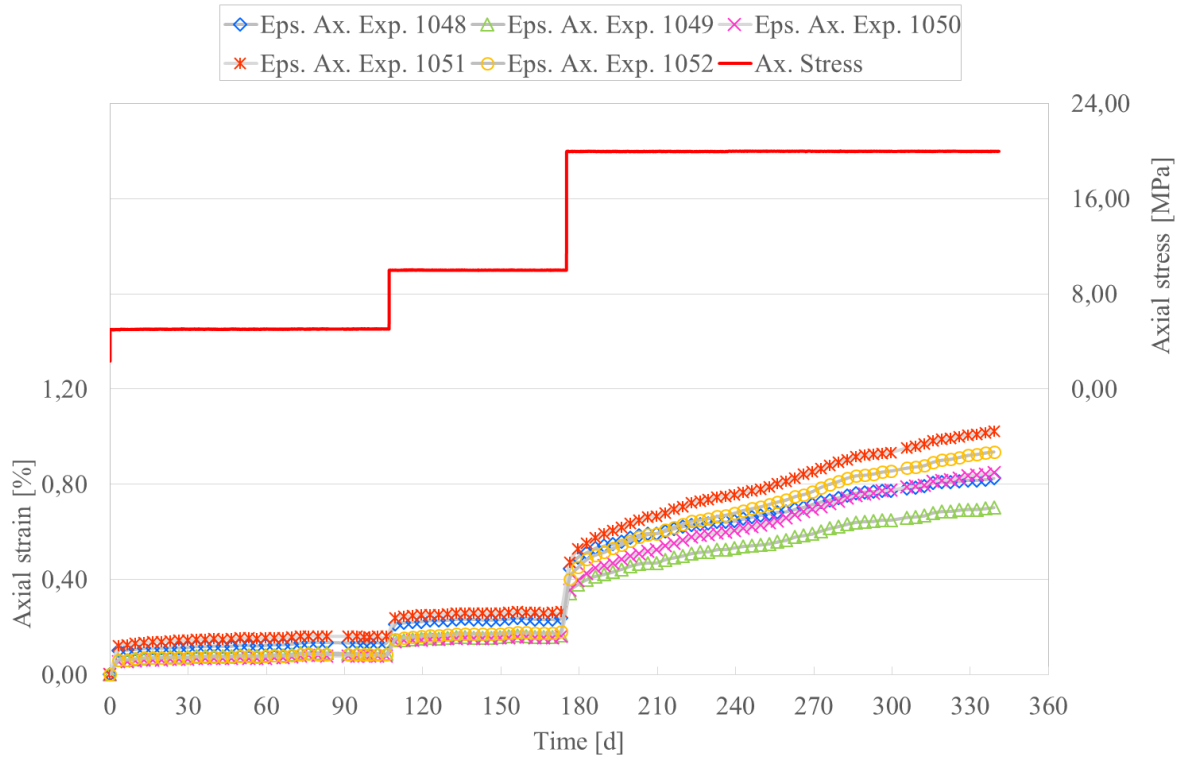

Fig. 3-5: Applied uniaxial stresses and corresponding axial strains

The *Fig. 3-7* informs about the average strain rate in each phase. Highlighted by green circles, transient creep deformations can be identified. Transient creep is defined as a disproportionate increase of deformations occurring within the initial time after raising the deviatoric stress. In contrast to transient creep, stationary creep deformations is exhibited when the strain rates tend to become constant (Düsterloh 2010). The red circle points clearly to non-negligible fluctuations of the strain rate, hence no stationary creep deformations are detected within the first and second deviatoric stress phase. However stationary creep deformations are assumed in the third phase.

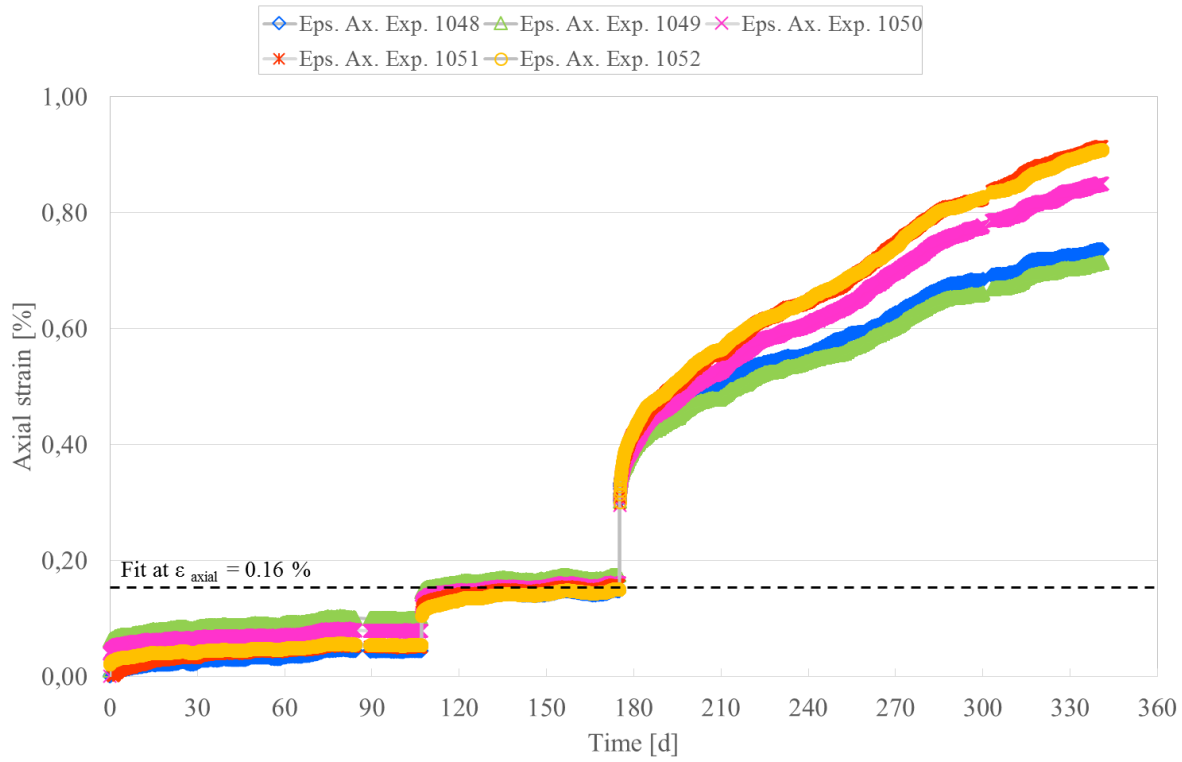

Fig. 3-6: Observed axial strains fitted at ε axial = 0.16 % (179 d)

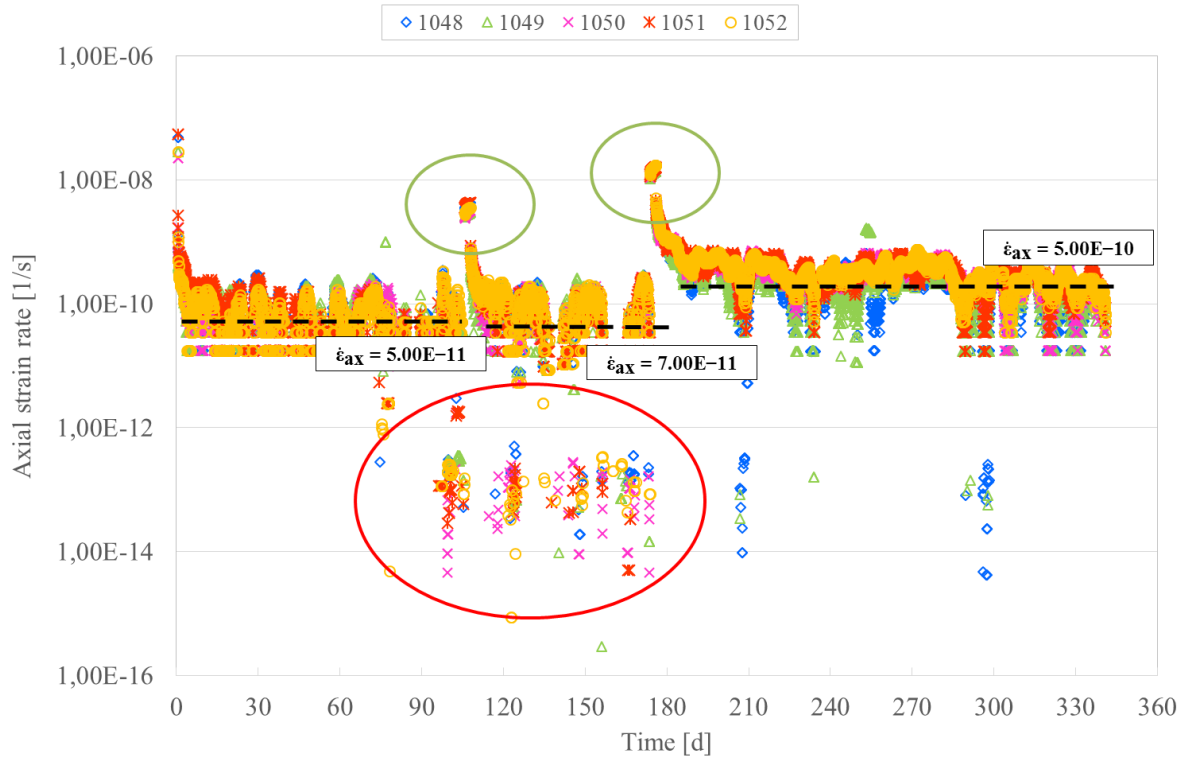

Fig. 3-7: Progress of axial strain rates calculated from the fitted axial strains in time

In *Fig. 3-8* the calculated axial strains are plotted against the axial strain rate. On the one side it is cognizable, that the strain rates occurring in the first phases have rapidly declined first and the samples stopped deforming fast second. Considering these two facts, stationary creep has not taken place. On the other side an evidence for stationary creep is provided in this figure,

because salt concrete samples have shown constant deformations for more than 150 days after exposing them to deviatoric stresses greater than 20 MPa.

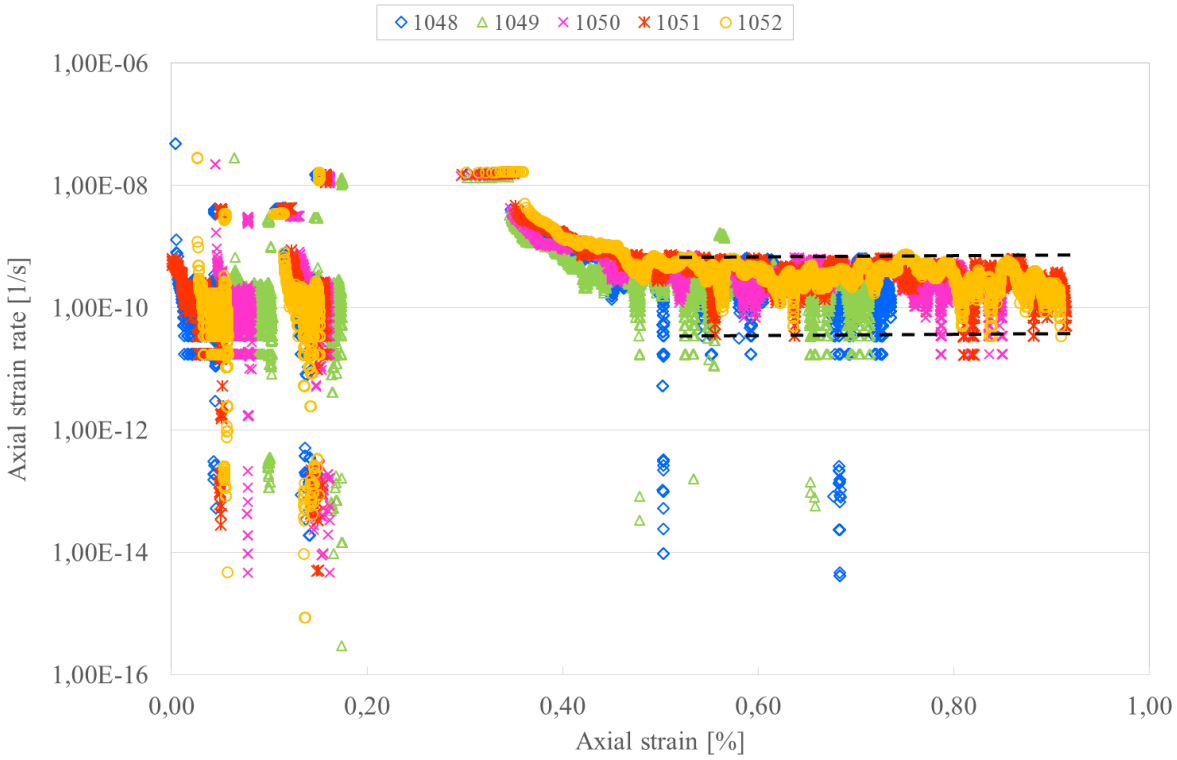

Fig. 3-8: Fitted axial strains vs axial strain rates calculated from the fitted axial strains

3.2.4 INTERPRETATION

The salt concrete incorporates the material properties of salt and cement, which becomes visible within the evaluated UCc-test. First it can be assumed, that the cement matrix of the salt concrete is able to resist deviatoric stresses below $\sigma_{Dev} \geq 20$ MPa. Hence the material deforms immediately after applying the load and deformations stagnate quickly, as it is shown by the declining rates in *Fig. 3-7*. This behavior is characteristic of concrete. Nevertheless the concrete matrix surrounding the salt grains seems to collapse partly when the applied stresses are increased up to $\sigma_{Dev} = 20$ MPa. Thereupon stress rearrangements take place within the salt concrete, so the salt grains are partly loaded. Consequently the material does not only exhibit elastic deformations, but also viscoplastic deformations due to the greater influence of the salt grains. When subjecting the salt concrete to greater deviatoric stresses for a longer period of time, viscoplastic behavior is expectable, e.g. stationary creep (Czaikowski et al. 2016; Middelhoff 18.08.2016).

4 CONSTITUTIVE MODEL SELECTION

Currently an advanced plasticity model is being developed for simulating the hydromechanical behavior of argillaceous materials. This advanced plasticity model is called visco-plasticity model henceforth. In accordance with (Mánica et al. 2016a) and (Mánica et al. 2016b) the visco-plasticity model is able to describe strain-hardening processes before peak, peak strength and post-peak softening. Further the results of (Middelhoff 18.08.2016) revealed the applicability of the implemented creep law. Although some drawbacks were detected, the modified form of Lemaitre's law yielded sufficient results. In general the model is able to describe short- and long-term deformations due to a decomposition of total strains into three terms:

$$d\boldsymbol{\varepsilon}^{tot} = d\boldsymbol{\varepsilon}^{e} + d\boldsymbol{\varepsilon}^{p} + d\boldsymbol{\varepsilon}^{c} \qquad \text{Eq. 4-1}$$

Where $d\boldsymbol{\varepsilon}^{tot}$ is the total strain increment tensor, $d\boldsymbol{\varepsilon}^{e}$ is the elastic strain increment tensor, $d\boldsymbol{\varepsilon}^{p}$ is the plastic strain increment tensor and $d\boldsymbol{\varepsilon}^{c}$ is the creep strain increment tensor. The elastic strain increment tensor $d\boldsymbol{\varepsilon}^{e}$ refers to the initially occurring elastic deformations. In case the initial yield surface is reached and stress level shifts the initial yield surface into the plastic domain, plastic deformations develop. The plastic straining is taken into account by the plastic strain increment tensor $d\boldsymbol{\varepsilon}^{p}$. By combining $d\boldsymbol{\varepsilon}^{e}$ and $d\boldsymbol{\varepsilon}^{p}$, the model is able to reproduce the short-term deformation behavior. To consider the long-term deformations properly, the third term $d\boldsymbol{\varepsilon}^{c}$ describes an independent deformation mechanism associated with creep. In this way long-term creep processes are reproduced adequately. Thus the model is not only able to describe the behavior of argillaceous materials, but also to reproduce the entire deformation behavior of materials, which exhibit similar deformation characteristics.

Nevertheless the visco-plasticity model considers exclusively homogenized materials. Hence the model neglects matrix, bonds and voids, which are major parts of a multi-component material, like argillaceous rocks, compacted soils and concrete.

4.1 SHORT-TERM RESPONSE

The first argument for selecting the visco-plasticity model evolved from the detailed evaluation of the performed TC-tests in chapter 3.1. Salt concrete does not seem to be comparable to argillaceous rocks due to the different composition. However the obtained results point to non-negligible similarities (compare *Fig. 4-1*). First salt concrete exhibits a significant stress-strain nonlinearity and plastic strains before reaching the peak strength (b in *Fig. 4-1*). The second point is the sudden loss of strength after peak (c in *Fig. 4-1).*

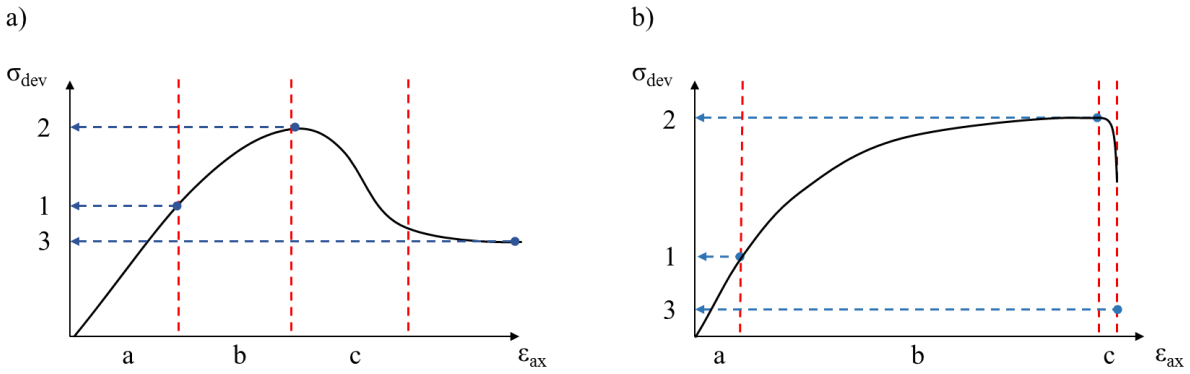

Fig. 4-1: Depiction of the short-term deformation behavior: a): argillaceous material; b) salt concrete; a: linear elastic branch; b: hardening branch; c: softening branch
1: Elastic limit/ Yield point; 2: Failure point; 3: Residual strength point

A modified Mohr-Coulomb-yield criterion was employed as the yield function for the model.

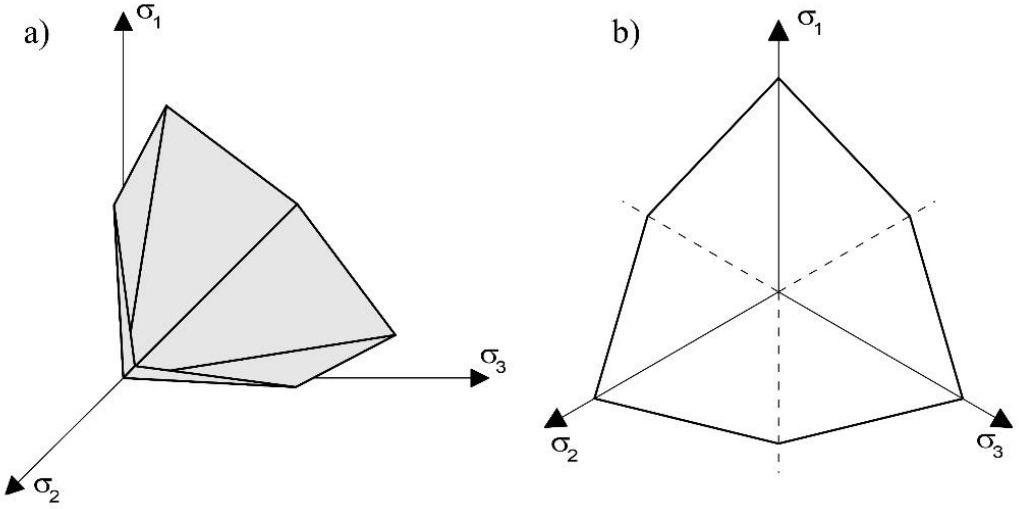

Fig. 4-2: Yield surface plotted in principal stress space (Mánica et al. 2016a)

When considering a three-dimensional principal stress space (σ_1, σ_2 and σ_3), the yield surface is illustrated as a cone with a hexagonal cross section in the deviatoric stress plane (compare *Fig. 4-2*, *Fig. 4-3* and *Fig. 4-4*). Mathematically the Mohr- Coulomb yield surface can be described by *Eq. 4-2*:

$$f = \left(\cos\theta + \frac{1}{\sqrt{3}}\sin\theta\sin\varphi\right)J - \sin\varphi\,(c\cot\varphi + p) = 0 \qquad \text{Eq. 4-2}$$

Where φ is the friction angle and c is the cohesion. A large variety of stress invariants are available to formulate the yield function. A set of invariants frequently employed in geomechanics are p, J and θ.

$$f(p,J,\theta) = 0 \qquad \text{Eq. 4-3}$$

The invariants are defined as follows:

$$p = \frac{1}{3} tr(\boldsymbol{\sigma}) \qquad \text{Eq. 4-4a}$$

$$J = \sqrt{\left(\frac{1}{2} tr\mathbf{S}^2\right)} \qquad \text{Eq. 4-4b}$$

$$\theta = -\frac{1}{3}\sin^{-1}\left(\frac{3\sqrt{3}\det\mathbf{S}}{2J^3}\right) \qquad \text{Eq. 4-4c}$$

Where **S** is the deviatoric stress tensor, which is defined as follows:

$$\mathbf{S} = \boldsymbol{\sigma} - p\mathbf{I} \qquad \text{Eq. 4-5}$$

Where **I** is the identity matrix. This set of stress invariants were chosen as they have a direct physical interpretation.

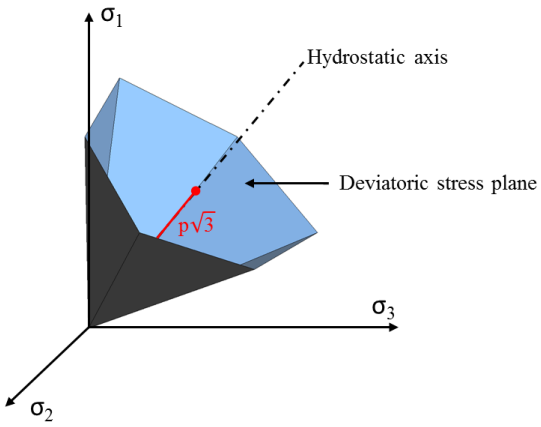

Fig. 4-3: Hexagonal Mohr-Coulomb yield surface in the principal stress space (including an illustration of p)

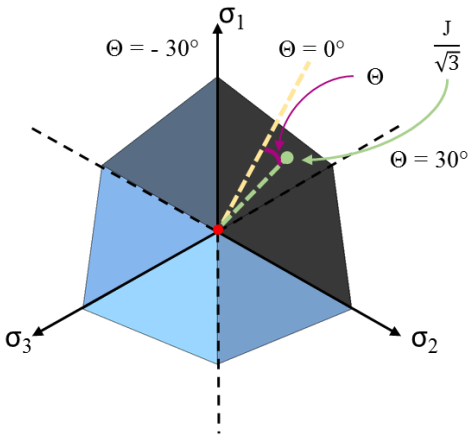

Fig. 4-4: Hexagonal Mohr-Coulomb yield surface in the principal stress space (top view including illustrations of θ and J)

As a brief summary, the principal stress coordinate system (σ_1, σ_2 and σ_3) corresponds to the orientation in which the shear stresses vanish. For instance, the *Fig. 4-3* shows a principal stress coordinate system. The invariant p is depicted in this figure additionally as it describes the magnitude of the hydrostatic load located on the hydrostatic axis ($\sigma_1 = \sigma_2 = \sigma_3$). Hence the invariant p represents the hydrostatic component of the current stress state. Further planes are considered being situated perpendicular to the hydrostatic axis. The top view at one plane is presented in *Fig. 4-4*. For any given stress state lying in this plane, the distance between the point representing the stress state and the hydrostatic axis is related to the deviatoric stress. The stress invariant J is equal to the magnitude of the mentioned distance and represents the measure of the deviatoric stress thus. The relationship of the intermediate principal stress to the major and minor principal stresses controls the last invariant θ. It is also known as the Lode angle. As depicted in *Fig. 4-4*, the magnitude of the intermediate principal stress in relation to the minor and major principal stresses is indicated by the invariant θ.

The *Fig. 2-8* shows the effect of alteration processes on the strength of materials during plastic loading (compare E and E_t). A reduction of material strength involves an instantaneous or continuous change of the friction angle and cohesion. Within the visco-plasticity model, the mobilization of the friction angle φ_{mob} and cohesion c_{mob} is controlled by the state variable ε^p_{eq} (compare *Eq. 2-18*), defined as:

$$\boldsymbol{\varepsilon}^p_{eq} = \sqrt{\left(\frac{2}{3}\boldsymbol{\varepsilon}^p : \boldsymbol{\varepsilon}^p\right)} \qquad \text{Eq. 4-6}$$

The variable $\boldsymbol{\varepsilon}^p$ represents the plastic strain tensor. The mobilized friction angle φ_{mob} and cohesion c_{mob} are calculated stepwise from $\boldsymbol{\varepsilon}^p_{eq}$ in combination with strain-hardening and strain-softening parameters. The *Fig. 4-5* depicts the friction angle evolution within the strain-hardening and -softening. Corresponding evolution laws are listed in *Tab. 4-1*.

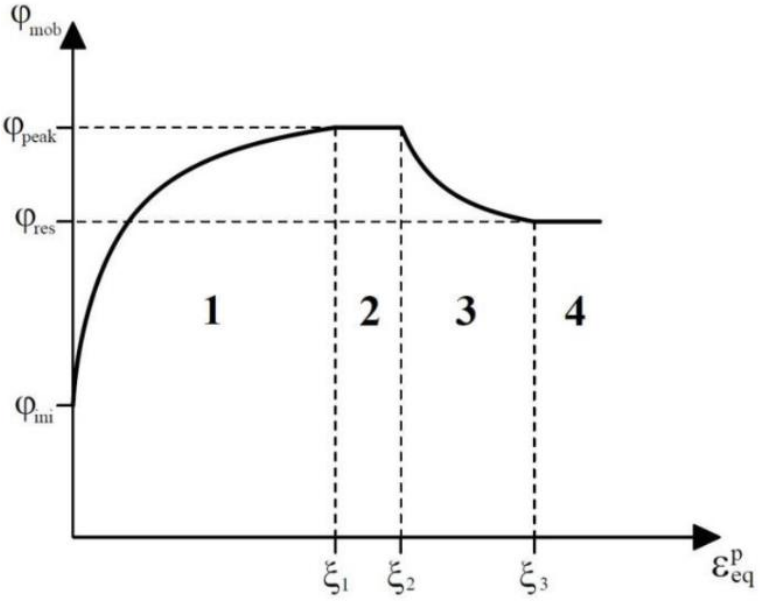

Fig. 4-5: Friction angle evolution including strain-hardening and strain-softening (Mánica et al. 2016b)

Tab. 4-1: Evolution laws of the mobilized friction angle corresponding to *Fig. 4-5*

Zone	Evolution law
Zone 1	$\varphi_{mob} = \varphi_{ini} + \frac{\varepsilon_{eq}^{p}}{a_{hard} + \frac{\varepsilon_{eq}^{p}}{\Delta\varphi_{hard}}}$; $\Delta\varphi_{hard} = \frac{\xi_1}{\frac{\xi_1}{\varphi_{peak} - \varphi_{ini}} - a_{hard}}$
Zone 2	$\varphi_{mob} = \varphi_{peak}$
Zone 3	$\varphi_{mob} = \varphi_{peak} - \frac{\varepsilon_{eq}^{p} - \xi_2}{a_{soft} + \frac{\varepsilon_{eq}^{p} - \xi_2}{\Delta\varphi_{soft}}}$; $\Delta\varphi_{soft} = \frac{\xi_3 - \xi_2}{\frac{\xi_3 - \xi_2}{\varphi_{peak} - \varphi_{res}} - a_{soft}}$
Zone 4	$\varphi_{mob} = \varphi_{res}$

The *Eq. 4-7* describes how the mobilized friction angle φ_{mob} is employed to calculate the corresponding mobilized cohesion c_{mob} afterwards:

$$c_{mob} = c_{peak} \cot\varphi_{ini} \tan\varphi_{mob} \qquad \text{Eq. 4-7}$$

Where c_{peak} is the peak cohesion and φ_{ini} is the initial friction angle.

As already mentioned, associated flow rules tend to overestimate volumetric strains in case of geomaterials, thus a non-associated flow was considered. The implemented flow rule was directly derived from the previously defined yield-criterion:

$$\frac{\partial g}{\partial \boldsymbol{\sigma}} = \omega \frac{\partial f}{\partial p}\frac{\partial p}{\partial \boldsymbol{\sigma}} + \frac{\partial f}{\partial J}\frac{\partial J}{\partial \boldsymbol{\sigma}} + \frac{\partial f}{\partial \theta}\frac{\partial \theta}{\partial \boldsymbol{\sigma}} \qquad \text{Eq. 4-8}$$

Where g is the plastic potential, ω is a constant, which controls the amount of plastic volumetric strains. Thus overestimation are countervailed. In case ω is set to 1, a completely associated flow rule is considered. Contrary no plastic volumetric strains occur when ω is set to 0.

4.2 LONG-TERM RESPONSE

The experiments revealed that viscoplastic deformations occur when subjecting salt concrete to higher deviatoric stresses for a long time (σ_{dev} > 20 MPa). The employed visco-plasticity model enables to reproduce time-dependent deformations caused by constant load as it incorporates a modified form of Lemaitre's creep law (Mánica et al. 2016b; Middelhoff and Czaikowski).

The *Eq. 4-1* can be reshaped to distinguish more clearly between the short-term and the long-term response determination. Then the total strain increment $d\boldsymbol{\varepsilon}$ can be decomposed in two mechanisms:

$$d\boldsymbol{\varepsilon}^{tot} = d\boldsymbol{\varepsilon}^{e} + d\boldsymbol{\varepsilon}^{p} + d\boldsymbol{\varepsilon}^{c} = d\boldsymbol{\varepsilon}^{ep} + d\boldsymbol{\varepsilon}^{c} = d\boldsymbol{\varepsilon}^{ep} + \Delta t\,(\dot{\boldsymbol{\varepsilon}}^{c}) \qquad \text{Eq. 4-9}$$

Where $d\boldsymbol{\varepsilon}^{ep}$ is the elastoplastic strain increment tensor related to the short-term response, $\dot{\boldsymbol{\varepsilon}}^{c}$ is the creep strain rate tensor, and Δt is the time increment. The approach assumes that creep deformations are mainly caused by deviatoric stresses. Thus the creep strain rates $\dot{\boldsymbol{\varepsilon}}^{c}$ are obtained by calculating:

$$\dot{\boldsymbol{\varepsilon}}^c = \frac{2}{3}\frac{\dot{\varepsilon}^c}{q}\mathbf{S} \qquad \text{Eq. 4-10a}$$

$$q = \sqrt{\left(\frac{3}{2}\mathbf{S}:\mathbf{S}\right)} \qquad \text{Eq. 4-10b}$$

$$\dot{\varepsilon}^c = \gamma\langle q - \sigma_s\rangle^n\left(1 - \varepsilon_{eq}^c\right)^m \qquad \text{Eq. 4-10c}$$

Where n and m are material constants, γ is a viscosity parameter and σ_s is a threshold parameter. The parameter γ controls the magnitude of initial viscoplastic strains, whereas the threshold parameter σ_s controls the activation of viscoplastic strains. The parameter ε^c_{eq} represents the state variable of the time-dependent response given by:

$$\varepsilon_{eq}^c = \int_0^t \sqrt{\left(\frac{2}{3}d\boldsymbol{\varepsilon}^p : d\boldsymbol{\varepsilon}^p\right)}\, dt \qquad \text{Eq. 4-11}$$

Where ε^c_{eq} are the equivalent creep strains and t is the time. By this means higher deviatoric stresses generate larger creep strain rates and these rates decrease as creep strains accumulated in time. An explicit scheme is utilized in the numerical implementation, so creep strains are computed from the deviatoric stress state at the beginning of the step (Mánica et al. 2016b).

4.3 THEORETICAL EMBEDMENT

The adequate reproduction of thermal-hydraulic-mechanically (THM) coupled processes in porous media represents a challenging problem (Olivella et al. 1996). The FEM- program Code_Bright provides a general formulation and a numerical approach to solve the governing equations within porous media (Olivella et al. 1994). Within the program the problem is formulated in a multiphase and multispecies approach. Porous materials, e.g. (un-)saturated soils, are considered to be composed of solid grains, water and gas. According to (Olivella et al. 1994) porous material are made up of three different species, which may coexist in three different phases. The *Tab. 4-2* responds to the mentioned phases and species in detail:

Tab. 4-2: Phase and specie description

		Abbrev.		Abbrev.		Abbrev.
Phase	Solid	s	Liquid	l	Gas	g
Specie	Solid	s	Water	w	Air	a

The Gas phase (g) exists as dry air and water vapor and the liquid phase (l) as water and dissolved air. In order to formulate the problem, some significant assumptions and aspects are taken into account. Since the performed numerical simulations deal with a pure mechanical problem, only the relevant assumptions are mentioned here //:

- The equation of momentum balance for the porous media is reduced to that of stress equilibrium in combination with a mechanical constitutive model. By this means stresses are related to strains. Further strains are obtained in terms of displacements.

- In case of deformations affecting the solid phase, only small strains or rather small strain rates are assumed. The transformation of the formulation in terms of material derivatives enables to omit advective terms due to displacements in the solid phase. Hence volumetric strain are adequately considered.

The governing equations for describing a non-isothermal multiphase flow of water and gas through a porous deformable media can be categorized into four groups (Tab. 4-3):

Tab. 4-3: Governing equations according to (Olivella et al. 1996)

Equation name	Example
Balance equation	Mass balance of solid, water and air; Stress equilibrium; Internal energy balance for the medium
Constitutive equation	Fick's law; Darcy's law; Mechanical constitutive model etc.
Equilibrium restriction	Solubility; Henry's law; Psychometric law etc.
Definition constraints	-

The visco-plasticity model represents a hydromechanical constitutive model for reproducing hydraulic-mechanically coupled processes. Nevertheless the recently performed simulations deal exclusively with the reproduction of the mechanical behavior of salt concrete //. Thus the balance equations, constitutive models and equilibrium restrictions implemented to reproduce the hydraulic coupling are not employed here. The used balance equations are described as follows:

- Mass balance of solid:

$$\frac{\partial}{\partial t}[\rho_S(1-\phi)] + \nabla \cdot (\mathbf{j}_S) = 0 \qquad \text{Eq. 4-12}$$

Where ρ_S is the density of the solid, ϕ is the porosity and $\mathbf{j}_s$ is the total mass flux of the solid. By eliminating the porosity variation caused by volumetric deformation and solid density, *Eq. 4-13* is obtained:

$$\frac{D_S\phi}{Dt} = \frac{1}{\rho_S}\left[(1-\phi)\frac{D_S\rho_S}{Dt}\right] + (1-\phi)\nabla \cdot \frac{d\mathbf{u}}{dt} \qquad \text{Eq. 4-13}$$

Where **u** are displacements. In order to perform the elimination of porosity variation, the material derivative with respect to the solid has been used and its definition is:

$$\frac{D_S(\bullet)}{Dt} = \frac{\partial}{\partial t} + \frac{d\mathbf{u}}{dt} \cdot \nabla(\bullet) \qquad \text{Eq. 4-14}$$

- Stress equilibrium:

$$\nabla \cdot \boldsymbol{\sigma} + \mathbf{b} = \mathbf{0} \qquad \text{Eq. 4-15}$$

Where **σ** is the stress tensor and **b** is the vector of body forces. By solving *Eq. 4-13* and *Eq. 4-15* in combination with constitutive model and equilibrium restrictions, the mechanical analysis can be performed. The main unknowns, which have to be determined by the analysis, are the displacements **u**.

5 NUMERICAL SIMULATIONS

The numerical simulations have been carried out by using the FEM- program Code_Bright. Due to revision and improvement processes the employed visco- plasticity constitutive model has not been implemented in the official version of Code_Bright yet. The programmers envisage including the model in the coming Code_Bright-version.

The numerical simulations aimed at generating one set of material parameters, which enables to reproduce the short- as well as the long-term deformation behavior of salt concrete. With regard to the simulation of the short- term behavior it is envisaged that the material parameter set describes the development of axial and volumetric strains first. Subsequently, the dilatancy point can be determined. The failure of the sample is another essential point. Second the material set should be able to reproduce time-dependent creep deformations. In order to calibrate the model, the results of the numerical simulations are compared with the experiment results from the TC- and UCc- tests.

Resulting from the complexity of the laboratory tests, the numerical simulations had to be simplified in terms of geometry, material, boundary conditions and time. In both numerical simulations the vessels including the steel piston have been omitted. Thus the applied stresses have directly horizontally and vertically been assigned to the simulated samples. In case of TC-tests the samples have vertically been subjected by a constant strain rate instead of vertical stresses. The salt concrete has been considered to be intact (without any micro- and macro fissures), absolute dry, isotropic and homogenized (disregard of salt concrete as a multi- component material). Also the laboratory temperature has been neglected. All basic assumptions are summarized in *Tab. 5-1*. Further test-specific assumptions are explained within the corresponding sections. It is believed that the major features of the laboratory experiments have sufficiently been preserved.

Tab. 5-1: Summary of basic assumptions for model simplification

	Assumption
1	Intact material (without any micro- and macro fractures)
2	Isotropic material
3	Homogenized material (Disregard of salt concrete as a multi-component material)
4	Absolute dry (Degree of saturation S = 0)
5	Disregard of temperature influence

The calculated vertical and horizontal displacements as well as vertical and horizontal stresses have been processed to compare the simulation results with the experiment ones. Information about data processing is given in *Appendix: Numerical simulations*.

5.1 SHORT-TERM RESPONSE: TRIAXIAL COMPRESSION TEST (TC)

Three TC- tests have been taken into account: T_1.38m, P5 and P10. The most important argument for excluding the other tests, like T_0.68m, was the amount of performed loading and unloading processes (“Loops”) during the test. These loading and unloading cycles are carried out in general to obtain the young’s modulus E. Nevertheless the development of a simulation

of these experiments would have been time-consuming and with respect to the material parameter calibration unnecessary. The evaluation of the remaining TC-tests points out that three of the samples have failed after axially deforming them by approximately ε = 3 %, one by 3.5 % and the last by 2.5 %.

Hence T_1.38m, P5 and P10 have exclusively been simulated. They have varied in confining stresses. The *Tab. 5-2* resumes the above mentioned information:

Tab. 5-2: Summary of previously selected experiments

Experiment name		T_1.38m	P2	P5	P10	P13
Confining stress	[MPa]	1	2	2	3	1
Simulated?		Yes	No	Yes	Yes	No

5.1.1 MAIN FEATURES OF THE NUMERICAL MODEL

The introduction of chapter 5 gives a rough overview of the previously considered simplifications. In detail the sample is exclusively simulated, whereas the rest of the surrounding apparatus is ignored. In order to remain as close to the real conditions as necessary, the model geometry is equal to the sample geometry. The sample is considered to be L = 0.14 m high and R = 0.035 m in radius. Due to the symmetry with respect to the center line, the sample is simulated axial symmetrically (compare *Fig. 5-1*).

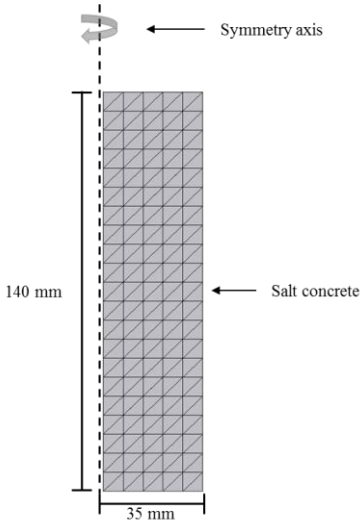

Fig. 5-1: Applied geometry including symmetry axis and model dimension

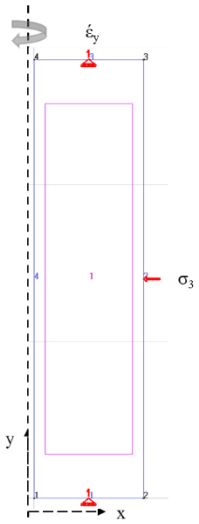

Fig. 5-2: Applied boundary conditions

The *Fig. 5-2* shows the applied boundary conditions. Horizontal displacements are allowed on the top as well as the bottom part of the sample. The horizontal stress is depicted by σ_3 in *Fig. 5-2*. A homogeneous stress distribution in horizontal direction can be created thereupon. After stress equilibrium, each sample is compressed by a deformation rate of $\dot{\varepsilon}_{ax}$ = - 3.1e-5 1/s until failure. Because of a lack of experiment data, all simulations have been performed only considering a deformation rate of $\dot{\varepsilon}_{ax}$ = - 3.1e-5 1/s. Hence salt concrete has been considered as a rate-independent material. In whole three different TC-tests have been simulated, which vary in

applied radial stresses. The *Tab. 5-3* summarizes briefly all actions within the simulations. Here it should be pointed out, that it is not necessary to simulate the first interval. The purpose of the first interval is to make clear how a homogeneous stress distribution can be created within the model. An alternative is the initial application of equal stress conditions in vertical as well as horizontal direction. Thus the simulation emanates from an isotropic stress state and reproduces exclusively the deviatoric stress phase. Both approaches yield the same results.

Tab. 5-3: Information about the applied time intervals (TC- test)

Experiment	Interval	Interv. Start [d]	Interv. End [d]	$\dot{\varepsilon}$ [1/s]	Interv. Start σ_{radial} [MPa]	Interv. End σ_{radial} [MPa]
T_1.38m	1	0	0.02	-	-0.1	-1
	2	0.02	Num. failure	-3.1e-5	-1	-1
P5	1	0	0.02	-	-0.1	-2
	2	0.02	Num. failure	-3.1e-5	-2	-2
P10	1	0	0.02	-	-0.1	-3
	2	0.02	Num. failure	-3.1 e-5	-3	-3

The simulation of all TC-tests incorporates two time intervals. In the first interval a stress equilibrium is developed. It lasts 0.02 day. After these 0.02 day, all displacements are set to zero. The second time interval represents the deviatoric phase, in which the vertical stress is increased by submitting a constant deformation rate. The simulation is stopped when failure is identified. It is not possible to reach convergence within the simulation then. The initial porosity of the salt concrete sample corresponds to the measured porosity ($\phi = 0.06$). Triangular elements have been selected for mesh generation. In whole the generated mesh consists of 210 elements and 132 nodes. The elements are equally distributed. To guarantee the correct application of the initial as well as boundary conditions, a consistency check has been performed, which has evaluated the horizontal stress distribution when the simulation stops as not reaching convergence. Finally the correct application was proved (see *Fig. Appendix B-1*).

5.1.2 PARAMETER SELECTION: LITERATURE RESEARCH AND EXPERIMENT EVALUATION

The values of young's modulus as well as poison ratio have been adopted from (Czaikowski et al. 2016) ($E = 10\,000$ MPa and $\nu = 0.18$) and the value of Φ from (Mánica et al. 2016b). The parameter ω, which controls the association of the flow rule, has been set to 1. The peak friction angle as well as the peak cohesion of salt concrete had to be evaluated from the recent laboratory results. Both values are essential input parameters of the employed model. They are utilized to estimate the mobilized friction angle and cohesion. For determining the peak friction angle φ_{peak} and peak cohesion c_{peak}, the failure strength ($\sigma_{axial\ max}$) and the corresponding radial stress ($\sigma_{radial\ corr}$) have been detected from every experiment (also considering the excluded experiments). Corresponding p- and J- values have been calculated from $\sigma_{axial\ max}$ and $\sigma_{radial\ corr}$ then. These calculated values have been plotted in a p-J-diagram together with a regression line.

The *Eq. 4-2* describes a linear equation. A reshaped form of the equation is represented by:

$$J = \frac{(\sin\varphi\ (c\cot\varphi + p))}{\left(\cos\theta + \frac{1}{\sqrt{3}}\sin\theta\sin\varphi\right)} \qquad \text{Eq. 5-1}$$

Due to conditions of triaxial loading, the value of θ is -30°. A range of p-values has been inserted in *Eq. 5-1* and the corresponding J- values have been calculated. These have been added to previously determined values in the p-J-diagram. By adapting φ and c, the evolving line has covered the regression line. When both lines have overlapped, the final φ- and c- values has been determined (compare *Fig. 5-3*). This method has revealed a peak friction angle φ_{peak} of 23.5° and a peak cohesion c_{peak} of 12.3 MPa.

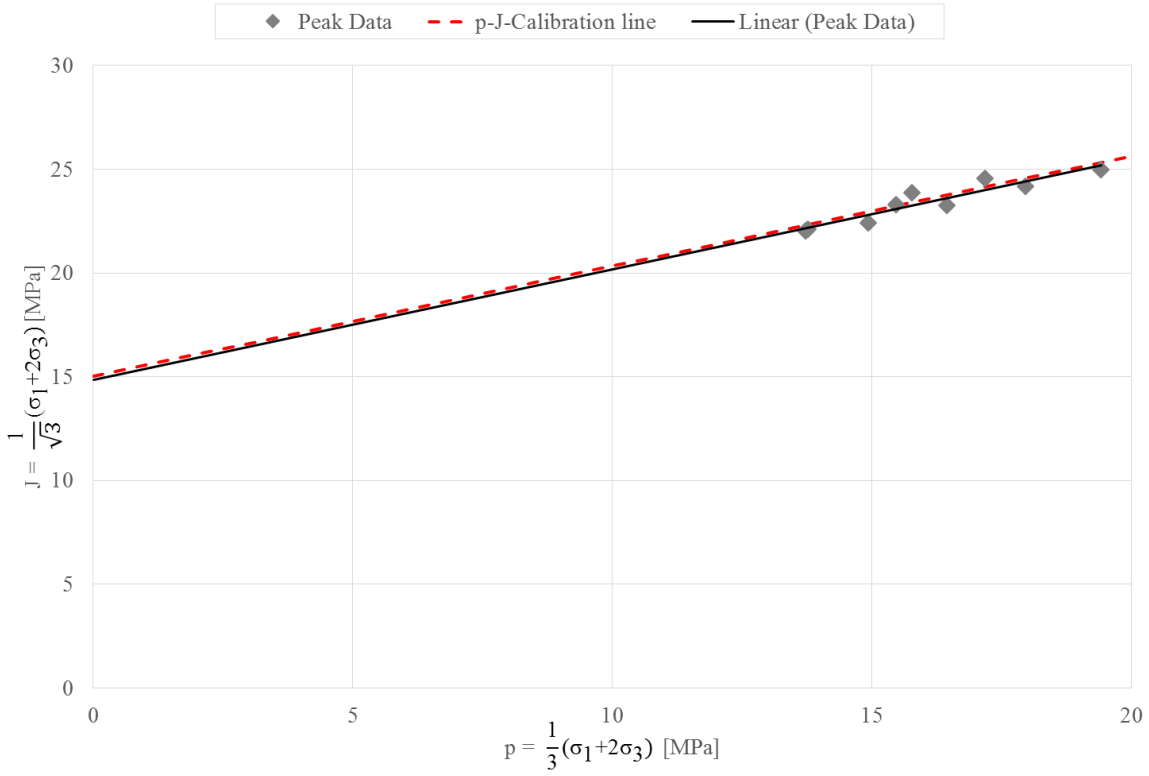

Fig. 5-3: Final derivation of φ_{peak} - and c_{peak}

Apart from the peak friction angle and the peak cohesion, the model demands input parameters regarding to initial friction angle φ_{ini} and the residual friction angle φ_{res}. Referring to *Fig. 4-5*, the initial friction angle controls the occurrence of the simulated yield point. The residual friction angel influences the residual strength. In order to determine the initial as well as the residual friction angle, the same analysis can be carried out. The only difference is that the yield point and the residual strength point respectively are considered instead of the failure strength $\sigma_{axial\ max}$. In case the different yield points and residual strength points are figured out correctly, the analysis yield the initial as well as the residual friction angle. Both values are smaller than the peak friction angle. Further input parameters are a_{soft} and a_{hard}. The shape of the stress- strain-curve is controlled by the parameter a_{hard} within the hardening branch and by a_{soft} within the softening branch. Values from (Mánica et al. 2016b) have been adopted as an indication for the

magnitude of a_{hard} and a_{soft}. Small magnitudes of 1e-3 are suggested to be suitable. In contrast to the hardening, the reproduction of the exhibited brittle behavior represents a demanding task, because the consideration of the rapid loss of strength is accompanied by great numerical issues. Therefore the recent thesis only adverts to the option to assume the brittle behavior, however no particular calibration of the softening branch was performed. Further some theories are mentioned dealing with the sufficient treatment of the brittle behavior within numerical simulations. The missing input parameters ξ_1, ξ_2 and ξ_3 are the different equivalent plastic strain values separating the different zones of behavior (compare *Fig. 4-5*). First the ξ_1- parameter controls the equivalent strain, at which the maximum strength is reached. Second the ξ_2 - parameter controls the equivalent strain, at which the softened strains start developing and finally the ξ_3 - parameter controls the equivalent strain, at which the residual strength is reached. In case of the salt concrete simulation, it can be assumed that the values of ξ_2 and ξ_3 only differ slightly from each other to obtain the indication of the sudden loss of strength.

5.1.3 PARAMETER SELECTION: CALIBRATION WORK

The results obtained from the performed calibration work is described in the following section. It mainly refers to the calibration work related to P5. The results of T_1.38m and P10 including the corresponding graphs are listed in the appendix though.

As it has already described in the last subchapter, six input parameter had been derived from literature and experiment evaluation. The remaining input parameters have been identified by a trial and error process. Ignoring strain hardening and softening the calibration process has started by inserting the six known input parameters into the constitutive model. A LEPP-stress-strain-curve has been obtained as a result (compare *Fig. 5-4*), which has yielded a maximum deviatoric stress around σ_{Dev} = 38 MPa. Additionally a transition of the volumetric strains is noticeable. Further steps of calibration work have focused on the input parameters φ_{ini}, a_{hard}, and ξ_1. In combination these parameters define the stress- strain curve within the hardening branch and control the appearance of peak strength. Compared to the failure point, the yield point is already reached by applying low deviatoric stresses, thus it is reasonable to assume smaller φ_{ini}-values than the obtained φ_{peak}-values.

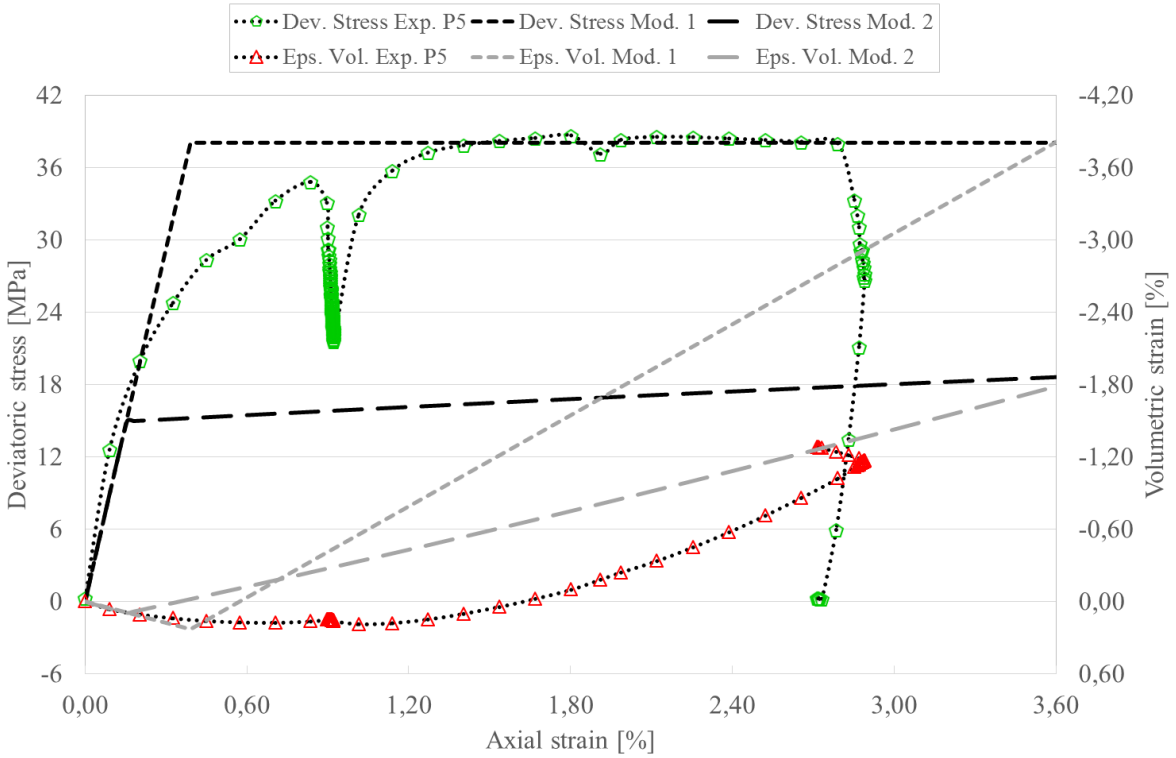

Fig. 5-4: Results of calibration of the initial friction angle

The parameters that have been used for the model shown in *Fig. 5-4* are listed in *Tab. 5-4*:

Tab. 5-4: Corresponding calibrated material parameters
(compare Mod. 1 and Mod. 2 in Fig. 5-4: Results of calibration of the initial friction angle)

	E [MPa]	ν [-]	Φ [°]	ω [-]	φ_{peak} [°]	c_{peak} [-]	φ_{ini} [°]	φ_{res} [°]
Mod. 1	10 000	0.18	25	1.0	23.50	12.30	23.50	1.0
Mod. 2	10 000	0.18	25	1.0	23.50	12.30	9.40	1.0

	a_{hard} [-]	a_{soft} [-]	ξ_1 [-]	ξ_2 [-]	ξ_3 [-]	σ_s [MPa]	γ [d^{-1}]	n [-]	m [-]
Mod. 1	1.0	1.0	1.0	1.0	1.0	1.0	1.0	1.0	1.0
Mod. 2	1.0	1.0	1.0	1.0	1.0	1.0	1.0	1.0	1.0

When the φ_{ini}- value is changed exclusively, a similar stress-strain-curve is obtained. The *Fig. 5-4* depicts the result of setting φ_{ini} to 9.4°. In this case the stress-strain-curve describes yielding when subjecting the samples to deviatoric stresses slightly bigger than 40 % of the actual maximum deviatoric stress. The maximum deviatoric stress of salt concrete is reached when axially deforming it around 2 %. Therefore the equivalent plastic strain ξ_1 has been considered to be around 0.02. By fixing a_{hard} to 0.005 and ξ_1 to 0.02, the strain development while plastic loading has been approximated well (compare *Fig. 5-5*).

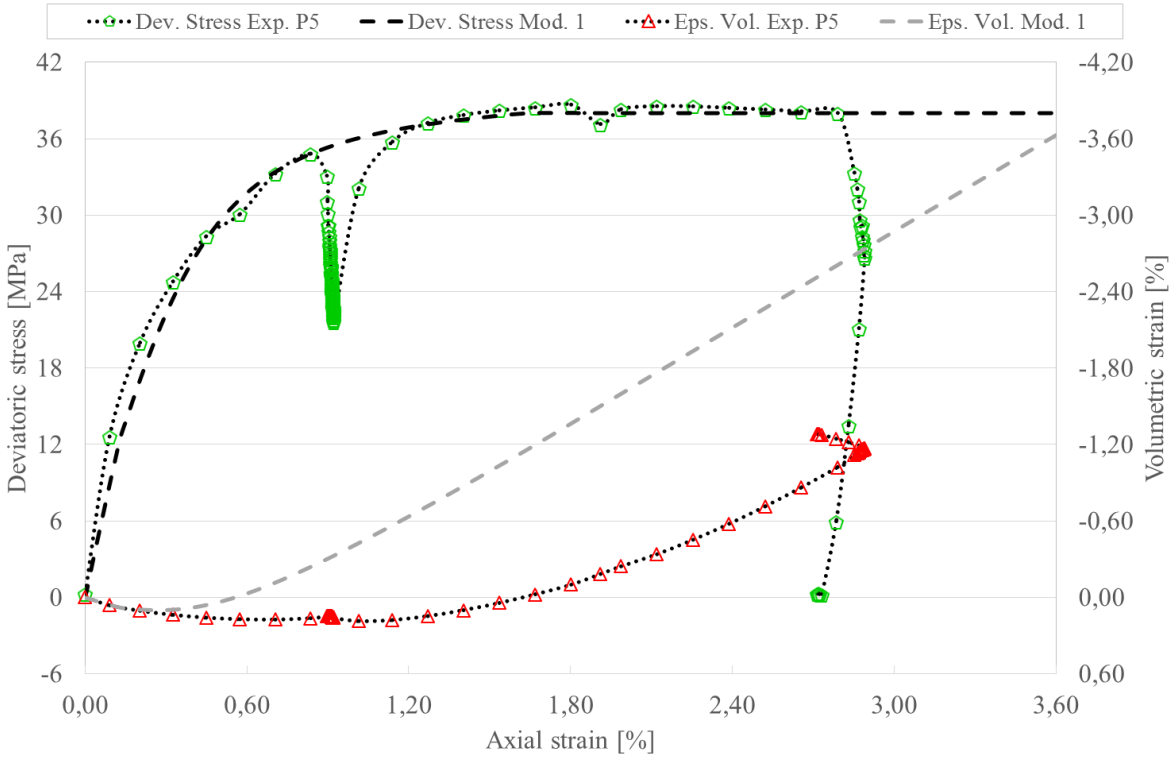

Fig. 5-5: Result of a_{hard}- and ξ_1-calibration

The parameters that have been used for the model shown in *Fig. 5-5* are listed in *Tab. 5-5*:

Tab. 5-5: Corresponding calibrated material parameters
(compare Mod. 1 in Fig. 5-5: Result of a_{hard}- and ξ_1-calibration)

	E [MPa]	ν [-]	Φ [°]	ω [-]	φ_{peak} [°]	c_{peak} [-]	φ_{ini} [°]	φ_{res} [°]
Mod. 1	10 000	0.18	25	1.0	23.50	12.30	9.40	1.0

	a_{hard} [-]	a_{soft} [-]	ξ_1 [-]	ξ_2 [-]	ξ_3 [-]	σ_s [MPa]	γ [d^{-1}]	n [-]	m [-]
Mod. 1	0.005	1.0	0.02	1.0	1.0	1.0	1.0	1.0	1.0

After calibrating the hardening branch, further steps have concentrated on softening. The following steps do not represent a calibration of the softening branch, but the employed constitutive model gives an indication of failure. A sufficient reproduction of the brittle behavior of salt concrete is a demanding task, because the exhibited sudden loss of strength coincides with the initial development of thin zones of intensive shearing within the sample (Jirásek 2002). This generation of shear bands or fractures in particular zones is known as “strain localization”. A constitutive model embedded in the framework of continuum mechanics cannot be utilized to objectively obtain these zones of localized plastic deformations (Jirásek 2002).

The obtained results depend strongly on the employed mesh. To counteract the known issues under the framework of continuum mechanics, different methods have been developed, called “regularization techniques”. They enable to retain the objectivity of the boundary value problem and to bypass the dependency regarding to the employed mesh. The brittle behavior of salt

concrete can be reproduced by taking a strain localization phenomenon into account and employing such regularization techniques (Jirásek 2002).

The value of the residual friction angle φ_{res} has been assumed to be about 10 % of φ_{peak}. Beside φ_{res} the equivalent plastic strains had to be defined, from which the softening branch begins. Therefore ξ_2 and ξ_3 have been equalized and adapted to the experiment results step wise. The *Fig. 5-6* shows that the utilization of a ξ_2- and ξ_3- value around 0.04 has yielded good approximations.

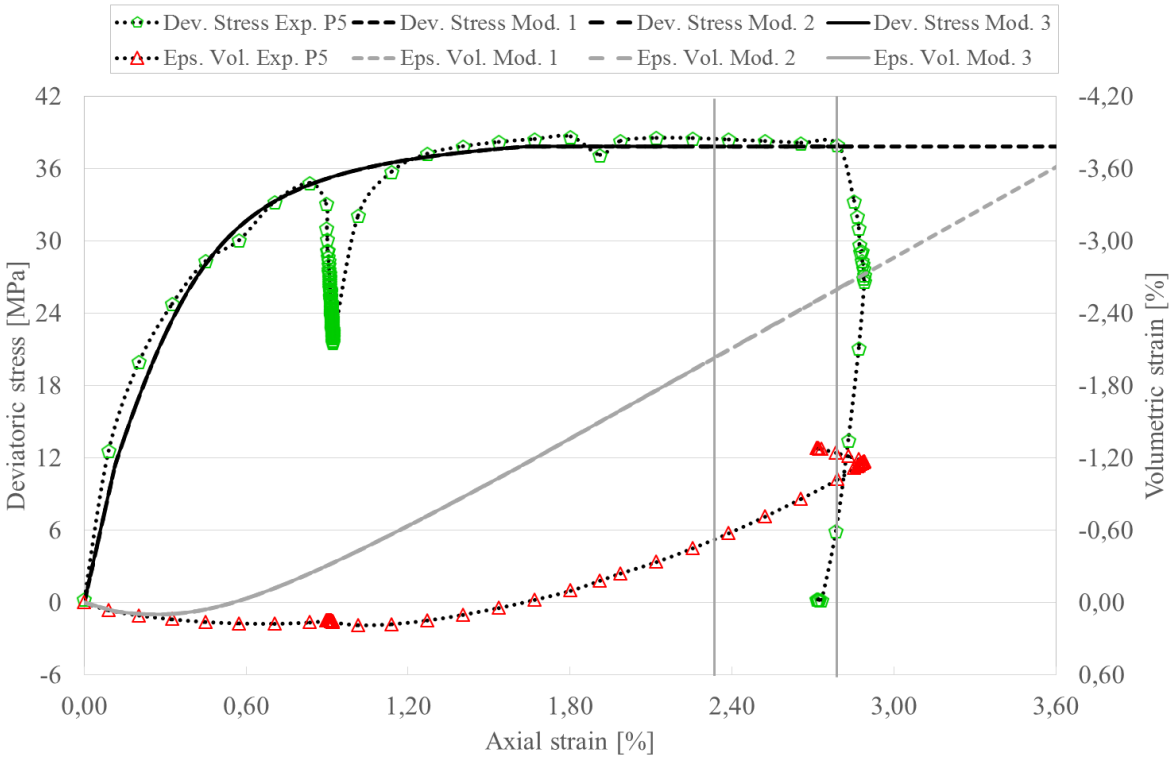

Fig. 5-6: Results of ξ_2 –calibration

The parameters that have been used for the model shown in *Fig. 5-6* are listed in *Tab. 5-6*:

Tab. 5-6: Corresponding calibrated material parameters
(compare Mod. 1, Mod. 2 and Mod. 3 in *Fig. 5-6*: Results of ξ_2 –calibration)

	E [MPa]	ν [-]	Φ [°]	ω [-]	φ_{peak} [°]	c_{peak} [-]	φ_{ini} [°]	φ_{res} [°]
Mod. 1	10 000	0.18	25	1.0	23.50	12.30	9.40	2.35
Mod. 2	10 000	0.18	25	1.0	23.50	12.30	9.40	2.35
Mod. 3	10 000	0.18	25	1.0	23.50	12.30	9.40	2.35

	a_{hard} [-]	a_{soft} [-]	ξ_1 [-]	ξ_2 [-]	ξ_3 [-]	σ_s [MPa]	γ [d^{-1}]	n [-]	m [-]
Mod. 1	0.005	1.0	0.02	0.08	0.08	1.0	1.0	1.0	1.0
Mod. 2	0.005	1.0	0.02	0.04	0.04	1.0	1.0	1.0	1.0
Mod. 3	0.005	1.0	0.02	0.03	0.03	1.0	1.0	1.0	1.0

In order to indicate the great loss of stiffness exhibited by the salt concrete samples, it has been assumed to make the difference between ξ_2 and ξ_3 relatively small. Thus ξ_3 has been set to 0.048. In accordance to the value used in (Mánica et al. 2016b), a_{soft} has preliminary been considered to be equal to 0.07. In combination with the small φ_{res}- value, it has been expected, that the model describes some points indicating a linear decrease of the applied stresses then. The *Fig. 5-7* depicts nicely the effect of a_{soft}. Most points have been yielded by setting a_{soft} to 0.04, which is slightly smaller in comparison to the value used in (Mánica et al. 2016b).

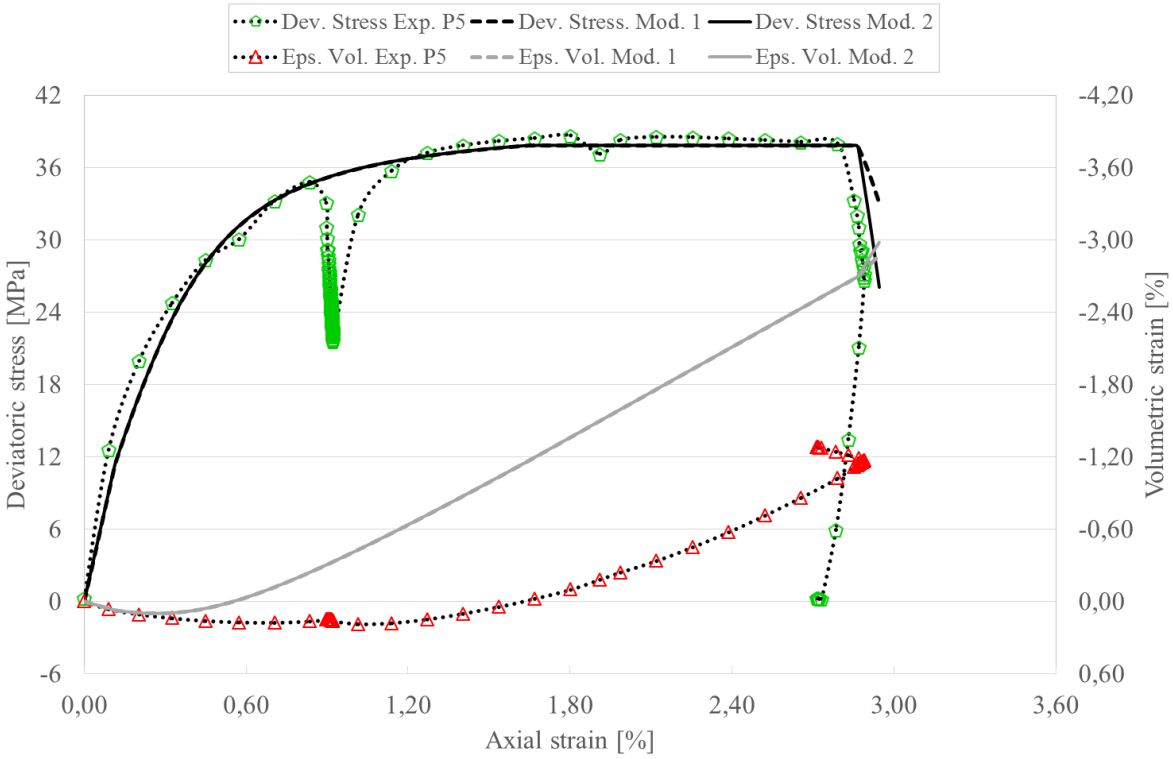

Fig. 5-7: Assumption of brittle behavior within the softening branch

The parameters that have been used for the model shown in *Fig. 5-7* are listed in *Tab. 5-7*:

Tab. 5-7: Corresponding calibrated material parameters
(compare Mod. 1 and Mod. 2 in Fig. 5-7: Assumption of brittle behavior within the softening branch)

	E [MPa]	ν [-]	Φ [°]	ω [-]	φ_{peak} [°]	c_{peak} [-]	φ_{ini} [°]	φ_{res} [°]
Mod. 1	10 000	0.18	25	1.0	23.50	12.30	9.40	2.35
Mod. 2	10 000	0.18	25	1.0	23.50	12.30	9.40	2.35

	a_{hard} [-]	a_{soft} [-]	ξ_1 [-]	ξ_2 [-]	ξ_3 [-]	σ_s [MPa]	γ [d^{-1}]	n [-]	m [-]
Mod. 1	0.005	0.07	0.02	0.04	0.048	1.0	1.0	1.0	1.0
Mod. 2	0.005	0.04	0.02	0.04	0.048	1.0	1.0	1.0	1.0

In following paragraphs the brittle behavior is not taken into account any longer, thus all further performed simulations have stopped when the equivalent plastic strains have reached the ξ_2-value of 0.04.

Because of the initial consideration of an associated flow rule, the model has overestimated the development of the volumetric strains. Hence the parameter ω has been decreased step by step. The *Fig. 5-8* describes the declination of calculated volumetric strains by reducing ω. Finally, a value of ω = 0.3 has been determined to access the occurring volumetric strains. In case of P5, the calculated volumetric strains and the experimental data indicates almost the same dilatancy point. The calculations have estimated the development of dilatant deformations slightly too early in case T_1.38m and P10. In general, it can be observed that the calculated volumetric strains tend to become too small at the end of the simulation.

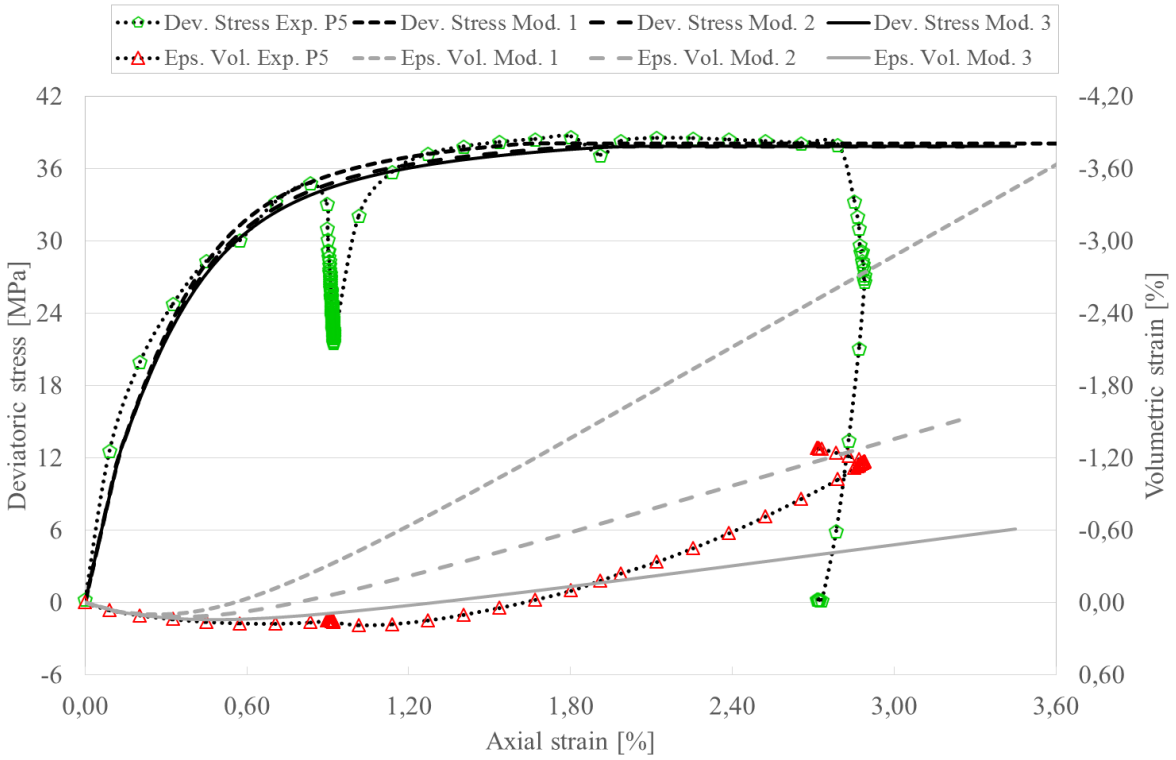

Fig. 5-8: Calibration of ω without considering softening

The parameters that have been used for the model shown in *Fig. 5-8* are listed in *Tab. 5-8*:

Tab. 5-8: Corresponding calibrated material parameters
(compare Mod. 1, Mod. 2 and Mod. 3 in *Fig. 5-8*: Calibration of ω without considering softening)

	E [MPa]	ν [-]	Φ [°]	ω [-]	φ_{peak} [°]	c_{peak} [-]	φ_{ini} [°]	φ_{res} [°]
Mod. 1	10 000	0.18	25	1.0	23.50	12.30	9.40	2.35
Mod. 2	10 000	0.18	25	0.6	23.50	12.30	9.40	2.35
Mod. 3	10 000	0.18	25	0.3	23.50	12.30	9.40	2.35

	a_{hard} [-]	a_{soft} [-]	ξ_1 [-]	ξ_2 [-]	ξ_3 [-]	σ_s [MPa]	γ [d^{-1}]	n [-]	m [-]
Mod. 1	0.005	1.0	0.02	0.04	0.04	1.0	1.0	1.0	1.0
Mod. 2	0.005	1.0	0.02	0.04	0.04	1.0	1.0	1.0	1.0
Mod. 3	0.005	1.0	0.02	0.04	0.04	1.0	1.0	1.0	1.0

5.1.4 OBTAINED RESULTS

The *Tab. 5-9* shows the finally identified set of material parameters, which is applicable in combination with the visco-plasticity model to simulate the short-term deformation behavior of salt concrete sufficiently (compare *Fig. 5-9*). The final parameter set results a good approximation of axial plastic strains within the hardening branch in all performed simulations. All simulations show both good estimations of the peak strength and of the volumetric strains by employing a non-associated flow rule (see *Fig. Appendix B-3* and *Fig. Appendix B-4*). In case of P10 the dilatancy point has been determined too early though.

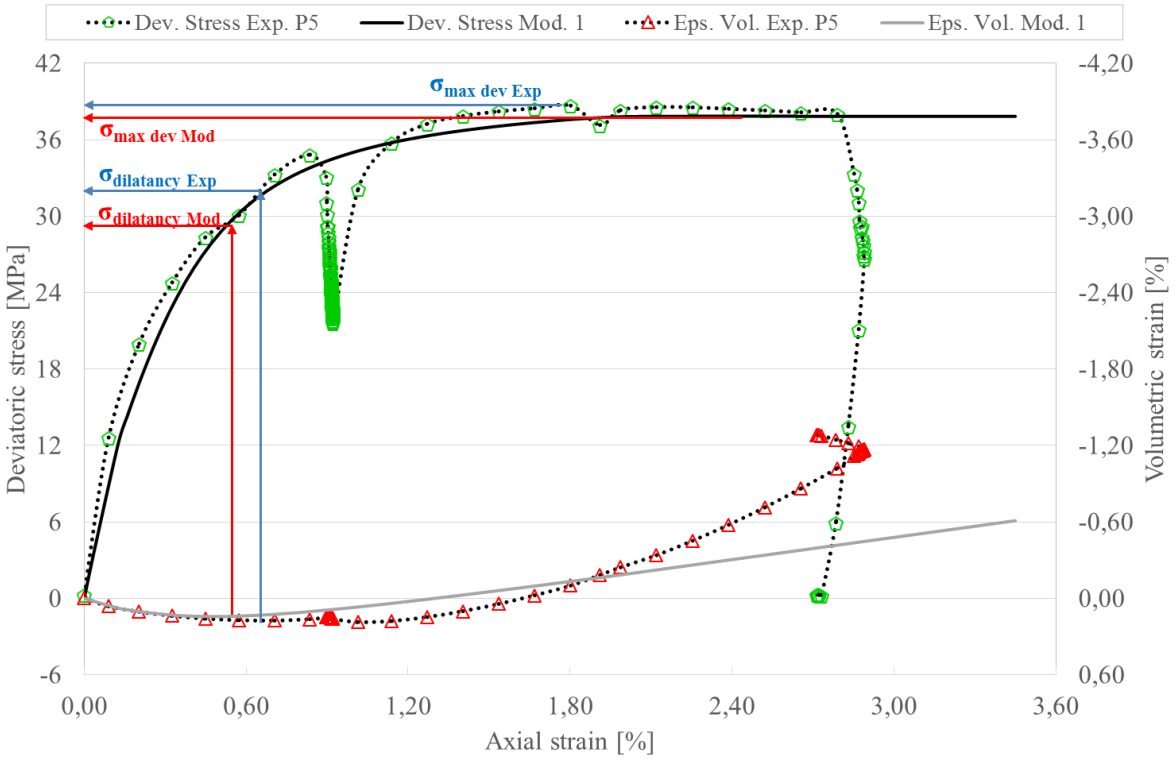

Fig. 5-9: Finally obtained results of the reproduction of the short-term behavior

The parameters that have been used for the model shown in *Fig. 5-9* are listed in *Tab. 5-9*:

Tab. 5-9: Finally obtained set of material parameters to reproduce the short-term deformation behavior (compare Mod. 1 in *Fig. 5-9*: Finally obtained results of the reproduction of the short-term behavior)

	E [MPa]	ν [-]	Φ [°]	ω [-]	φ_{peak} [°]	c_{peak} [-]	φ_{ini} [°]	φ_{res} [°]
Mod. 1	10 000	0.18	25	0.3	23.50	12.30	9.40	2.35

	a_{hard} [-]	a_{soft} [-]	ξ_1 [-]	ξ_2 [-]	ξ_3 [-]	σ_s [MPa]	γ [d^{-1}]	n [-]	m [-]
Mod. 1	0.005	1.0	0.02	0.04	0.04	1.0	1.0	1.0	1.0

5.2 LONG-TERM RESPONSE: UNIAXIAL COMPRESSION CREEP TEST (UCC)

Previously performed numerical simulations of salt concrete generated mainly insufficient results regarding to time-dependent deformations. Although some limitations have been detected, (Middelhoff and Czaikowski) showed that a modified form of Lemaitre's creep law is able to reproduce the time-dependent deformations of damaged salt concrete samples satisfactorily. This has been discussed in chapter 1. The recent numerical simulations have focused on the description of axial strains exhibited by intact salt concrete samples in the UCc-test. The employed samples have exhibited similar axial deformations. Therefore all five samples have been taken into considerations.

5.2.1 MAIN FEATURES OF THE NUMERICAL MODEL

The model is L = 0.16 m long and D = 0.08 m in diameter. All non-essential boundary conditions, like the steel piston, are omitted. Comparable to the TC- test, the UCc- test can be simulated assuming axial symmetry (compare *Fig. 5-10*).

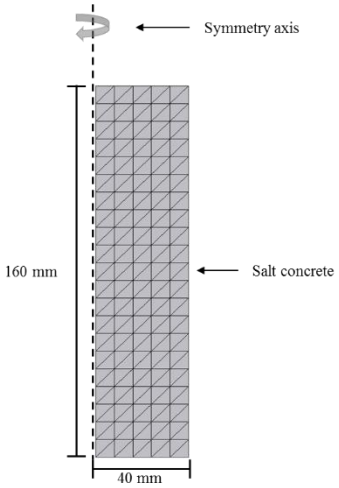

Fig. 5-10: Applied geometry including symmetry axis and model dimension

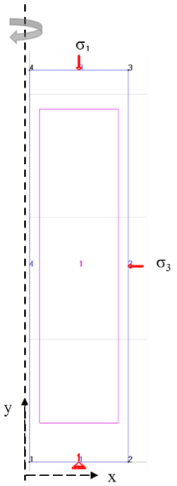

Fig. 5-11: Applied boundary conditions

Horizontal displacements are allowed at the bottom part of the sample, so a homogeneous stress distribution is created. The horizontal stresses remain constant during the experiment progress and is fixed to - 0.1 MPa. The initial porosity of the salt concrete is set to $\phi = 0.06$ and the horizontal as well as the vertical initial stresses are considered to be $\sigma_{ini} = -0.1$ MPa. Triangular elements are chosen. The mesh consists of 100 Elements and 66 nodes.

The simulation is performed in six intervals. Three intervals include a ramp loading process, in which the axial stress σ_1 affecting the top part of the sample is increased. During the other intervals the deviatoric stress is kept constant. In contrast to the experiment, the intervals including the ramp loading processes cover the same time span, so every ramp loading lasts 0.1 days. The *Tab. 5-10* describes the stepwise increase of deviatoric stress from 5 MPa to 20 MPa.

Tab. 5-10: Applied intervals (UCc)

Interval	Interv. Start	Interv. End	Interv. Start		Interv. End	
			σ_{axial}	σ_{radial}	σ_{axial}	σ_{radial}
	[d]	[d]	[MPa]	[MPa]	[MPa]	[MPa]
1	0.00	0.10	-0.1	-0.1	-5.0	-0.1
2	0.10	107.00	-5.0	-0.1	-5.0	-0.1
3	107.00	107.10	-5.0	-0.1	-10.0	-0.1
4	107.10	179.00	-10.0	-0.1	-10.0	-0.1
5	179.00	179.10	-10.0	-0.1	-20.0	-0.1
6	179.10	341.00	-20.0	-0.1	-20.0	-0.1

In order to guarantee the correct application of the initial and boundary conditions, a consistency check has been performed, which has evaluated the vertical and horizontal stress distribution after the second, fourth and sixth time interval. Finally, the correct application was determined (see *Fig. Appendix B-5* and *Fig. Appendix B-6*)

5.2.2 PARAMETER SELECTION: LITERATURE RESEARCH AND EXPERIMENT EVALUATION

A utilization of the parameter set identified by (Middelhoff and Czaikowski) seems to simplify the parameter selection process. However the applicability must not be taken for granted, because the set of material parameter has been calibrated to previously damaged material. The main differences between the previously evaluated TCc- test (compare (Middelhoff and Czaikowski)) and the recent UCc-test had to be assessed before starting simulating.

Tab. 5-11: Determined parameter set for simulating damaged salt concrete according to (Middelhoff and Czaikowski)

	σ_s [MPa]	γ [d^{-1}]	n [-]	m [-]
Mod. TCc damaged Mat.	20	0.001	0	300

The *Fig. 5-12* below shows a comparison of the results obtained from the UCc-test and from the TCc-test. It refers to the phases of the experiment, in which the material shows viscoplastic deformation behavior. In order to simplify the comparison of viscoplastic strain development, all axial strains have been fitted to a value of $\varepsilon = 0.0$ %. The intact material reacts different to loading.

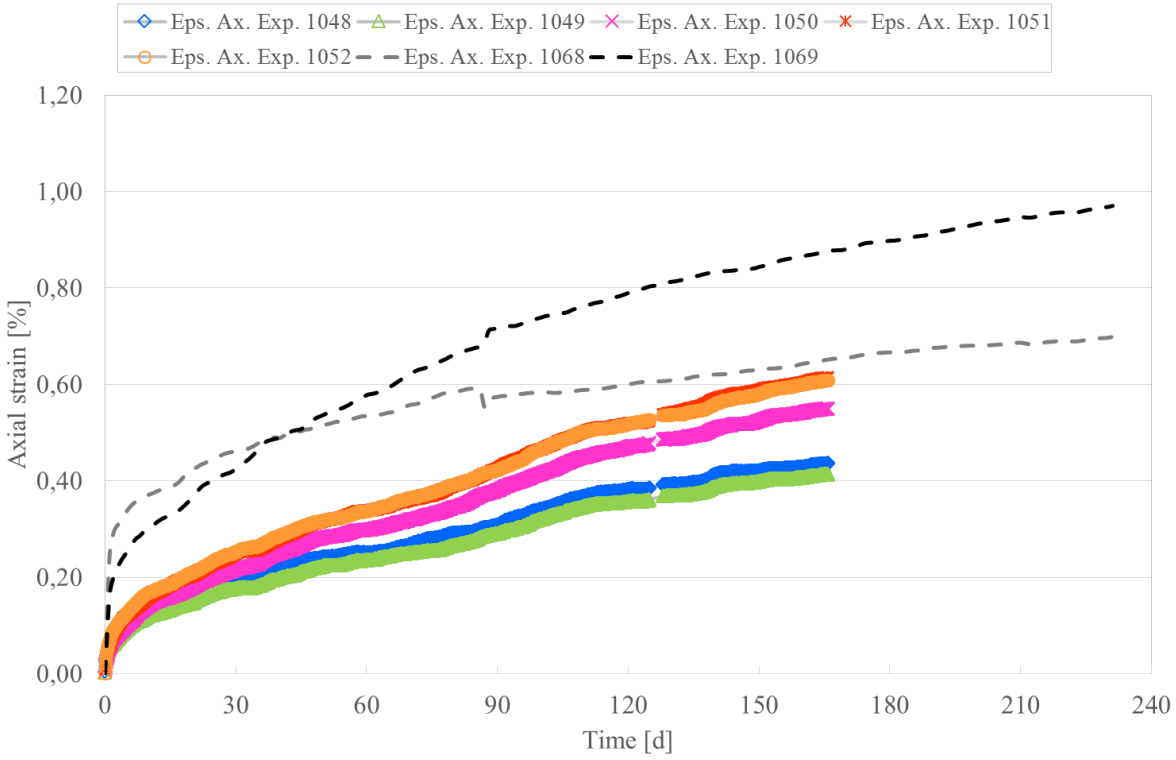

Fig. 5-12: Comparison of viscoplastic strains obtained from UCc-tests
(intact material: 1048, 1049, 1050, 1051, 1052) and TCc-tests (damaged material: 1068, 1069)

5.2.3 PARAMETER SELECTION: CALIBRATION WORK

Due to issues occurring in the simulation of the TCc- test, the threshold parameter σ_s had to be adapted. The parameter σ_s controls the activation of viscoplastic deformations, thus viscoplastic strains develop exclusively when the applied deviatoric stress state q is greater than σ_s. Accordingly viscoplastic deformations develop as recently as the samples are subjected to a deviatoric stress greater than 20 MPa. For instance, a deviatoric stress state q of 16 MPa generates viscoplastic strains.

Resulting from a lack of tests under deviatoric stress levels, it has been avoided to calibrate the parameter of n. The parameter controls the increase of creep deformations with increasing deviatoric stresses.

The magnitude of initial viscoplastic strains was adapted because the TCc- samples exhibit higher initial strains (ε_{ini} = 0.2 - 0.3 %) in comparison to the UCc- samples (ε_{ini} = 0.1 %) (see *Fig. 5-12*). In order to decrease their magnitude, the parameter γ has been decreased stepwise during calibration work, as it can be seen in *Fig. 5-13*. The calibration started by inserting the known γ-parameter (γ = 0.001), which has yielded too big initial viscoplastic strains. A value of γ = 0.0005 resulted in better values, however these values were still too high. Finally, a value of γ = 0.0002 reproduced the initial viscoplastic strains satisfactorily.

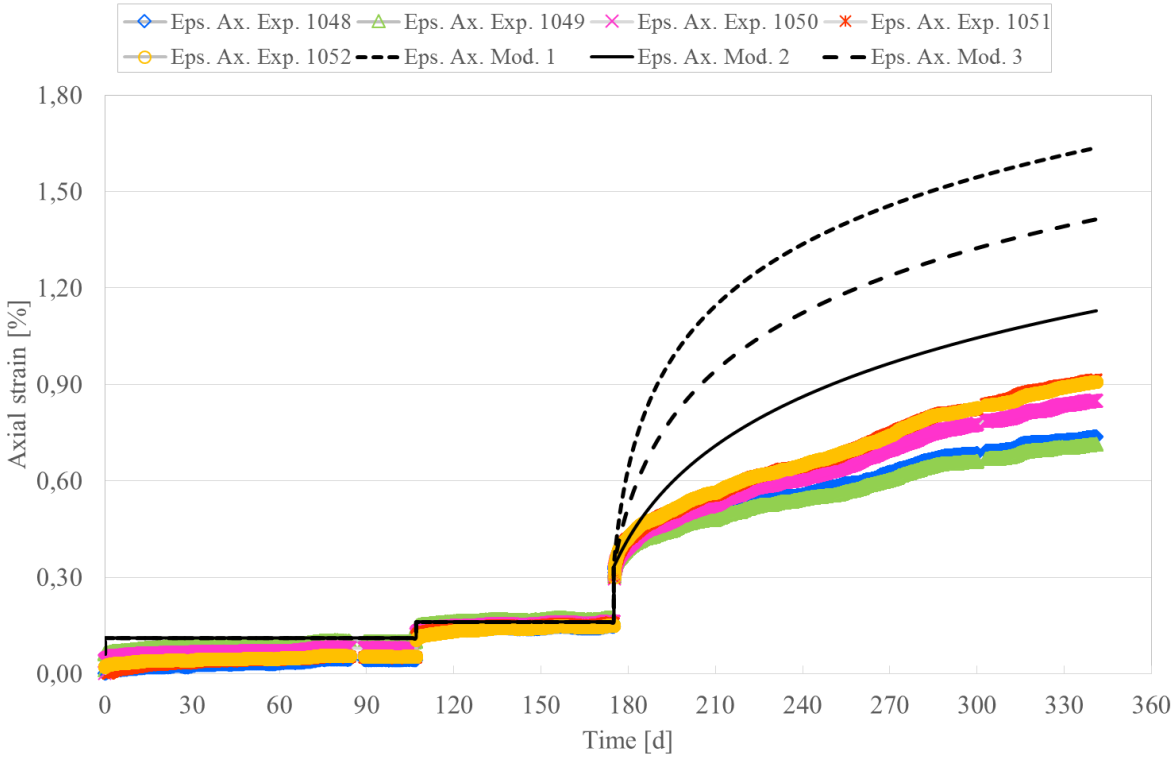

Fig. 5-13: Calibration of the viscosity γ
(Simulation results and experiment data are fitted at an axial strain of 0.16 % (179 d))

The parameters that have been used for the model shown in *Fig. 5-13* are listed in *Tab. 5-12*:

Tab. 5-12: Corresponding calibrated material parameters
(compare Mod. 1, Mod. 2 and Mod. 3 in *Fig. 5-13*)

	E [MPa]	ν [-]	Φ [°]	ω [-]	φ_{peak} [°]	c_{peak} [-]	φ_{ini} [°]	φ_{res} [°]
Mod. 1	10 000	0.18	25	0.3	23.50	12.30	9.40	2.35
Mod. 2	10 000	0.18	25	0.3	23.50	12.30	9.40	2.35
Mod. 3	10 000	0.18	25	0.3	23.50	12.30	9.40	2.35

	a_{hard} [-]	a_{soft} [-]	ξ_1 [-]	ξ_2 [-]	ξ_3 [-]	σ_s [MPa]	γ [d^{-1}]	n [-]	m [-]
Mod. 1	0.005	1.0	0.02	0.04	0.04	16	0.001	0	300
Mod. 2	0.005	1.0	0.02	0.04	0.04	16	0.0002	0	300
Mod. 3	0.005	1.0	0.02	0.04	0.04	16	0.0005	0	300

The *Fig. 5-14* reveals that the results of UCc-tests and TCc-tests greatly vary in the maximum magnitude of viscoplastic strains. The maximal axial strains in the UCc- test are around ε_{max} = 0.6 %, whereas the strains in the TCc-test reach a value of ε_{max} = 1.0 %. Therefore, an increase of the parameter m is necessary to reduce the accumulated plastic strains. As depicted in *Fig. 5-14* a value of m = 700 yields a good approximation.

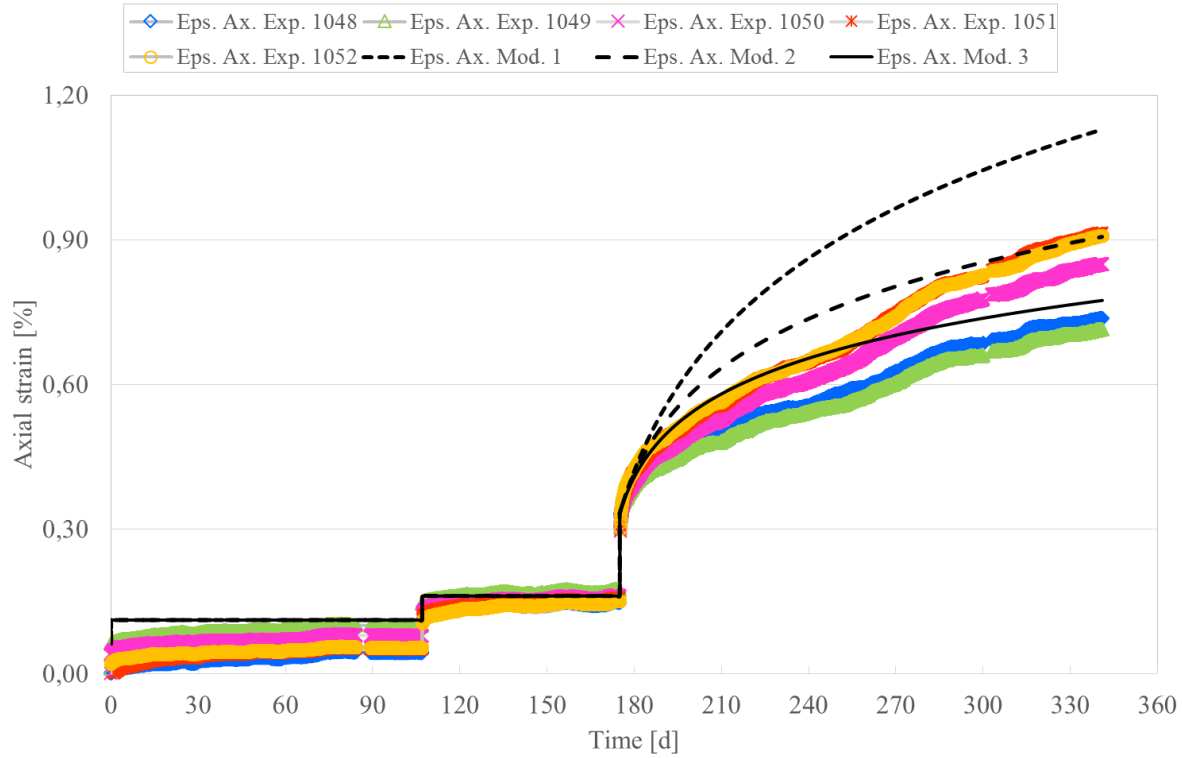

Fig. 5-14: Calibration of m
(Simulation results and experiment data are fitted at an axial strain of 0.16 % (179 d))

The parameters that have been used for the model shown in *Fig. 5-14* are listed in *Tab. 5-13*:

Tab. 5-13: Corresponding calibrated material parameters
(compare Mod. 1, Mod. 2 and Mod. 3 in *Fig. 5-14*)

	E [MPa]	ν [-]	Φ [°]	ω [-]	φ_{peak} [°]	c_{peak} [-]	φ_{ini} [°]	φ_{res} [°]
Mod. 1	10 000	0.18	25	0.3	23.50	12.30	9.40	2.35
Mod. 2	10 000	0.18	25	0.3	23.50	12.30	9.40	2.35
Mod. 3	10 000	0.18	25	0.3	23.50	12.30	9.40	2.35

	a_{hard} [-]	a_{soft} [-]	ξ_1 [-]	ξ_2 [-]	ξ_3 [-]	σ_s [MPa]	γ [d^{-1}]	n [-]	m [-]
Mod. 1	0.005	1.0	0.02	0.04	0.04	16	0.0002	0	300
Mod. 2	0.005	1.0	0.02	0.04	0.04	16	0.0002	0	500
Mod. 3	0.005	1.0	0.02	0.04	0.04	16	0.0002	0	700

5.2.4 OBTAINED RESULTS

Besides the possibility of simulating the short-term deformations, the visco-plasticity-model has been chosen because it enables the reproduction of long-term deformations related to creep. The investigations of (Middelhoff and Czaikowski) have proved that the implemented form of Lemaitre's creep law describes sufficiently creep deformations of salt concrete in case of low deviatoric stresses. In order to distinct between elastic strain and viscoplastic strain development, the recent model includes a threshold parameter σ_s. As already determined within chapter 3, salt concrete starts exhibiting creep deformations as recently as subjecting it to deviatoric

stresses greater than 20 MPa. This yields an σ_s - value of 16 MPa. The black curve in *Fig. 5-15* describes the finally obtained results after calibration.

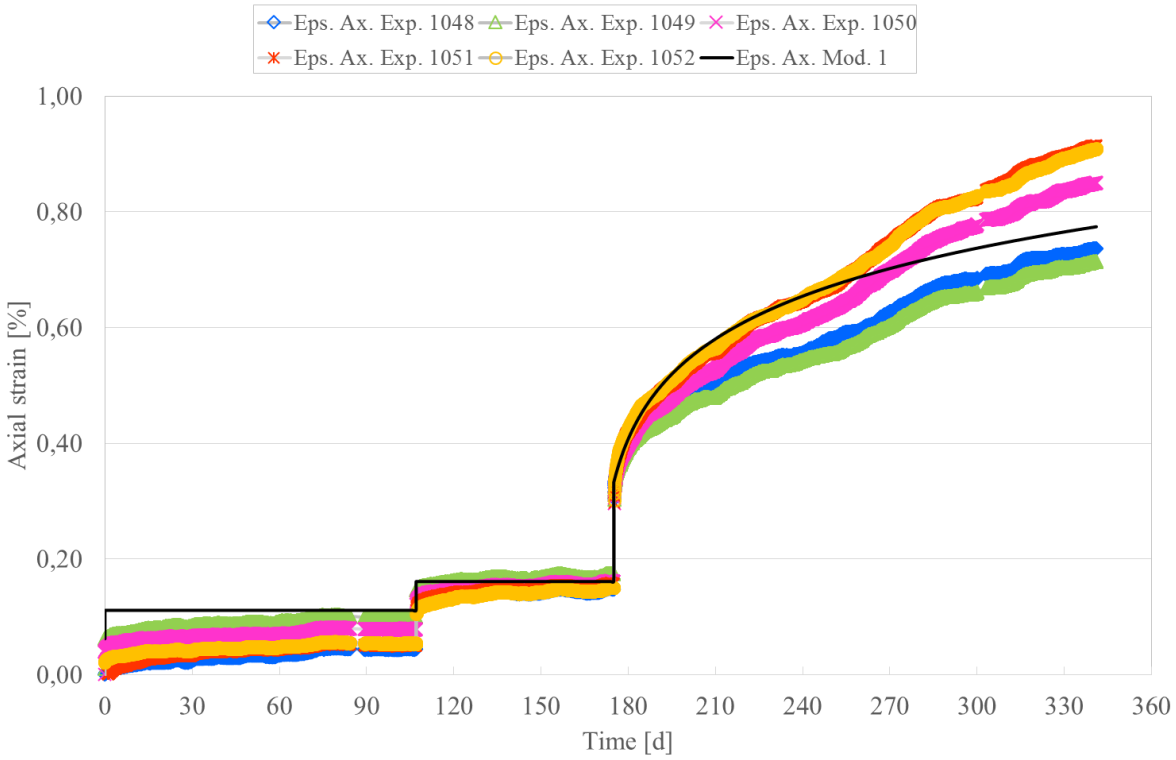

Fig. 5-15: Final results of UCc- simulation
(Simulation results and experiment data are fitted at an axial strain of 0.16 % (179 d))

The parameters that have been used for the model shown in *Fig. 5-15* are listed in *Tab. 5-14*:

Tab. 5-14: Finally obtained set of material parameters to reproduce the long-term deformation behavior (compare Mod. 1 in *Fig. 5-15*)

	E [MPa]	ν [-]	Φ [°]	ω [-]	φ_{peak} [°]	c_{peak} [-]	φ_{ini} [°]	φ_{res} [°]
Mod. 1	10 000	0.18	25	0.3	23.50	12.30	9.40	2.35

	a_{hard} [-]	a_{soft} [-]	ξ_1 [-]	ξ_2 [-]	ξ_3 [-]	σ_s [MPa]	γ [d^{-1}]	n [-]	m [-]
Mod. 1	0.005	1.0	0.02	0.04	0.04	16	0.0002	0	700

The viscoplastic deformations seem to be reproduced sufficiently, whereas the elastic response of the material is slightly underestimated (approximately about 0.05 %), probably caused by the high stiffness of salt concrete. In order to better compare the simulated development of viscoplastic strains with experimental data, all curves have been fitted to an axial strain of 0.16 %. The previously mentioned proposals to decrease the γ- parameter and to increase the m- parameter result a good approximation in general. The initial deformations fit well, however the axial strains are first overestimated and finally underestimated during the further progress (compare *Fig. 5-15*).

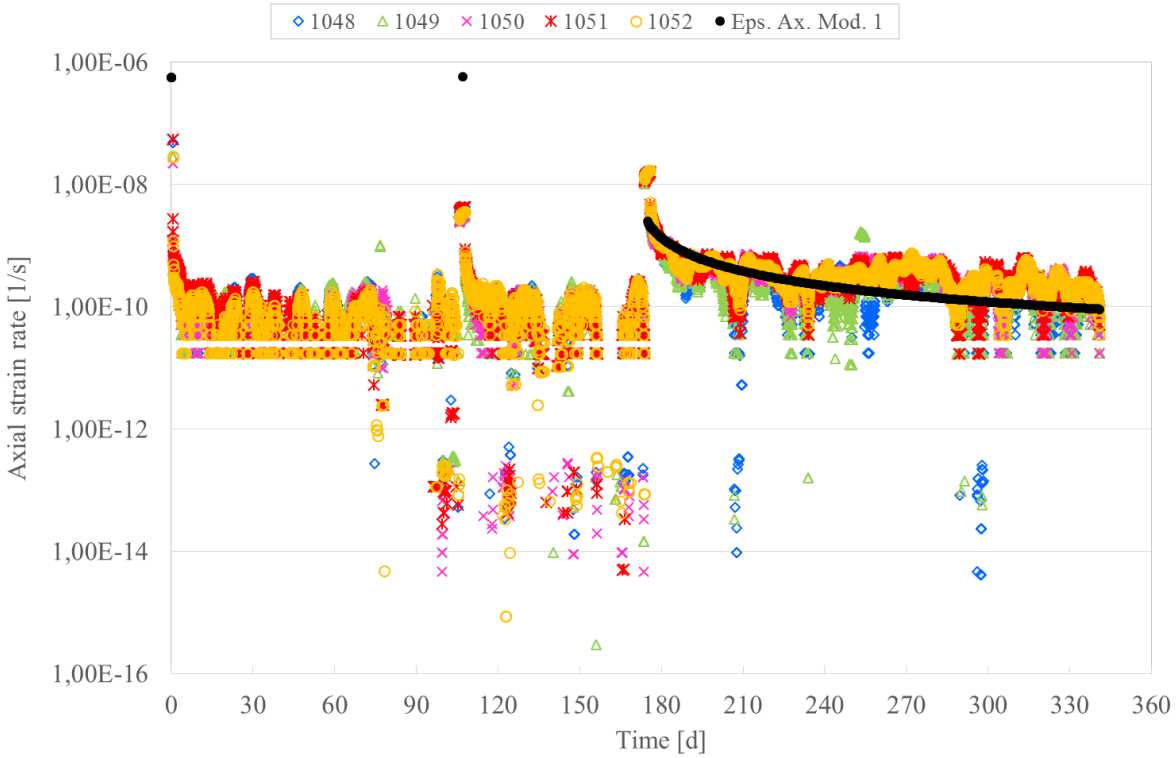

Fig. 5-16: Final results of UCc- simulation
(Time vs Axial strain rate/ Simulation results and experiment data are fitted at an axial strain of 0.16 % (179 d))

The *Fig. 5-16* also shows a good prediction of the strain rates during the last deviatoric stress phase. Even a sufficient cover of probably occurring transient creep deformations in the beginning of the third deviatoric phase is noticeable. Nevertheless no strain rates can be determined within the first and second deviatoric stress phase, because a pure elastic material behavior is considered. Chapter 3 adverts to a likely development of stationary creep deformations when the samples have been submitted to deviatoric stresses over 20 MPa for 166 days.

6 DISCUSSION AND CONCLUDING REMARKS

A recently developed visco-plasticity constitutive model basing upon the framework of elasto-plasticity has been employed to reproduce the short- as well as long-term mechanical behavior of salt concrete. Embedded in a suitable theoretical formulations, the constitutive model enables the reproduction of the main deformation features exhibited by salt concrete, like observed strain hardening before reaching the peak strength, peak strength, development of volumetric strains and creep deformations.

In whole the calibration work has involved the simulation of three triaxial compression tests (TC-test) varying in applied confining stresses first and second one uniaxial compression creep test (UCc-test). The calibration work has revealed that the visco-plasticity-model is able to reproduce the short- as well as the long-term mechanical behavior satisfactorily. As it was initially envisaged the mechanical behavior is described by exclusively employing one set of material parameters. The *Tab. 6-1* lists the finally obtained set of material parameters. Nevertheless some drawbacks inside the visco-plasticity model have been identified. They are commented and discussed in following.

Tab. 6-1: Finally obtained set of material parameters to reproduce the entire deformation behavior of salt concrete

	E [MPa]	ν [-]	Φ [°]	ω [-]	φ_{peak} [°]	c_{peak} [-]	φ_{ini} [°]	φ_{res} [°]
Mod. 1	10 000	0.18	25	0.3	23.50	12.30	9.40	2.35

	a_{hard} [-]	a_{soft} [-]	ξ_1 [-]	ξ_2 [-]	ξ_3 [-]	σ_s [MPa]	γ [d^{-1}]	n [-]	m [-]
Mod. 1	0.005	1.0	0.02	0.04	0.04	16	0.0002	0	700

6.1 DISCUSSION: SHORT-TERM MECHANICAL BEHAVIOR

With respect to the simulation of the TC-tests, the constitutive model in combination with the finally generated set of material parameters has sufficiently estimated the axial strain development of all considered experiments. Not taking the observed brittle behavior into account, the developed axial strains have slightly been overestimated in case of T_1.38m and P5, so the failure occurs when axially deforming the sample by $\varepsilon = 3.5$ %. In case of P10 the simulation has yielded more precise results.

As already explained in detail, the reproduction of the observed brittle behavior represents a demanding task, because strain localization processes can be assumed to initialize the sudden loss of strength at the end of the experiments. The presented results only imply an option of an adequate treatment of this brittle behavior without considering the mentioned regularization techniques. Nevertheless strain localization processes should be borne in mind for further simulations of salt concrete.

Apart from the axial strain evolution, material parameters have also been calibrated to reproduce volumetric strains. The evaluation of volumetric strains enables to estimate the initialization of micro-fissure development in the sample, which probably causes an increase of porosity

and permeability. The *Fig. 5-8* illustrates clearly that an associated flow rule has yielded an overestimation of the volumetric strains in all cases. When employing a non-associated flow the dilatancy point has sufficiently been predicted in cases of P5 and T_1.38m, although the further development of volumetric strains has been underestimated. The volumetric strain development of P10 has always been overestimated (see *Fig. Appendix B-4*).

Another significant point represents the assumed strain rate independency of salt concrete. Strain rate dependency means, that the maximum compressive strength of a material depends on the applied deformation rate. Although (Mehta und Monteiro 2006) and (Pajak 2011) mention a rate-dependence of concrete on the one side and (Düsterloh 2010) a rate-dependence of salt on the other side, a strain rate independency had to be assumed as all considered TC-tests were exclusively carried out by applying one deformation rate. Hence the calibrated set of material parameters inside the visco-plasticity model only obtains well-fitting results in case of a deformation rate of $\dot{\varepsilon}_{ax}$= - 3.1e-5 1/s. Simulations of other experiments will yield non-satisfying results, if a different deformation rate is considered. Rate-dependency represents a phenomenon, whose causes have not fully been determined up-to-date. In case of salt concrete the viscosity of the material can be assumed as one major trigger of the rate-dependent behavior //.

Experiment results published in (DBE 2004) point clearly out the rate-dependence of salt concrete, which *Fig. 6-1* depicts below. It shows different J-values calculated from the maximal exhibited compressive strength and the corresponding confining stress. Within the performed TC-tests, the material has isotropically been loaded at the beginning. In a further step it has gradually been deformed until reaching the maximum compressive strength of the sample

Comparing to the "ASSE"-material, the material presented in (DBE 2004) was exclusively made to perform TC-tests under laboratory conditions. The biggest difference from the ASSE-type is the addition of hard coal fly ash. Thus the M2-type becomes more homogeneous. The material was partly saturated furthermore, so the degree of saturation and pore pressure effects respectively were not negligible. Last the produced salt concrete has not been subjected to convergence processes for 30 years. Nevertheless both kinds of salt concrete are comparable as their main components are crushed salt and cement (see *Tab. 6-2*):

Tab. 6-2: Composition of salt concrete type M2 related to 1 m³ (DBE 2004a)

Composition of salt concrete	Proportion [kg/ m³]	Proportion [mass-%]
Cement	328	16.4
Hard coal fly ash	328	16.4
Crushed salt	1072	53.8
Water	267	13.4
Total	2074	100

A rate-dependency is detectable in *Fig. 6-1*. It shows the experiment results revealed by (DBE 2004) in comparison with the recently obtained results.

For instance, nine samples have been subjected to three different deformation rates under a confining pressure of σ_3 = 2.5 MPa. By deforming the samples with a rate of $\dot{\varepsilon}$ = 2.5e-5 1/s, the

salt concrete is able to resist higher deviatoric stresses, whereas the values of maximum compressive strength decline gradually, when the applied deformation rate becomes smaller. A rate reduction below $\dot{\varepsilon}$ = 1.0e-6 1/s does not result in a further reduction of the compressive strength. This is noticeable by the overlaying values of $\dot{\varepsilon}$ = 1.0e-6 1/s and $\dot{\varepsilon}$ = 1.0e-7 1/s. Thus it can be assumed that the rate-independent stress envelope is located in this range.

The recently obtained results are in accordance with the values of (DBE 2004). The Asse-material describes a higher ultimate compressive strength due to the applied strain rate of $\dot{\varepsilon}$ = 3.1e-5 1/s. Hence the *Fig. 6-1* rather indicates a rate-dependence of salt concrete than it proves the dependence. In order to prove the rate-dependence it is recommendable to carry out further TC-tests including a variation of the deformation rates. However further tests are hardly not realizable due to the small amount of available salt concrete samples.

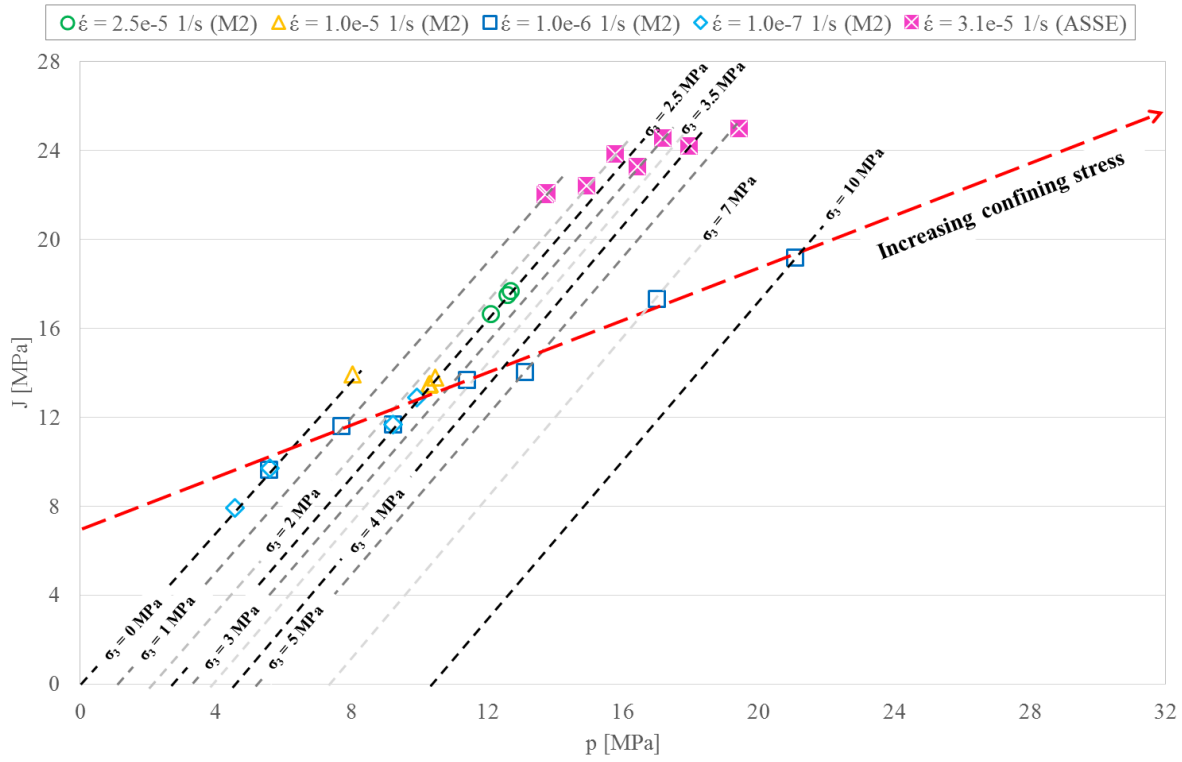

Fig. 6-1: Results of TC-tests carried out on salt concrete type M2/ Exhibition of rate dependency (compare (DBE 2004))

6.2 DISCUSSION: LONG-TERM MECHANICAL BEHAVIOR

Since the set of material parameters derived in (Middelhoff und Czaikowski) was calibrated to pre-damaged salt concrete samples, another set for non-damaged material had to be developed. The previous damage has made it impossible to compare the results of the TCc-test with the ones of the UCc-test.

The results gained in chapter 5.2.4 correspond to the results of (Middelhoff und Czaikowski). In general the recently developed set of material parameters is partly able to reproduce the long-term mechanical behavior of salt concrete. One frequently discussed point is the employment of the threshold parameter σ_s. Its utilization enables the clear distinction between elastic and

viscoplastic strain development that depends on deviatoric stress level. However results from creep experiments examining rock salt militate against the utilization of such threshold parameter in case of salt concrete. They refer to the fact that rock salt deforms in time viscoplastically, even by subjecting it to low deviatoric stresses (Wieczorek 2010). For instance (Czaikowski et al. 2016) considers a modeling approach of permanently developing viscoplastic strains. By means of σ_s, small viscoplastic deformations are disregarded and elastic deformations are supposed only. In case of the recent creep tests, the axial strains created within the first and second deviatoric stress phases have been underestimated. The underestimation has probably been caused by the high value of the young's modulus of the salt concrete. Hence the strains in these both phases have not been approximated satisfactorily (compare *Fig. 5-15*)

Concerning the viscoplastic deformations the modified form of Lemaitre's creep law estimates sufficiently the magnitude of transient creep deformations on the one side. However the creep law exhibits non-negligible limitations on the other side. The simulation has overestimated the deformations of samples 1048 and 1049 first and underestimated samples 1050, 1051 and 1052 second (see *Fig. 6-2*). Material inhomogeneity accounts for the different deformations most likely. Further gradually increasing axial strains indicates stationary creep, which is noticeable in *Fig. 5-16* and *Fig. 6-2* by the almost equal values of axial strain rates.

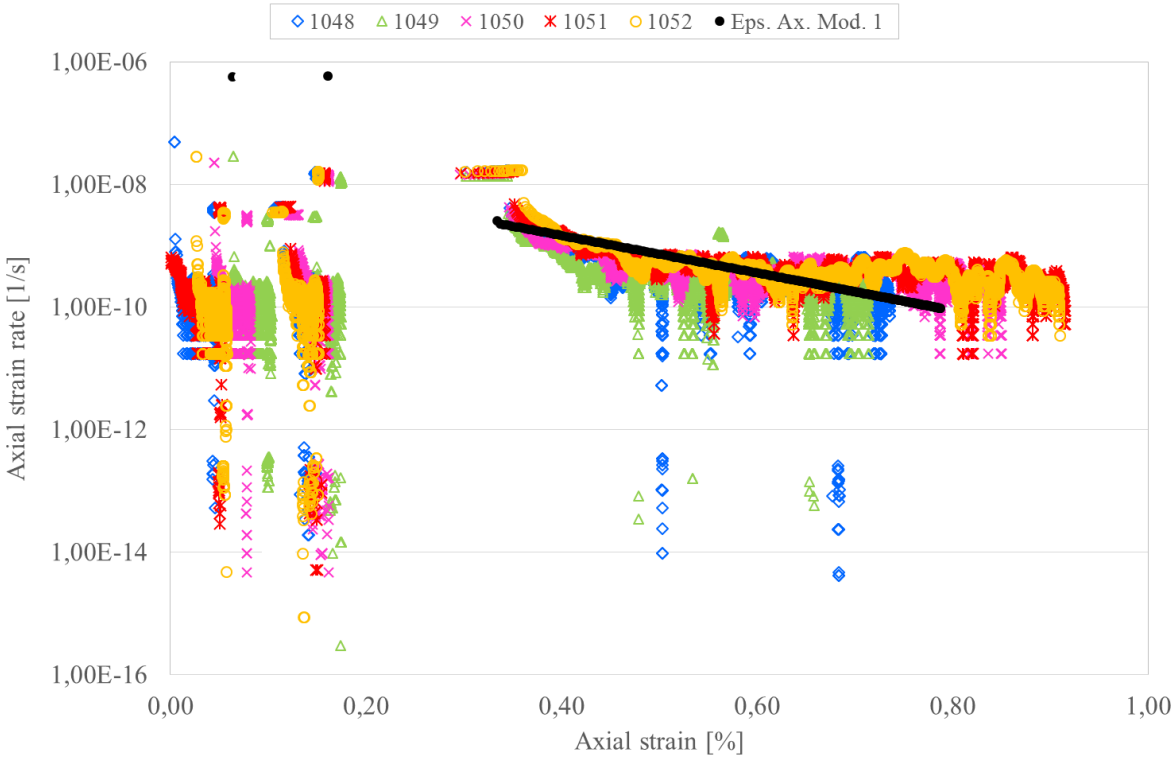

Fig. 6-2: Evaluation of assumed stationary creep deformations in the third deviatoric stress phase (Simulation results and experiment data are fitted at an axial strain of 0.16 %)

In contrast to these findings, the simulation curve shows a gradually declining line, which goes directly through the experiment data (see Eps. Ax. Mod. 1 in *Fig. 6-2*). Thus the description of stationary and tertiary creep respectively represents a drawback of the implemented creep law. The work of (Middelhoff and Czaikowski) mentions the simple mathematical structure of the

creep law as the main reason of the limitation. However the reproduction of all creep phases is negligible when simulating the stress conditions in a future repository as the development of an isotropic stress state is exclusively assumed. Lateral extensions accompany the axial reduction of the sample as well. Nevertheless the modified form of Lemaitre's creep law is also limited with respect to this point. As the incremental creep strain rate tensor is calculated by only taking the deviatoric stress tensor q into considerations, the volumetric component of the strain is omitted during constant stress.

6.3 CONCLUSION

The simulations revealed the applicability of the employed visco-plasticity constitutive model for simulating the short- and long-term behavior of salt concrete by means of using one set of material parameter. Although some drawbacks, mainly related to the description of creep deformations, have been identified, the constitutive model is able to reproduce the major deformation characteristics adequately. The *Tab. 6-3* summarizes briefly the main outcome:

Tab. 6-3: Final evaluation of performed simulations

	Characteristic	Adequate simulation?	
1	Strain hardening prior peak	YES	
2	Peak strength	YES	
3	Brittle behavior post peak	YES*[1]	
4	Volumetric strains while loading	YES	
5	Transient creep strains	YES	
6	Stationary creep strains		NO
7	Tertiary creep strains		NO
8	Volumetric strains while constant loading		NO
9	Rapture	YES*[2]	

*[1]: Although the sudden loss of material strength was described, the constitutive model is not able to reproduce the brittle behavior in fact, as it omits strain localization processes.

*[2]: Rapture as a result of accumulating viscoplastic strains has not been investigated within these simulations. However an adequate description is probable due to the determination of friction angle and cohesion.

Currently the employed visco-plasticity model is improved with respect to different aspects. The inclusion of regularization methods is envisaged in order to simulate strain localization processes. The next version will also include modifications within the implemented creep law to describe both stationary and tertiary creep. Since the evaluated TC-tests were performed by deforming the samples with the same deformation rate, it is recommendable to vary deformation rates within future laboratory tests. Thus a set of material parameters can be calibrated, which is rate-independent. The development of creep strains at low deviatoric stresses represents a further important aspect as deviatoric stresses above 20 MPa are not expected under repository conditions.

A APPENDIX: PERFORMED EXPERIMENTS

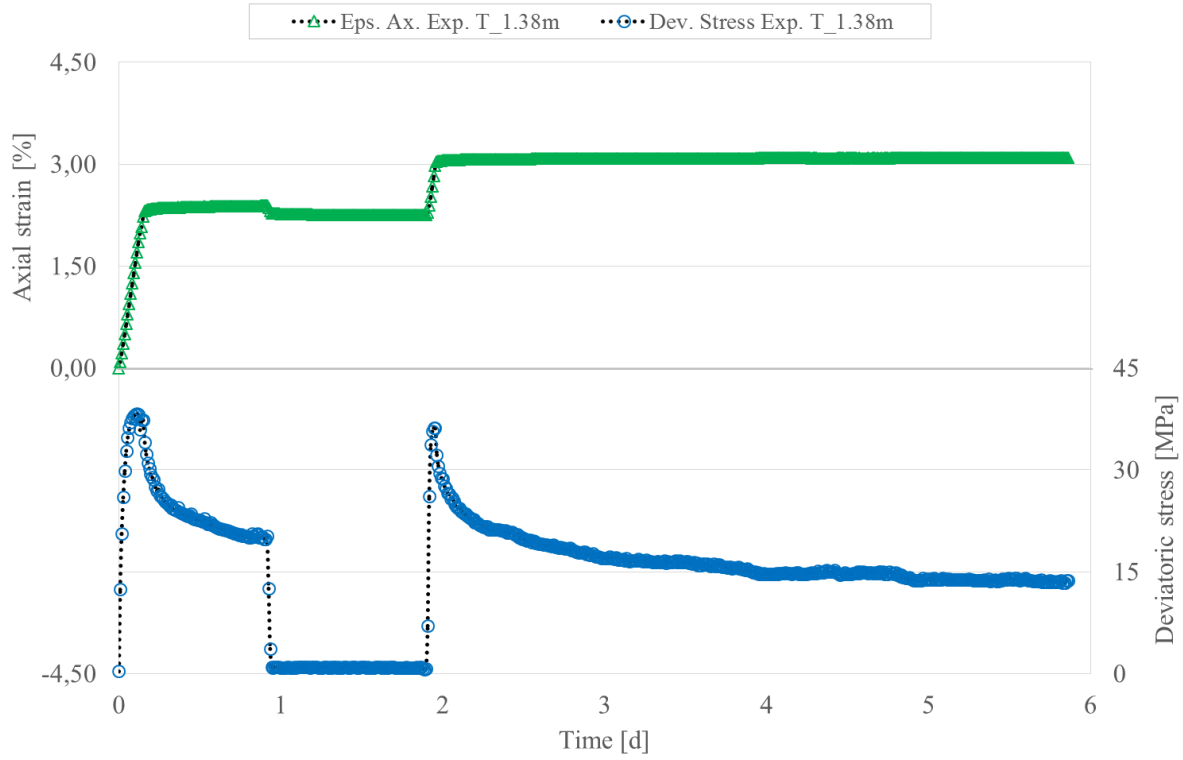

Fig. Appendix A-1: Axial strain application and evolving deviatoric stresses in time (T_1.38m)

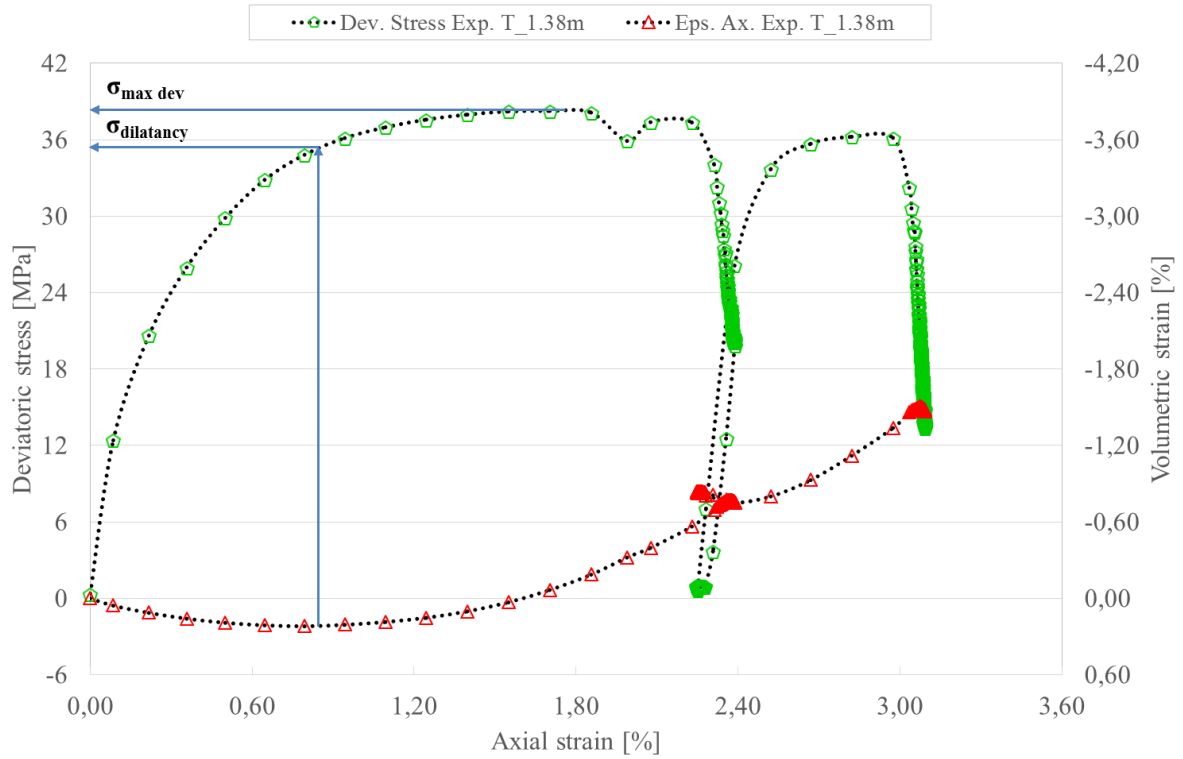

Fig. Appendix A-2: Evolution of deviatoric stresses and volumetric strains
(The maximum deviatoric stress as well as the dilatancy point are depicted)

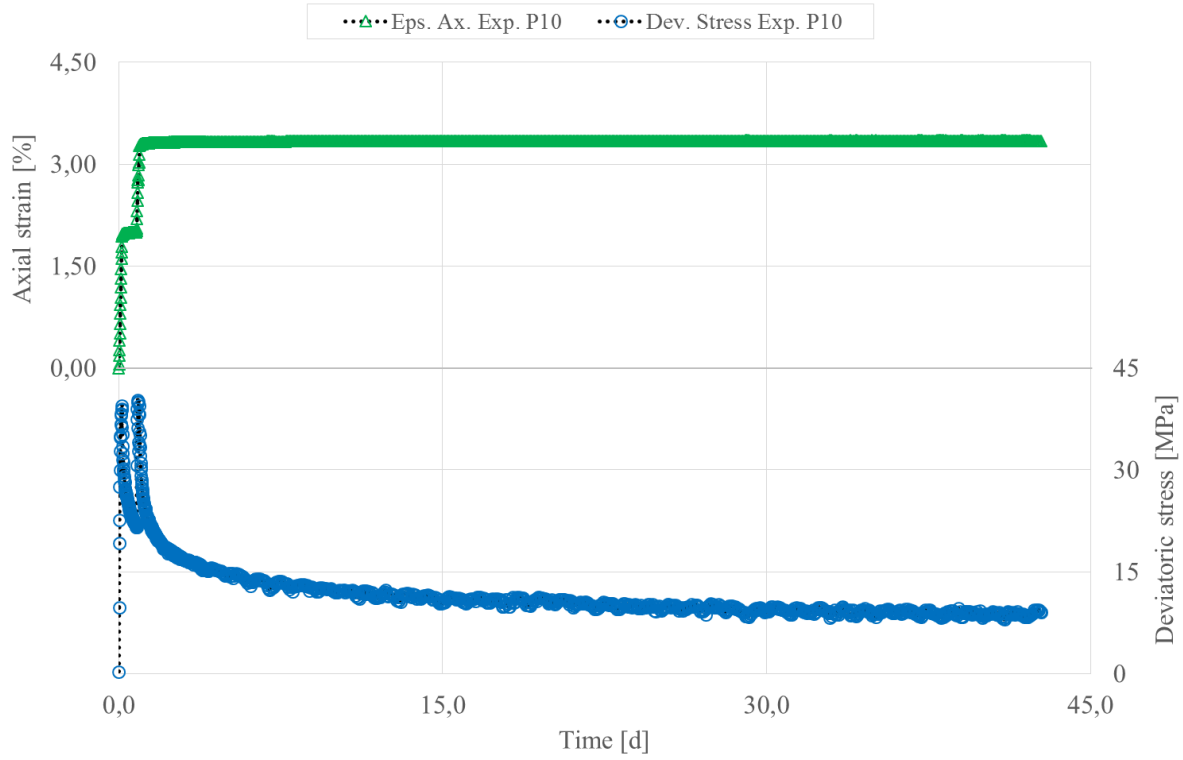

Fig. Appendix A-3: Axial strain application and evolving deviatoric stresses in time (P10)

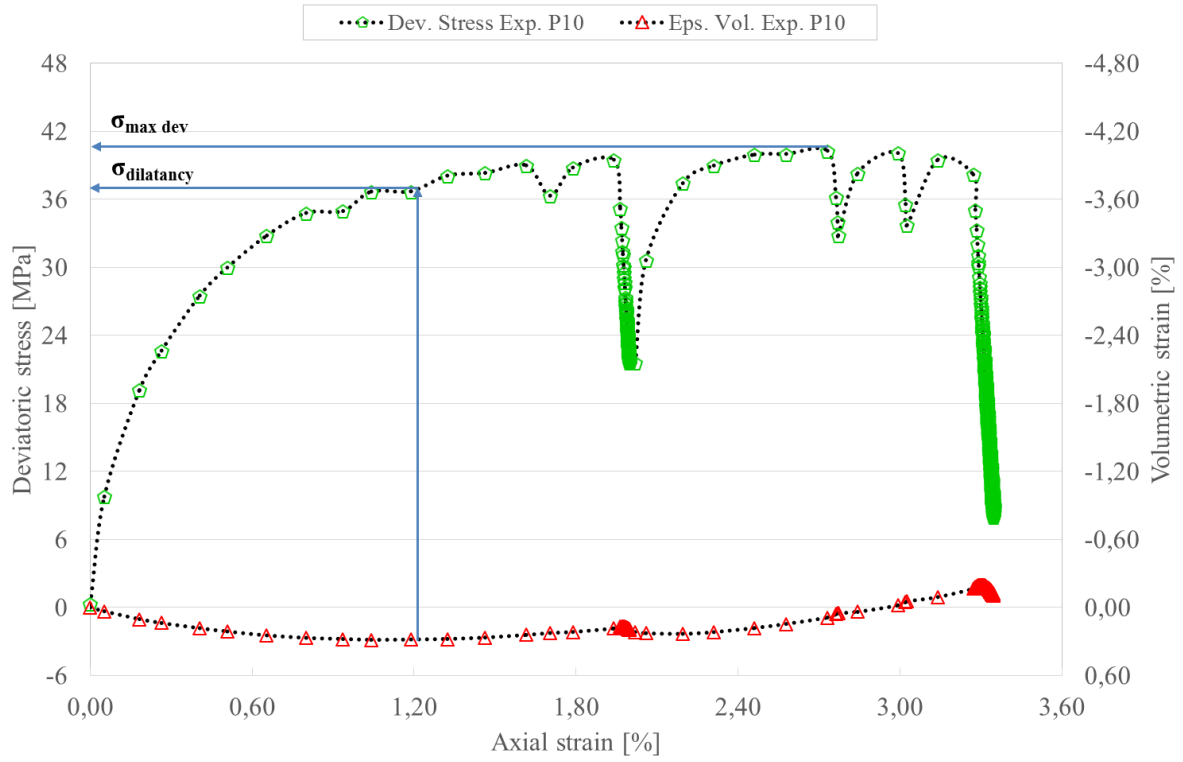

Fig. Appendix A-4: Evolution of deviatoric stresses and volumetric strains
(The maximum deviatoric stress as well as the dilatancy point are depicted)

B APPENDIX: NUMERICAL SIMULATIONS

GENERAL REMARK

The data for determining the vertical displacements and stresses were obtained in the center axis of the model at a height of 0.14 m (TC- test)/ 0.16 m (UCc- test). The deviatoric stresses were obtained in elements at model height of 0.07 m (TC- test)/ 0.08 m (UCc- test) and model radius of 0.035 m (TC- test)/ 0.04 m (UCc- test). Last the horizontal displacements were obtained in a node at model height of 0.07 m and model radius of 0.035 m.

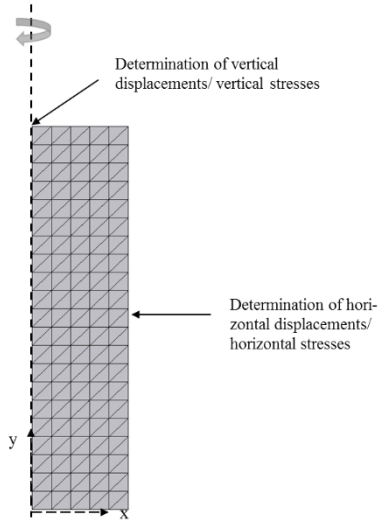

Fig. Appendix B-1: Determination of (vertical/ horizontal) displacements and stresses

Afterwards the created data was processed to compare the simulation results to the experiment results. The generated displacements had to be converted into strains. According to (Düsterloh 2010a) the axial, radial and volumetric strains were obtained by calculating:

$$\varepsilon_y = \left(\frac{\Delta l}{l_0}\right) * 100\% \qquad \text{Eq. B-1a}$$

$$\varepsilon_x = \left(\frac{\Delta r}{r_0}\right) * 100\% \qquad \text{Eq. B-1b}$$

$$\varepsilon_{vol} \cong \varepsilon_y + 2 * \varepsilon_x \qquad \text{Eq. B-1c}$$

The parameters l_0 and r_0 represent the initial length and the initial radius of the model respectively, whereas the horizontal as well as the vertical displacements are mentioned by Δl and Δr. In case of the TC- test, the volumetric strains ε_{vol} are derived by adding the vertical strain component to the horizontal strain components. In contrast to the displacements, the vertical and horizontal stresses are independent from the selected point within the model due to the homogeneous stress distribution, which was proved before. The vertical and the horizontal stresses were obtained from the same points as the evaluated displacements.

Last the deviatoric stresses are calculated as:

$$\sigma_{dev} = \sigma_y - \sigma_x \qquad \text{Eq. B-2}$$

By this means of processing the simulation results are comparable to the obtained results with the experiment results.

CONSISTENCY CHECK (TC-TEST)

To ensure that all boundary conditions are applied correctly, a consistency check was performed. The *Fig. Appendix B-2* shows the line evolution, which evaluates the final horizontal stress distribution in 0.07 m height when the calculation stops. It was assumed that the applied confining stresses σ_x = - 1 MPa, - 2 MPa or - 3 MPa create an almost homogeneous horizontal stress distribution within the sample. An insignificant stress reduction was expectable close to the center axis.

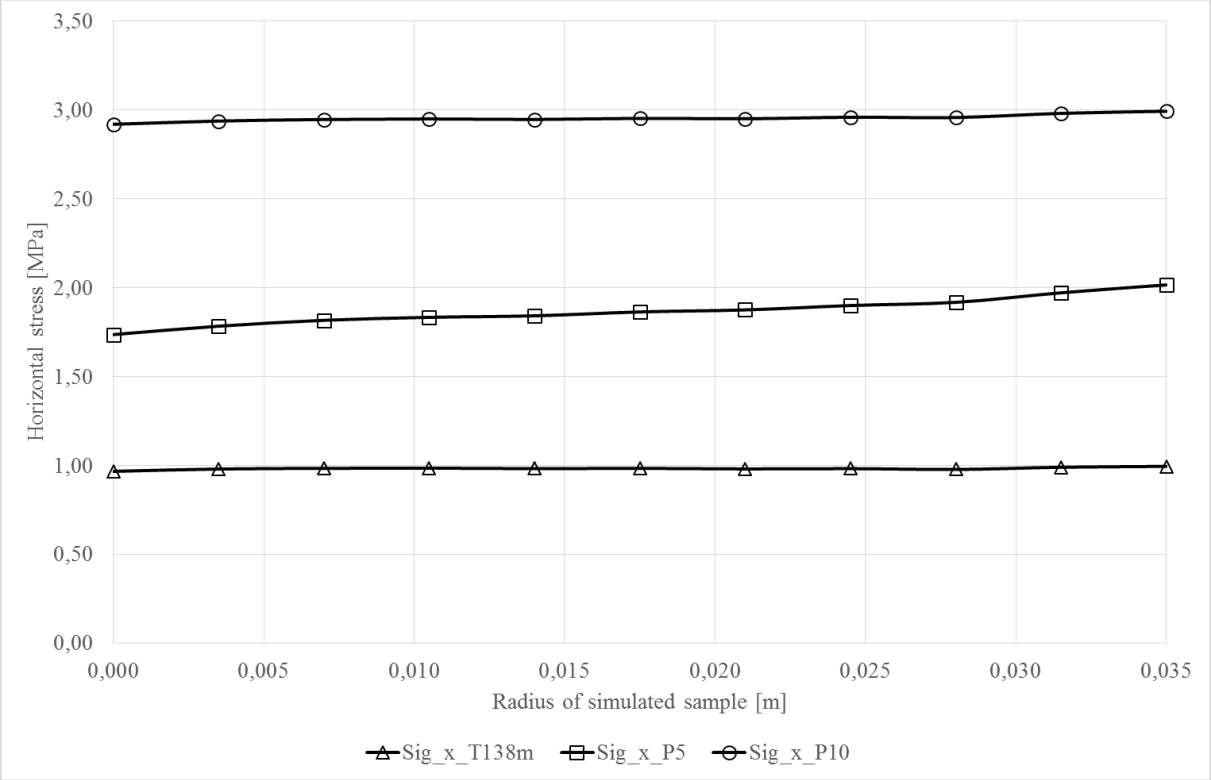

Fig. Appendix B-2: Horizontal stress distribution determined at a height $_{sample}$ = 0.07 m and failure time

The horizontal stress boundary conditions and the displacement restrictions were applied correctly. As depicted in *Fig. Appendix B-2*, the confining stresses affect the entire width of the sample in all the simulations as intended.

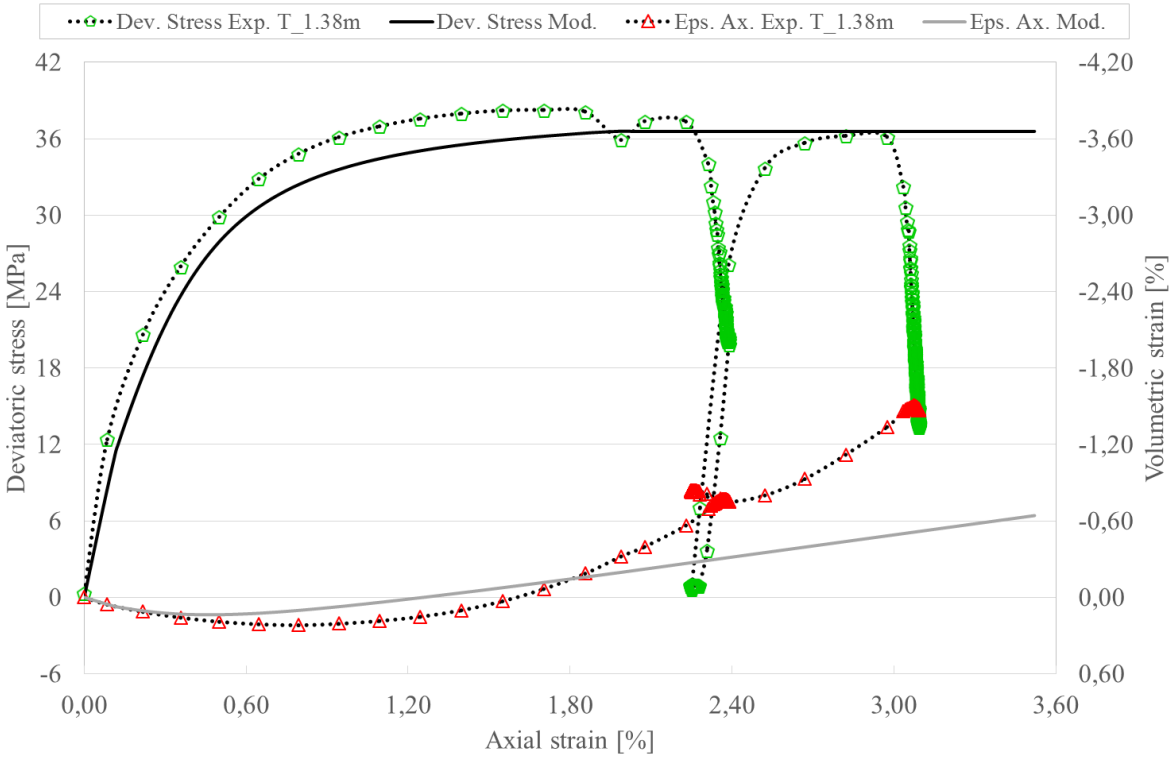

Fig. Appendix B-3: Finally obtained results for T_1.38m reproduction

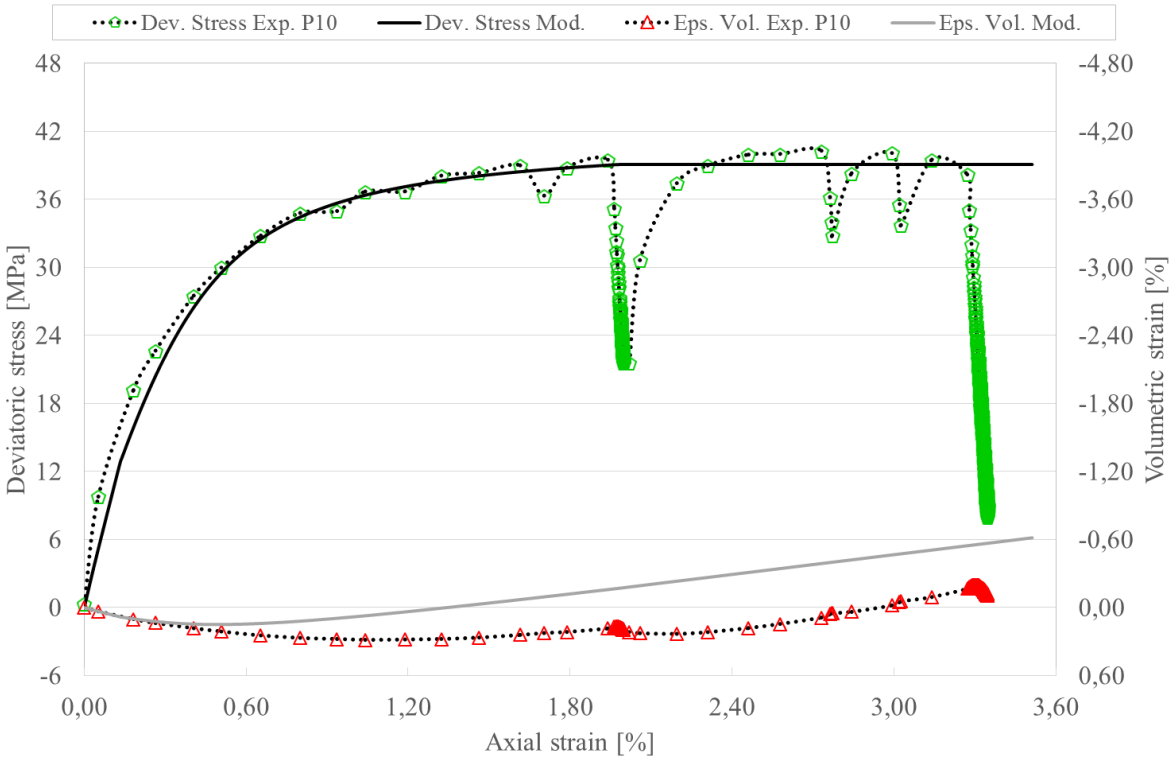

Fig. Appendix B-4: Finally obtained results for P10 reproduction

CONSISTENCY CHECK

In case of UCc-simulation a consistency check was performed as well to determine whether the boundary conditions were applied correctly. The horizontal stress value was assumed to be constant (σ_3 = - 0.1 MPa) during the simulation progress. The vertical stresses were assumed to increase stepwise (compare *Tab. 5-10*). Line evolutions were created, which revealed the stress distribution in horizontal and vertical direction. The vertical line evolution has been obtained in the center axis of the sample and the horizontal line evolution in sample height of 0.08 m.

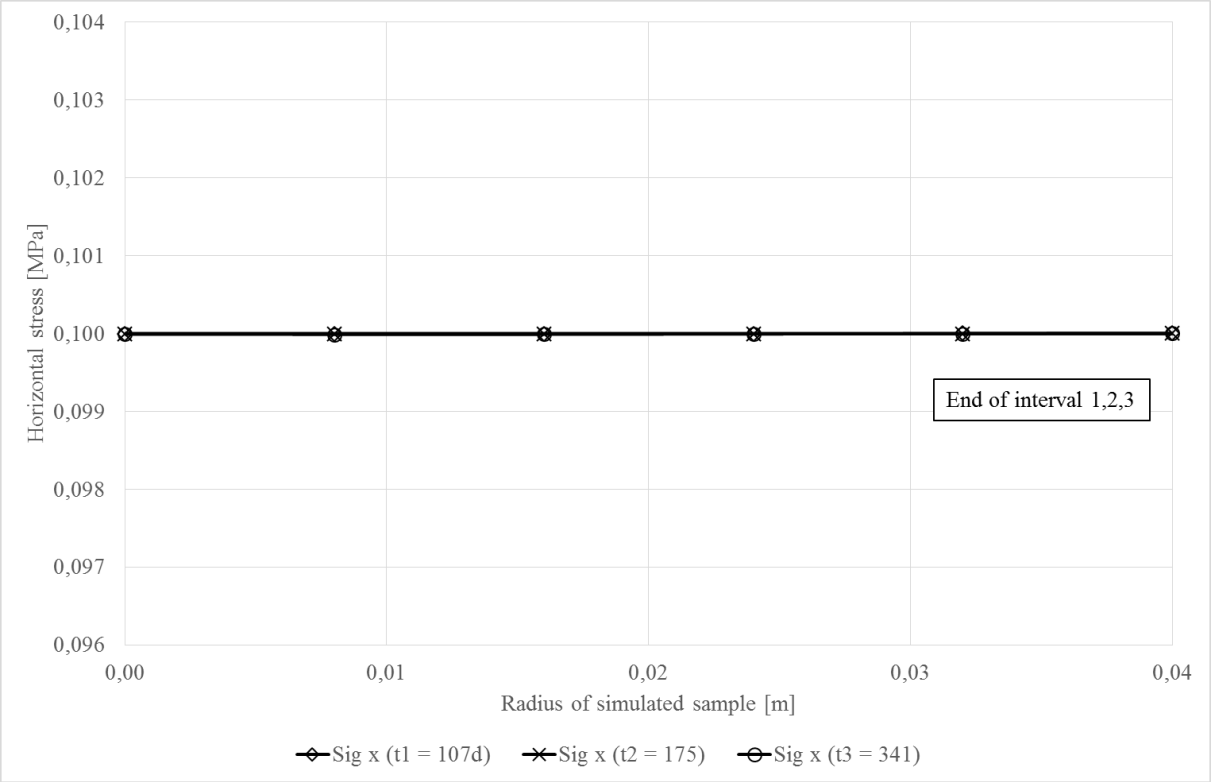

Fig. Appendix B-5: Horizontal stress distribution determined at a height $_{sample}$ = 0.08 m and end of intervals (1, 2 and 3)

The *Fig. Appendix B-5* shows an equally distributed horizontal stress state of σ_3 = - 0.1 MPa as it was assumed before. Apart from the horizontal stress distribution, the vertical stress conditions were applied correctly as well (see *Fig. Appendix B-6*).

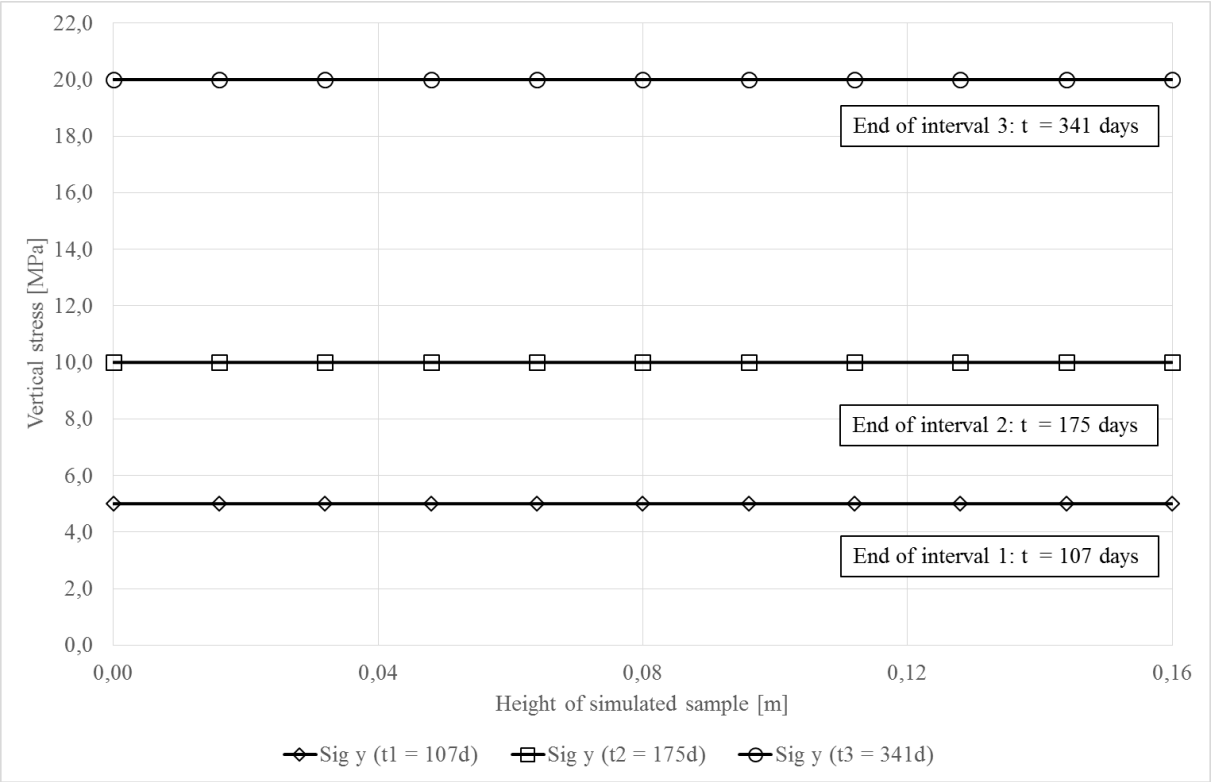

Fig. Appendix B-6: Vertical stress distribution determined at center axis and end of intervals (1, 2 and 3)

LIST OF FIGURES

LIST OF TABLES

REFERENCES

Bollingerfehr, Wilhelm (2013): Status of the safety concept and safety demonstration for an HLW repository in salt. Summary report. Peine: DBETEC.

Bundesministerium der Justiz und für Verbraucherschutz (23.07.2013): Gesetz zur Suche und Auswahl eines Standortes für ein Endlager für Wärme entwickelnde radioaktive Abfälle (Standortauswahlgesetz - StandAG). StandAG, vom Geändert durch Art. 2 G v. 26.07.2016 I 1843. Online verfügbar unter https://www.gesetze-im-internet.de/standag/BJNR255310013.html.

Bundesministerium für Umwelt, Naturschutz and Reaktorsicherheit (2010): Sicherheitsanforderungen an die Endlagerung wärmeentwickelnder radioaktiver Abfälle.

Chaboche, J. (2009): Elasto-Viscoplasticity. Nonlinear Computional Mechanics. Athens, 16.03.2009.

Czaikowski, O.; Hartwig, L.; Hertes, U.; Jantschik, K.; Miehe, R.; Müller, J.; Schwarzianeck, P. (2016): Full scale demonstration of plugs and seals (DOPAS) Deliverable D3.28 &D5.5. Status report on LASA related laboratory tests and on process modelling activities. Braunschweig: GRS (GRS, A-3760).

DBE (2004): Verfüllmaterial für Strecken mit hohen Anforderungen. Materialeigenschaften und Materialkennwerte Salzbeton M2. Verfahrensunterlagen. Hg. v. Bundesamt für Strahlenschutz (Planfeststellungsverfahren zur Stilllegung des Endalgers für radioaktive Abfälle Morsleben, P 192).

Düsterloh, Uwe (Hg.) (2010): Geotechnische Sicherheitsnachweise für Hohlraumbauten im Salinargebirge unter besonderer Berücksichtigung laborativer Untersuchungen. Ein Beitrag zum Nachweis von Standsicherheit und Barrierenintegrität für untertägige Abfallentsorgungsanlagen und Hohlraumbauten des salinaren Berg- und Kavernenbaus. Zugl.: Clausthal, Techn. Univ., Habil.-Schr., 2009. 1. Aufl. Clausthal-Zellerfeld: Papierflieger-Verl. (Schriftenreihe / Lehrstuhl für Deponietechnik und Geomechanik, Institut für Aufbereitung, Deponietechnik und Geomechanik, Technische Universität Clausthal, 16).

Etse, G.; Lorefice, R.; Carosio, A.; Carol, I. (2004): Rate dependent interface model formulation for quasi-brittle materials. Hg. v. IA-FraMCoS (FraMCoS-5 Vail (USA), 2004 Proceedings, 96). Online verfügbar unter http://framcos.org/FraMCoS-5.php#gsc.tab=0.

Fischer-Appelt, Klaus (2013): Synthesebericht für die VSG. Bericht zum Arbeitspaket 13 ; vorläufige Sicherheitsanalyse für den Standort Gorleben. Köln: GRS (GRS, 290).

Heeres, Otto M.; Suiker, Akke S.J.; Borst, René de (2002): A comparison between the Perzyna viscoplastic model and the Consistency viscoplastic model. In: *European Journal of Mechanics - A/Solids* 21 (1), S. 1–12. DOI: 10.1016/S0997-7538(01)01188-3.

International Atomic Energy Agency - IAEA (2009): IAEA Safety Standards for protecting people and the environment. Classification of radioactive waste. Vienna (General Safety Guide, GSG-1).

International Atomic Energy Agency - IAEA (2011): IAEA Safety Standards for protecting people and the environment. Disposal of radioactive waste. Specific Safety Requirements. Vienna (IAEA Safety Standards Series, SSR-5).

International Energy Agency - IEA; OECD Nuclear Energy Agency - NEA (2015): Technology Roadmap. Nuclear Energy. Energy Technology Perpectives. Paris.

Jirásek, M. (2002): Objective modeling of strain localization. In: *Revue française de génie civil.* (6), S. 1119–1132.

Kelly, P. (2015): Solid Mechanics (I). Lecture notes. University of Auckland, Auckland.

Krabbenhöft, Kristian (2002): Basic computional plasticity. Hg. v. Department of Civil Engineering. Technical University of Denmark.

Mánica, M.; Gens, A.; Vaunat, J.; Ruiz, D. F. (2016a): A cross-anisotropic formulation for elasto-plastic models. In: *Géotechnique Letters* 6 (2), S. 156–162. DOI: 10.1680/jgele.15.00182.

Mánica, Miguel; Gens, Antonio; Vaunat, Jean; Ruiz, Daniel F. (2016b): A time-dependent anisotropic model for argillaceous rocks. Application to an underground excavation in Callovo-Oxfordian claystone. In: *Computers and Geotechnics. DOI:* 10.1016/j.compgeo.2016.11.004.

Mehta, Povindar K.; Monteiro, Paulo J. M. (2006): Concrete. Microstructure, properties, and materials ; [CD-ROM with 1000+ Powerpoint slides, videos, bonus material, and more]. 3rd ed. [fully rev. and updated]. New York: McGraw-Hill. Online verfügbar unter http://www.loc.gov/catdir/enhancements/fy0664/2005053352-b.html.

Middelhoff, M. (18.08.2016): Contributions to the simulation of salt concrete: Applicability-assessment of a modified creep law implemented in the “Argillite-Model”. Clausthal-Zellerfeld.

Middelhoff, M.; Czaikowski, O.: Applicability assessment of the “Argillite-/ Composite-Model”-approach. Modelling the time-dependent mechanical behavior of concrete basedsealing material in rock salt related to the DOPAS-project. In: Workshop of Code_Bright, Bd. 8, S. 25–30. Online verfügbar unter https://www.etcg.upc.edu/recerca/webs/code_bright/workshop/8th-workshop-of-code_bright.

Mönig, Jörg (2012): Sicherheits- und Nachweiskonzept. Bericht zum Arbeitspaket 4 Vorläufige Sicherheitsanalyse für den Standort Gorleben. Garching: GRS (GRS, 277).

Müller-Hoeppe, Nina (2012): Vorbemessung. Köln: GRS (GRS, 287).

Olivella, S.; Carrera, J.; Gens, A.; Alonso, E. E. (1994): Nonisothermal multiphase flow of brine and gas through saline media. In: *Transp Porous Med* 15 (3), S. 271–293. DOI: 10.1007/BF00613282.

Olivella, S.; Carrera, J.; Gens, A.; Alonso, E. E. (1996): Porosity variations in saline media caused by temperature gradients coupled to multiphase flow and dissolution/precipitation. In: *Transp Porous Med* 25 (1), S. 1–25. DOI: 10.1007/BF00141260.

Olivella, S.; Gens, A. (2002): A constitutive model for crushed salt. In: *Int. J. Numer. Anal. Meth. Geomech.* 26 (7), S. 719–746. DOI: 10.1002/nag.220.

Pajak, M. (2011): The influence of the strain rate on the strength of concrete taking into account the experimental techniques. In: *ACEE* (3).

Wieczorek, Klaus (2010): THERESA subproject MOLDAU. Coupled thermal hydrological mechanical chemical processes in repository safety assessment ; final report. Köln, Hannover: Ges. für Anlagen- und Reaktorsicherheit (GRS); Technische Informationsbibliothek u. Universitätsbibliothek (GRS, 262).

Zienkiewicz, O. C.; Cormeau, I. C. (1974): Visco-plasticity-plasticity and creep in elastic solids-a unified numerical solution approach. In: *Int. J. Numer. Meth. Engng.* 8 (4), S. 821–845. DOI: 10.1002/nme.1620080411.

Zienkiewicz, Olgierd Cecil; Taylor, Robert Leroy (2003): Solid mechanics. 5. ed., reprinted. Oxford: Butterworth-Heinemann (The finite element method, / O. C. Zienkiewicz; R. L. Taylor ; Vol. 2).